ABSTRACT

Title of Thesis: DEVELOPMENT OF HYBRID AIR-WATER ROTOR TRANSITION THRUST PREDICTION AND CONTROL

Ilya Yevgeniyevich Semenov
Masters of Science, 2020

Thesis directed by: Professor Inderjit Chopra
Department of Aerospace Engineering

Hybrid vehicles are able to function in some combination of aerial, underwater, and terrestrial environments, which greatly expands the scope of missions a vehicle can perform. Hybrid aerial-water (HAW) vehicles are a promising subcategory that are designed to operate in two vastly different fluid mediums. Multirotor HAW vehicles configurations have advantages in maneuverability, but pose a challenge in the water entry or water exit transitions. The interaction of a powered rotor with the air-water interface and its performance in a mixed air-water medium are poorly understood. Previous HAW vehicle strategies avoid a powered rotor with additional propulsion and buoyancy systems, constraining the design space.

A custom test stand was constructed to better understand rotor performance during the air-water transition. By recording powered rotor performance during controlled water entries and exits in a large tank, several novel observations were made. Previously unrecorded phenomenon such as the gradual height and RPM dependent transition and the underwater ceiling effect are determined.

These observations inform the development of the Transition Index TI, a novel metric that indicates the transition state of the rotor, without the need for specialized sensors or computationally intensive modeling. TI is applied to experimental data to make further observations, and is also used in a novel thrust prediction formulation. The first known low-order prediction of thrust through the transition is validated against experimental data, and allows for the development of a TI based controller. A preliminary controller implementation shows promising results in maintaining constant thrust through the air-water transition.

Finally, a HAW vehicle to apply this controller is built. Careful consideration to the waterproofing and motor choice is shown and preliminary flight tests are demonstrated.

Future expansion on the application of the novel TI and thrust prediction has great potential to advance the capabilities of hybrid aerial-water vehicles.

DEVELOPMENT OF HYBRID AIR-WATER ROTOR TRANSITION THRUST PREDICTION AND CONTROL

by

Ilya Yevgeniyevich Semenov

Thesis submitted to the Faculty of the Graduate School of the
University of Maryland, College Park in partial fulfillment
of the requirements for the degree of
Master of Science
2020

Advisory Committee:
Professor Inderjit Chopra, Chair
Professor Anubhav Datta
Professor James Baeder

Preface

Some effort was taken to minimize the annihilation of electrical components during the making of this thesis.

Dedication

To my Mother and Father

I am forever grateful for the endless support you show for my progress in life.

Acknowledgments

Many people have contributed greatly to this research, without their advice, suggestions, questions, and support it would never have come together

Dr. Chopra, as my advisor you have always had the wisdom to guide me towards ambitious, and progressive goals throughout my time as his student. The mentality you instilled in me to build up from simple concepts and strive for distinct and important milestones will stay with me for the rest of my life. Your feedback and direction was invaluable to this work.

Dr. Nagaraj, thank you for always having time for my questions, carefully considering my concerns and challenges, and helping me overcome them. You have taught me to convey the turbulent mix of ideas and observations in an approachable, understandable way. Without your support, advice, and belief in me I fear this thesis would be unreadable.

Dr. Hrishikeshavan, your help with the technical challenges and helpful advice were essential to my progress. Anytime I feared I could not overcome an obstacle, I knew your perspective and advice would help me get through it.

Ehis, Austin, and Robert, your support and listening to me ramble about issues truly helped keep my head straight. We progressed through our classes and research together, and it was an honor to learn with you guys.

Konrad, Jacob, and Nathan. Thank you for assisting me in my research, your contributions are valuable and I hope the experience was fulfilling.

Table of Contents

Commonly Used Definitions

A	Rotor Area, πR^2
α	Blade angle of attack
c	Chord length
C_d	Drag coefficient
C_l	Lift coefficient
$C_{l\alpha}$	Lift curve slope
C_m	Moment coefficient
C_P	Rotor shaft power coefficient, $\frac{P}{\rho A(\Omega R)^3}$
C_Q	Rotor torque coefficient, $\frac{Q}{\rho A(\Omega R)^2 R}$
C_T	Rotor thrust coefficient, $\frac{T}{\rho A(\Omega R)^2}$
C_{Ta}	Rotor thrust coefficient in air
C_{Tw}	Rotor thrust coefficient in water
F	Prandtl tip loss factor
F_y	Aerodynamic force in y direction
F_z	Aerodynamic force in z direction
h	Height above water surface
$\bar{h}$	Non-dimensional height above water surface, $\frac{h}{R}$
I	DC Current
κ	Induced power factor
λ	Inflow non-dimensional velocity, $\frac{u}{\Omega R}$
N_b	Number of blades
Ω	Rotor angular velocity
ϕ	Inflow angle of attack
P	Rotor mechanical power, $Q\Omega$
P_0	Rotor profile power
Q	Rotor torque
ρ	Density
ρ_a	Density of air
ρ_{eff}	Effective medium density during air-water transition
ρ_w	Density of water
R	Rotor radius
r	Non-dimensional span along blade, $\frac{x}{R}$
Re	Reynolds number
σ	Rotor solidity
θ	Local blade pitch
θ_0	Collective pitch
θ_{tw}	Blade twist
θ_f	Blade torsional displacement
T	Rotor thrust

T_a	Expected thrust in air
T_w	Expected thrust in water
T_{pred}	Predicted thrust
thr	Throttle input to ESC, normalized between, $0 \leq thr \leq 1$
TI	Transition index
U	Fluid velocity
U_P	Fluid velocity component parallel with the axis of rotation
U_T	Fluid velocity component tangent to the axis of rotation
V	Voltage
v_i	Inflow velocity
w	Bending displacement
x	Span along blade

AC	Aerodynamic Center
ADC	Analog to Digital Converter
AQWUA	A Quad With Underwater Ability
BEMT	Blade Element Momentum Theory
BET	Blade Element Theory
BLDC Motor	Brushless DC motor
CFD	Computational Fluid Dynamics
DC	Direct current
EA	Elastic Axis
ESC	Electronic Speed Controller
FEA	Finite Element Analysis
FEM	Finite Element Method
HAW	Hybrid Aerial-Water
MT	Momentum Theory
PWM	Pulse Width Modification
ROV	Remotely Operated Vehicle
RPM	Revolutions per minute
TURNS2D	Transonic Unsteady Rotor Navier–Stokes 2D solver

Chapter 1: Introduction

1.1 Applications of Hybrid Air-Water Vehicles

[1]

Hybrid aerial-water (HAW) vehicles are a category of aircraft that can perform missions in air as well as underwater. They have advantages over conventional vehicles for certain applications in commercial, civilian, and military sectors. However, HAW vehicles have to overcome the challenge of operating and transitioning between two vastly different environments.

Often, a single HAW vehicle can replace two separate non-hybrid aerial and submersible vehicles. For instance, multiple vehicles are traditionally required when inspecting the structure of a construction that is partially submerged [2], [3]. The inspection of bridges, dams, offshore energy facilities, liquid processing stations, ship hulls, and various plumping or waste water infrastructure can be performed by a single vehicle by equipping a HAW platform with the appropriate sensors as the payload. This allows for more cost effective and safer inspections as fewer tasks need to be completed by humans in treacherous locations. Some of these buildings and structures are shown in Figure 1.1.

Figure 1.1: Examples of water surface piercing structures

In addition to inspection, HAW vehicles can perform various military roles. The ability to launch aerial vehicles from a submarine is useful for reconnaissance and discrete deployment of resources [4]. Similarly, the ability to fly a HAW vehicle to a desired location at the sea quickly and survey underwater can be tactically advantageous and is faster than deploying a submersible vehicle to travel through the water to the same location. Having an aerial vehicle be able to take cover and minimize energy use in the water can also be a strategical advantage.

Lastly, perhaps a HAW vehicle's major advantage is in navigating flooded or partially flooded terrain. For instance, cave systems often have pockets or tunnels that are flooded called sumps, a map of a cave that features such sumps is shown in Figure 1.2. A conventional submersible or aerial vehicle could not navigate past a sump. HAW vehicles that can navigate such areas are applicable in search and rescue and geological research fields.

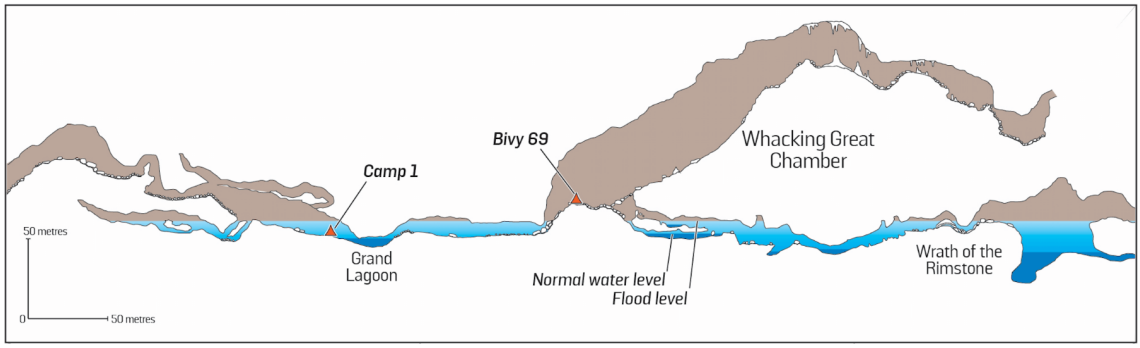

Figure 1.2: Map section of a cave with sumps [5]

1.2 Approaches to Hybrid Air-Water Vehicles

The most notable difference between aerial and water environments for the purpose of navigation is medium density. Water is over 800 times more dense than air at typical atmospheric conditions, which means that the fluid dynamic forces involved change drastically. HAW vehicles need to have a propulsion system that can operate in both a high density and low density regime, which is enormously challenging.

Generally, two categories of HAW vehicles exist. One is a fixed wing concept that can dive into and jump out of the water at speed. An example of this category

of vehicle is shown in Figure 1.3. This approach is an example of bio-mimicry, replicating the action of diving birds such as gannets on water entry and flying fish such as sailfins on water exit. These types of vehicles have advantages in aerial endurance and range due to the efficiency of a wing in forward flight. However they have disadvantages in maneuverability in both mediums. This is caused by the dependence on airspeed for lift in the air, eliminating the ability to hover and constraining a minimum turn radius, as well as the lack of vectored thrust in water, resulting in a lack of ability to pivot in place [6]. Additionally, fixed wing HAW vehicles concepts tend to have problems with a controllable dynamic water exit [7].

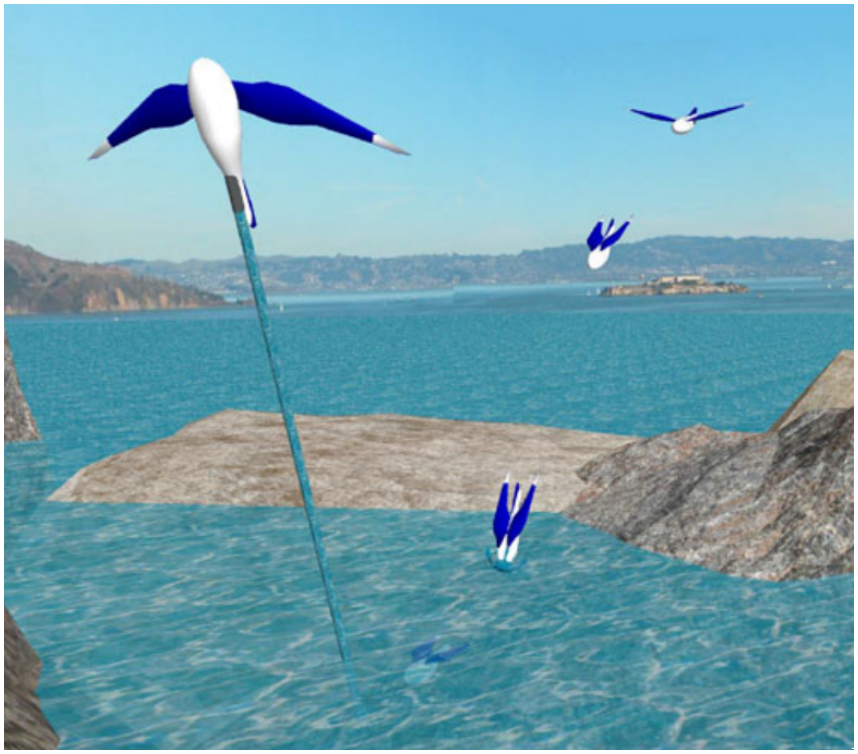

Figure 1.3: Concept sketch of a fixed wing HAW vehicle performing water entry and exit [6]

The second concept is a multi-rotor design. This thesis focuses on such a vehicle. Multi-rotor HAW vehicles combine the working principles of aerial multi-

rotors and traditional remotely operated underwater vehicles (ROVs). Due to the ability to control the thrust vector and reverse individual rotor thrust direction these types of vehicles tend to be extremely maneuverable, able to hover in air, and turn with zero radius in water. This is an advantage for operating payloads that comes at the cost of lowered aerial endurance. However, a major challenge for such a vehicle is the rotor interaction with the water in the transition state. The selection of a rotor and power system capable of sufficient performance in both air and water is not an easy task. Even more challenging is the air-water transition.

The performance of a rotor that operates in a mixed air and water environment such as that during the water entry or exit transitions is poorly understood. As such, the air to water or water to air transition of a multi-rotor HAW vehicle does not appear to be attempted with a powered rotor. Instead, the transition through the water surface has been previously approached by entirely avoiding a powered rotor in transition. There are two basic approaches: two sets of rotors or a buoyancy system.

One such approach using two rotor sets is used by the commercialized vehicle from Rutgers University called The Naviator shown in Figure 1.4 [8]. The Naviator platform uses two sets of rotors vertically spaced in an X8 configuration. Water sensors above the top rotor set, and below the bottom rotor set are used to detect the water. The procedure for the transition into the water involves powering off the lower rotors when the water is approached and using the top rotors operating fully in air to descend the vehicle such that the lower rotors are submerged. Then the lower rotors are powered on in fully submerged conditions and the upper rotors are

powered off. The vehicle then descends further into the water and the upper rotors are powered on again only in fully submerged conditions. In this case, the transition states are avoided. This strategy avoids having a powered rotor produce thrust in the air-water interface and results in successful transitions. However, this approach restricts the multi-rotor configuration space significantly, and requires additional sensors not typically required for an aerial rotorcraft [8, 9].

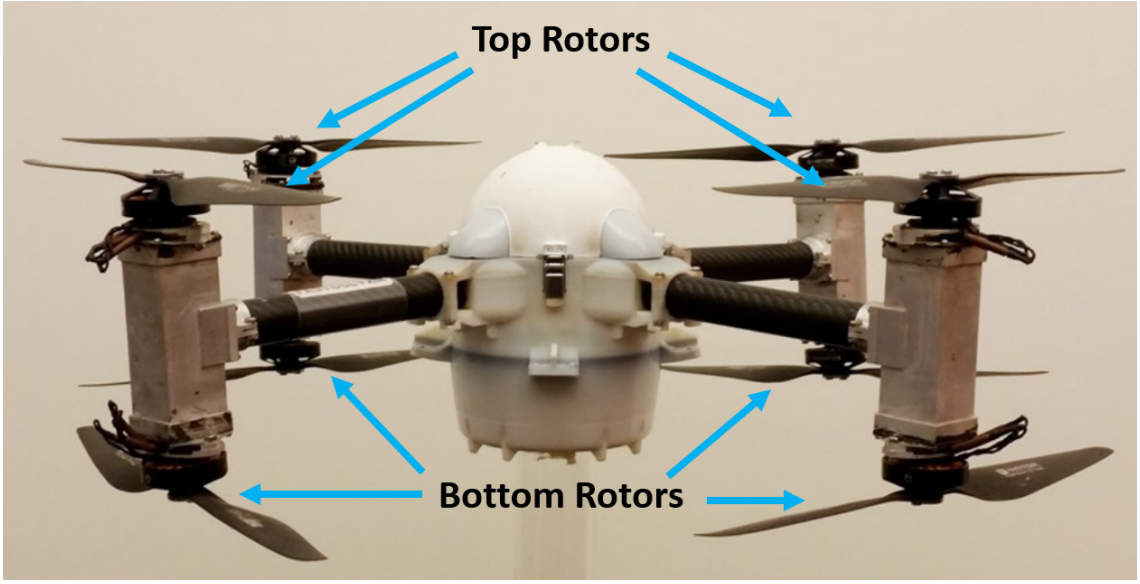

Figure 1.4: The Naviator HAW vehicle [9]

A similar transition strategy is used by other research vehicles, with the difference that the lower rotor set uses marine propellers rather than aerial rotors. It was found that the X8 configuration with counter-rotating rotors is inefficient in air and water. This type of configuration uses only one set of rotors in the air or water, and similarly never powers either rotor set at the air water interface [10]. The same configuration constraint and sensor requirement exists here as for the Naviator. Additionally this configuration requires supporting the weight of a propulsion system

that is unused in one medium, limiting the payload size.

The two rotor set approach avoiding the powered rotor in the transition has a fundamentally limiting constraint regardless of the rotor types selected. These vehicles are limited to relatively still water with near vertical transitions only. Transitions of this type are limited to minimal horizontal velocity and have an inclination constraint determined by the geometry of the rotor sets. Additionally the transition velocity is limited by the rotational acceleration and brake speed of the rotors.

The other type of approach involves a buoyancy system to perform the transition operation. One such example is the Loon Copter vehicle from Oakland University shown in Figure 1.5. The vehicle is a standard quadrotor configuration carrying a pneumatic tank and ballast system [11]. Initially buoyant the vehicle lands on the water surface and powers off the rotors. The tank is then filled with water and the vehicle descends into the water. The rotors are then powered on in a completely submerged condition. The exit from the water is performed similarly, with the tank being evacuated to raise the buoyancy and lift the unpowered rotors out of the water. They are then powered on in a fully aerial state and the vehicle takes off. The advantage of such an approach is the ability to transition in rougher water relative to the two rotor set approach. The disadvantage is that the transition is performed slowly compared to the two rotor set approach, which is already limited in transition velocity. Furthermore there is a large weight penalty for carrying the buoyancy system that is unused during aerial operation. The payload size with this approach is limited as a result and transitions remain constrained to minimal horizontal velocity relative to the water.

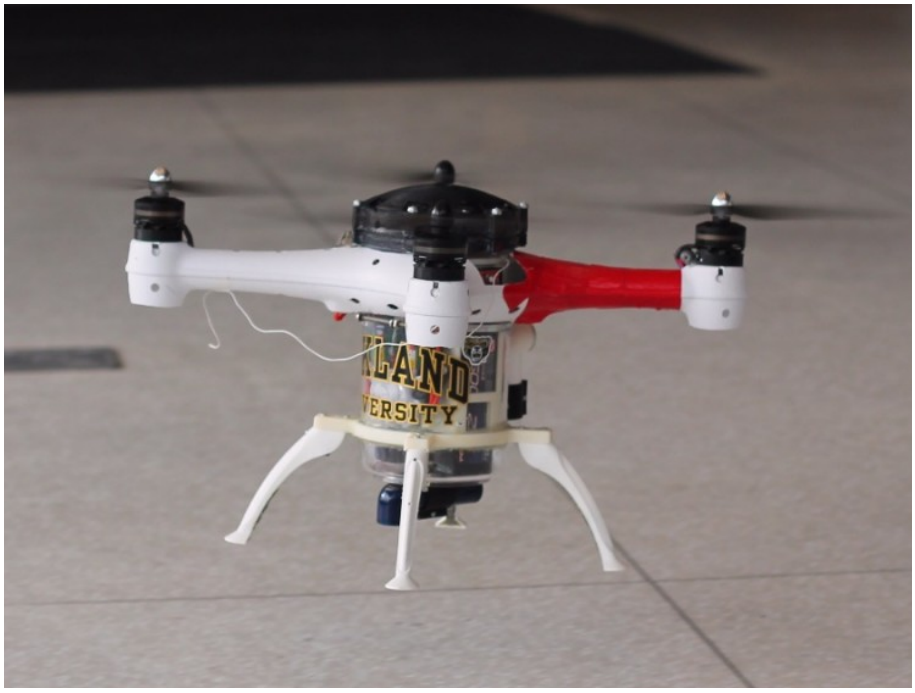

Figure 1.5: The Loon Copter HAW vehicle [11]

In general, one of the biggest disadvantages of approaches that avoid a powered rotor transition is the extra weight required in the form of propulsion systems or buoyancy systems. Additionally constraints on the transition approach, speed, and water surface state minimize the applicability and capability of such vehicles.

This thesis suggests an approach that does not require additional propulsion, active buoyancy, or sensor systems by leveraging an expanded understanding of rotor performance in a mixed air-water medium. By utilizing the motors as sensors and enabling a controller based on thrust prediction during the transition of a powered rotor, a multirotor vehicle is transformed into a HAW vehicle through systematic satisfaction of only motor output and waterproofing requirements. The AWQUA (A Quad With Underwater Ability) is the vehicle created for this thesis that implements such a strategy, it is shown in Figure 1.6. Such an approach can be applicable to

other configurations, allows for more design flexibility and increases payload fraction. Additionally this approach has the potential to allow for angled transitions with lateral velocity in and out of the water.

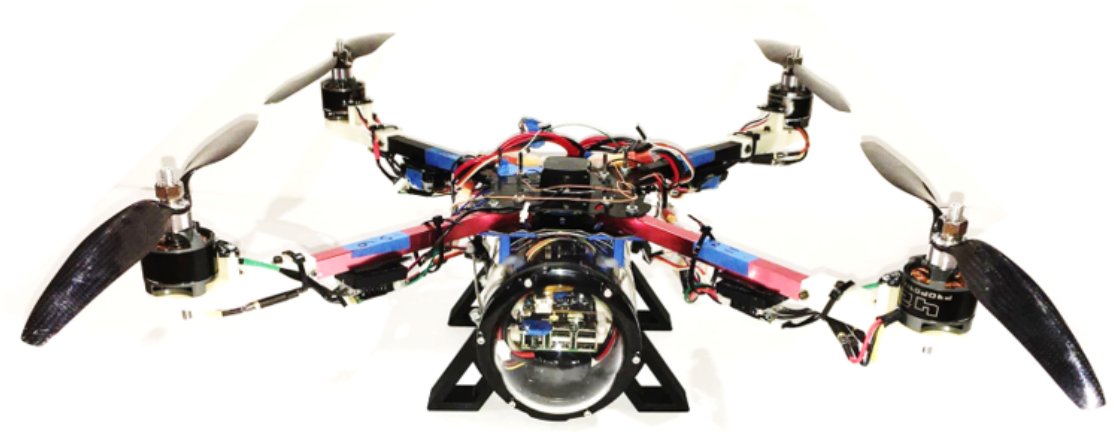

Figure 1.6: The AQWUA hybrid aerial-water vehicle

1.3 Rotor in Multi-Medium Environment

A HAW vehicle that uses a powered rotor during the transition requires a systematic understanding of the rotor performance in a mixed air-water medium. The knowledge of thrust at different states may enable a controller to be designed. However, for such a controller to work effectively the prediction must not rely on computationally intensive procedures such as computational fluid dynamics (CFD), which cannot be performed by a flight computer in real time. As such, a general understanding of the transition performance for a variety of rotors is desired. Very few prior works have approached a similar problem from a general perspective.

Due to the novel nature of HAW vehicles with powered rotors during the transition, insights were taken from various other analogous fields. One such example is

in surface piercing boat propellers, an example of which is shown in Figure 1.7.

Figure 1.7: A surface piercing propeller on the Turanor PlanetSolar [12]

Boat propellers differ from HAW vehicle applications in that they remain at a near right angle with the water surface at all times. Conversely, HAW rotors are not restricted in orientation and they tend to be mostly parallel to the water surface during transition. Surface piercing propellers are a subcategory of boat propellers where some portion of the propeller disk breaks the surface of the water. These types of propellers have greater efficiency due to ventilated supercavitation, a process where the air from the atmosphere is entrained to the suction side of the hydrofoil. The thrust increases and the drag decreases due to the low density and low pressure of the air relative to the water.

Surface piercing propellers have been conceptualized and experimented with since the late 19th century, however a theoretical foundation only came about in

1969 and required numerical integral methods [13]. All work since then has relied on numerical methods to process high dimensional equations [14–16]. While there are promising results, using this approach for the practical multirotor HAW vehicle is not viable due to the presence of significant lateral velocity which allows the rotor to move away from the highly mixed air-water medium that occurs in the wake of a SP propeller. Studies on the composition of the air-water medium in the wake of a ventilated airfoil exist, but assume an air flow rate into the water which would be determined with numerical methods in the case of SP propellers [17].

Another field where a rotor operates in a mixed air-water medium is in mechanical aerators, an example of which is shown in Figure 1.8. Various applications call for increased oxygen content in water and one method to achieve this is a mechanical surface aerator, common in waste-water treatment plants. Such an aerator is composed of a rotating impeller positioned near the water surface that stirs the air and water. Work in this field focuses on the molecular oxygen content in the water of the tank as a whole and related parameters [18, 19]. Insights on the mixed media state as a function of distance from the impeller are not offered nor is the gas flow rate as a function of impeller geometry and distance to water surface. Due to the lack of studied variables that are of interest to HAW applications the insights provided by the aeration field on the total long term state of a finite volume of water are not applicable for use in a HAW vehicle context.

Figure 1.8: A mechanical surface aerator in action

While there are some reports on the performance of various rotors in air-water mixtures, the focus and approach of these efforts are not directly applicable for the challenge of estimating rotor performance in air-water transition in flight. Therefore, a novel approach is required to develop an efficient hybrid aerial-water system.

1.4 Outline of This Thesis

This thesis is organized progressively, with more fundamental content addressed first. Each chapter is self contained but builds on the concepts of previous ones. The organization of this thesis is as follows:

Chapter 1: It covers introduction and motivation for this research.

Chapter 2: A detailed description of the experimental setup used to obtain results through-

out this thesis. The hardware and software components are examined, as well as the construction of rotors made for testing.

Chapter 3: Rotor performance characteristics fully in air and fully in water are evaluated first. Blade element momentum theory (BEMT) used for analysis is introduced and factors important to rotor performance and differences between air and water are explained. The analytical results are validated against experimental data.

Chapter 4: Rotor performance in air-water transition states is described and evaluated. Key observations are made and the Transition Index (TI) is introduced as a means of characterizing rotor state using information available in flight. The applications of the Transition Index in thrust prediction and control are examined as well.

Chapter 5: A description of the HAW vehicle used to test and validate the powered rotor transition work is presented. The components particularly important for HAW applications are examined in detail and observations from flight testing are described.

Chapter 7: Conclusions about this work and suggestions for future work are described. The implications and limitations of the powered rotor in transition approach are examined.

Chapter 2: Experimental Setup

2.1 Tank Hardware

A test stand was built in order to characterize a rotor in air, water and in the air-water transition. It is designed around a large 4x4x4 ft water tank made with a welded steel frame and Plexiglas panes. The steel frame has four 45 inch long legs with heavy duty casters that enables siphon draining the tank, allows for equipment underneath the tank, a viewing location from below, and the ability to relocate the tank. The edges of the Plexiglass panes were sealed with silicone to create the watertight transparent container. The tank is filled with tap water to a depth of approximately 30 inches. A chlorine and boric acid treatment is applied to the water to prevent corrosion of submerged metal components and growth of microorganisms. The test stand with no water in the tank is shown in Figure 2.1.

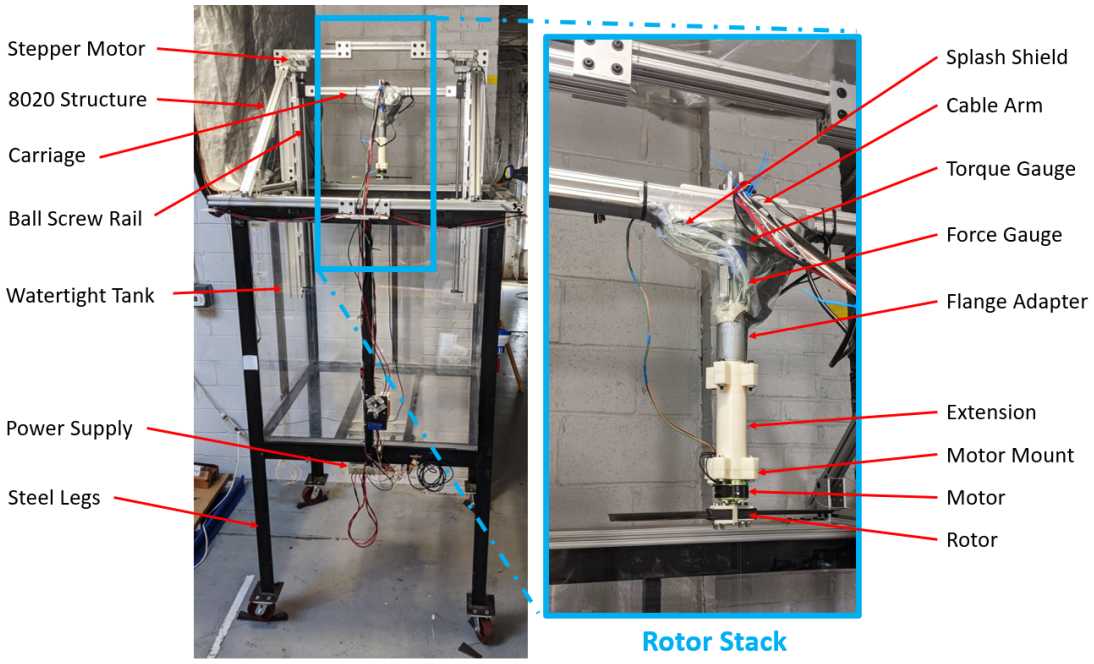

Figure 2.1: The test stand

2.1.1 Structure

The tank is outfitted with 8020 T-slot aluminum beams used for simple assembly of heavy duty aluminum structures. This construction provides support for the actuators and sensors used to conduct experiments. All 8020 beams are assembled together using 6 mm thick brackets bolted with 5/16-18 bolts and nuts. Four 3 x 1.5 inch beams are bolted to a steel flange on the perimeter of the top of the tank. Two 1.5 x 1.5 inch beams run horizontally across the top of the tank 5 inches from either side. Two upright 51 inch long 3 x 1.5 inch beams are attached to the horizontal beams at their midpoint. These two upright beams are kept perpendicular to the water by three 1.5 x 1.5 inch beam sections that connect across the top. The overall length of the three beams is adjusted to accomplish this. Two diagonal 1.5

x 1.5 inch beams run from the top of each upright to the top of the tank to provide additional stiffness.

The two upright beams are fitted with a Fuyu Technology FSL40 ball screw linear motion rail with a 1000 mm stroke. These rails support and allow for the motion of the carriage: the structural element that moves the rotor and sensors into and out of the water. Each rail is attached with 20 M4 bolts to 10 aluminum U brackets, which are in turn attached to the upright 8020 beams with 5/16-18 bolts. The rails are run by Nema 23 stepper motors. The rail slides are equipped with large aluminum U brackets to support the carriage, which is a 29.5 inch long 1.5 x 1.5 inch 8020 beam. The carriage is mounted on either end to the large U brackets with 5/16-18 bolts and allows for a minimum of 16 inches of clearance from the axis of rotation to any structural element.

2.1.2 Rotor Stack

The rotor stack is an assembly of mounting components, force and torque gauges, the motor, rotor, and splash shield. It is shown in Figure 2.1. A 15 mm thick aluminum adapter mounts a Tranducer Techniques TRT-50 torque sensor to the carriage. A 3D printed ABS force gauge to torque gauge adapter that is 1.5 inches long mounts a DYLY S-type 5 kg force gauge to the torque gauge. This force gauge is attached on the other end to another 3D printed flange adapter part that is 4 inches long. This second adapter ends in a cross shaped flange, which is common with the next several parts. Attached to that cross shaped flange is a 3D printed

extension part that is 5 inches long and has an equivalent flange on the other side. This extension part can be removed or swapped to vary the overall length of the rotor stack, it is also hollow and has holes to allow draining of any water entrained within. A 3D printed motor mount adapts a motor mounting hole pattern to the cross shaped flange. The rotating part of the motor is bolted the rotor being tested. In total, the distance from the rotor to the carriage is 16 inches, and allows for a maximum submersion depth of 9 inches.

In addition to the main components of the rotor stack there is a small arm clamped to a carbon fiber tube containing a waterproofed A3144 Hall effect sensor. This arm is attached to the motor mount and allows adjustable positioning of the Hall effect sensor to line up with magnets on various motors, which is out of view behind the rotor stack in Figure 2.1. The splash shield is a flexible plastic sheet that is attached to the extension piece and 8020 beam. It is attached with enough slack such that it does not contribute any tension to the force readings, or the cables that pass through it.

On top of the 8020 carriage there is a hinge made from aluminum brackets which attaches to a 3 ft long carbon fiber rod serving as a cable arm. The cables and wires from the rotor stack are zip tied to the rod such that there is slack in the wire between the hinge and the various components throughout the entire stroke of the rails. The unhinged end of the rod rests against the top edge of the tank and is free to move. The cables also have slack from this end of the rod to the electronic components. This setup ensures that cable tension has no effect on sensor readings during the entire range of carriage movement.

2.2 Control and Data System

The devices used to control the experimental setup and record the data from the sensors are diagrammed in Figure 2.2. The power system is omitted for clarity. First, the components that actuate the test stand are described.

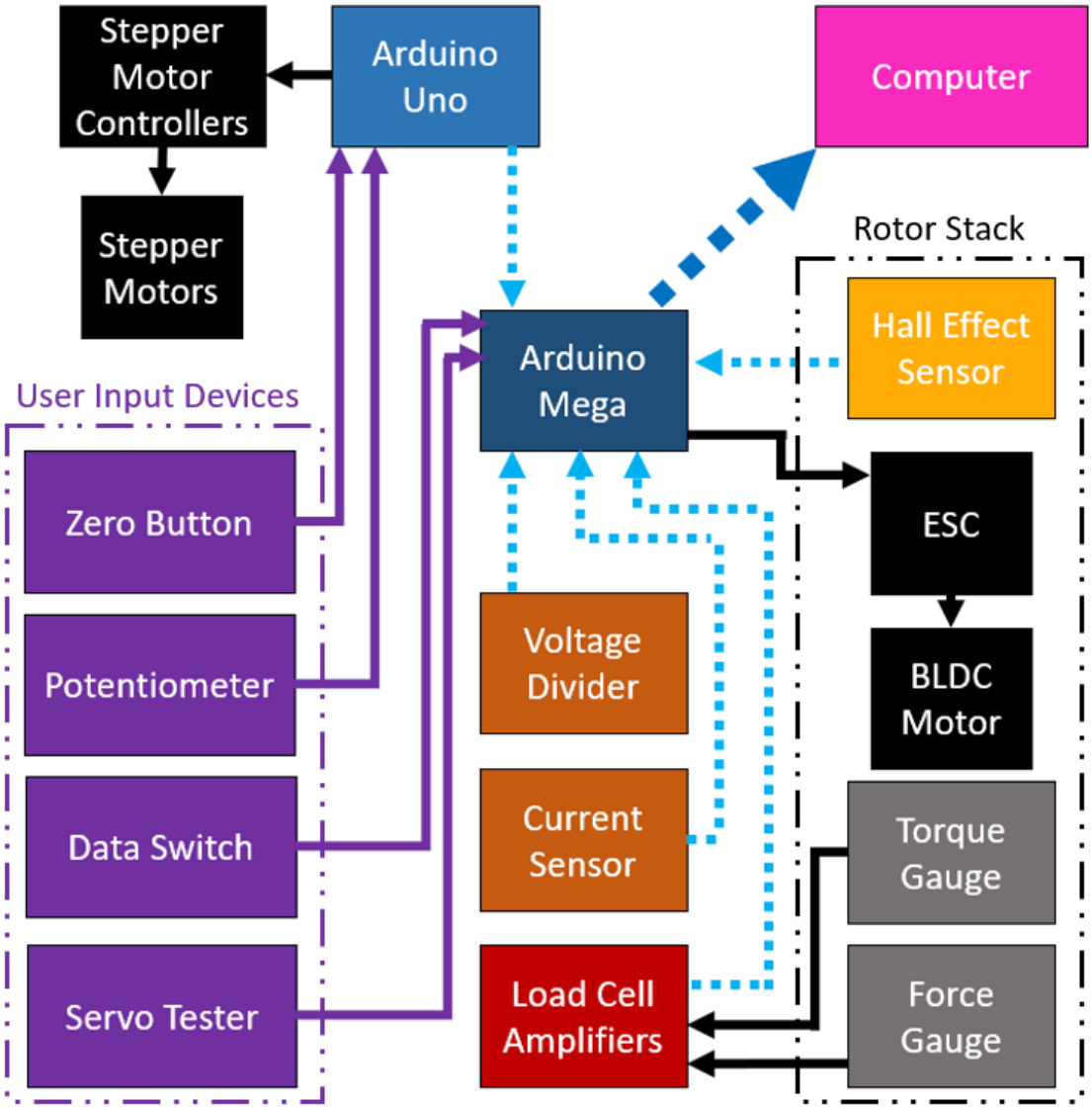

Figure 2.2: The control and data system of the test stand

2.2.1 Actuators

The brushless DC (BLDC) motor is powered by a waterproofed Castle Creations Micro Mamba X electronic speed controller (ESC). It is attached to the carriage near the top of the rotor stack, and is hidden from view behind the carriage in Figure 2.1. The ESC takes in power from a 3S battery and passes it through a series of transistors to create a commutated 3 phase signal that drives the motor. This ESC is also capable of operating sensored motors and has a port for a hall effect sensor board output to inform the commutation of the brushless motor. The speed of the motor is regulated by the throttle, which is inputted to the ESC as a pulse width modulation (PWM) signal. The user turns a knob on a HV Digital Servo Tester to throttle the motor.

The stepper motors move the carriage vertically such that the rotor can enter or exit the water. The two stepper motors are powered by a Sorensen XBT 32-3FTP DC power supply capable of 3 amps at 32 volts on two outputs. These two outputs power two StepperOnline DM542T stepper motor controllers. The stepper motor controllers input a frequency pulse and a direction signal and output a commutated signal on the 4 lines to the each side of the A and B phase coils of the stepper motors.

The digital pulse signal that controls the motor controller is generated by an Arduino Uno. The Arduino Uno uses internal clock interrupt routines using register and port manipulation commands written in C. This low level code allows for pulse generation of frequencies of up to 10 kHz and enables a maximum slide speed of 34

cm/s. The Arduino Uno controls the direction of carriage travel by outputting a digital signal. To receive user inputs the Arduino Uno samples an analog signal tied to a potentiometer. When the potentiometer is turned away from the midpoint, the direction and how far it is turned specifies the direction and speed of the carriage. This Arduino Uno not only controls the carriage, but is also part of the data system.

2.2.2 Data System

The data system is centered around a separate Arduino Mega microcontroller responsible for data collection and output. The Arduino Mega was selected due to the multiple serial communication chips it has, which allow for serial communication over USB to a laptop, as well as serial communication to the Arduino Uno which controls the stepper motors.

The stepper motor controller Arduino Uno counts the number of pulses it sends out and the direction of stepper motor travel. Each pulse corresponds to 1/200th of a centimeter of travel, which sets the maximum resolution of carriage positions. In order to determine the position of the rotor relative to the water surface, the rotor center is placed on the water surface and the zero button is pressed. This button triggers an interrupt routine in the Arduino Uno that sets the absolute position to 0. Then as the gantry is moved the number of pulses sent are added or subtracted from the absolute position depending on if the carriage was moving up or down. The absolute position is sent over serial to the Arduino Mega data collection microcontroller.

The DYLY force gauge and Transducer Techniques torque gauge are both strain gauge load cells. Strain gauge load cells wire a strain gauge across one leg of a full wheatstone bridge. This means that the strain is proportional to the voltage across the wheatstone bridge. However, due to the limitations of Arduino analog to digital converter (ADC) chips, a direct reading would not yield a satisfactory resolution. Due to this, a Sparkfun HX711 load cell amplifier breakout board is used to amplify the signal and allow for more accurate readings. The Arduino Mega records the readings by processing a two wire digital signal from the amplifiers.

Calibration of the force gauge and torque gauge was performed experimentally with a set of known weights. The torque gauge was mounted horizontally to a rigid structure and a long wooden lever arm was bolted on parallel with the ground. This lever arm allows for torque generation of known magnitudes by hanging weights at a set distance from the torque cell. The calibration results in an R^2 value of 0.999974 for the torque gauge and 0.9998 for the force gauge. The calibration results can be seen in Figures 2.3 and 2.4.

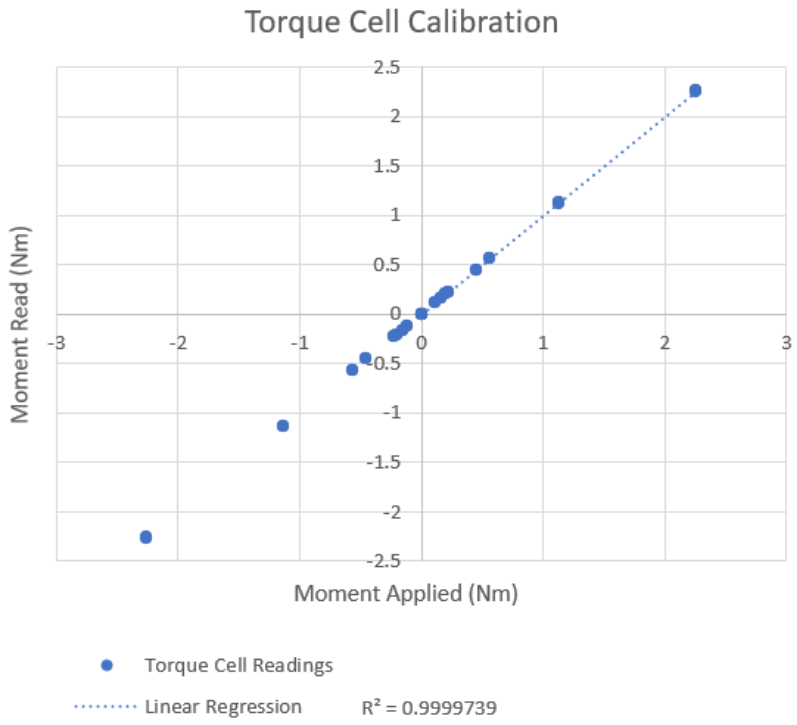

Figure 2.3: Torque gauge calibration results

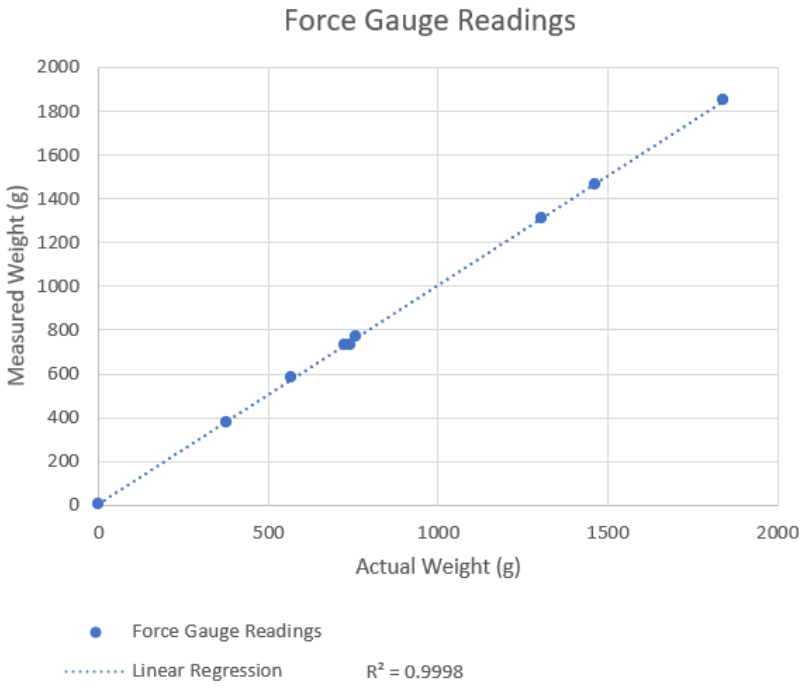

Figure 2.4: Force gauge calibration results

RPM is measured by a A3144 Hall effect sensor attached to the motor mount. Four small magnets were glued to the outside of the motor at opposite ends. The Hall effect sensor outputs a digital high signal when a magnetic field is nearby. Therefore, there are four pulses for every revolution of the motor. The rotor is directly driven by the motor so the motor revolutions per minute (RPM) is also the rotor RPM. The falling edge of each pulse triggers an interrupt routine in the Arduino Mega that calculates the time between the pulses. This period t_{pulse} is measured in seconds and converted to RPM by using Equation 2.1.

$$RPM = 15 * (1/t_{pulse}) \tag{2.1}$$

The current is measured by an Allegro ACS712 Hall effect linear current sensor which outputs a voltage that increases by 66 mV for every amp of current. This voltage is read directly by the Arduino Mega ADC and scaled to find the real current. The read current was validated against power supply readings to ensure proper function of the sensor.

The battery voltage is measured via a resistor voltage divider with an impedance lowering capacitor across the battery leads. The resistor values are 690 kΩ and 470 kΩ and the output voltage is read across the 470 kΩ resistor. A 100 nF capacitor is wired from the output to ground to lower the impedance of the voltage divider and allow for accurate ADC measurements.

The PWM throttle signal is initially generated by an HV Digital Servo Tester which the user manipulates. This throttle signal is first sent to the Arduino Mega,

where an interrupt service routine triggers every time there is a falling or rising edge. The interrupt service routine measures the current state of the signal and logs the internal clock state to find the time elapsed during the digital high state of the line. This time is known as the width of the PWM signal and is interpreted as the throttle value.

The Arduino Mega generates a separate PWM throttle signal that is sent directly to the ESC. In a standard operating mode the signal generated by the Arduino Mega is the same as the signal generated by the servo tester. However, when the feedback controller is activated the signal generated by the servo tester is used to inform the set point of the system, while the signal generated by the Arduino Mega is used to throttle the motor and drive the system to the set point.

Lastly, a data switch is used to signify important data points. The status of this switch is recorded by the Arduino Mega to simplify data post processing.

The DC power supply outputs a regulated 5 volts on a tertiary output that powers the load cell amplifiers, Hall effect sensor, current sensor, user input devices, and both Arudinos. The regulated supply voltage ensures analog signals are as accurate as possible.

The Arduino Mega compiles the current, voltage, torque, thrust, throttle, carriage position, and data switch status and sends this information over serial to a laptop along with a timestamp. When the controller is activated additional information such as throttle input, throttle output, and other diagnostic controller information is included. The laptop uses a serial monitor program to save all the data sent by the Arudino Mega to a text file for post processing. Initial post pro-

cessing is done with Microsoft Excel macros to isolate data of interest and identify outliers, final post processing is done with Mathworks MATLAB to generate plots and perform calculations.

With these devices the a user is able to control the motor throttle and carriage speed to collect experimental data. Additionally the feedback controller can be enabled to modulate the throttle during transition.

2.3 Waterproofing

To ensure the dependability of the equipment used in the tank, some waterproofing measures were taken. Some of the processes described here also apply to waterproofing the vehicle.

Some of the aluminum 8020 upright beam sections, U brackets, mounting hardware, and portions of the ball screw rail are submerged or near the water line. These metal components will corrode due to repeated exposure to air and water, especially near the water line itself. To combat this CorrosionX dielectric compound is applied to the exposed metals. CorrosionX protects the metal surfaces from rust, provides electrical insulation, and adds lubrication for the rail. CorrosionX and other chemicals used for waterproofing are shown in Figure 2.5.

Figure 2.5: Waterproofing chemicals used on the test stand

The Hall effect sensor is a small board mount 3 prong chip, in order to waterproof it and maintain its function a Fine-L-Kote HT silicone conformal coating is applied. This flexible, thin, waterproof, dielectric coating allows the hall effect sensor to function completely submerged. In order to waterproof the wiring leading to the sensor and add a rigid protective casing a carbon fiber tube is used. The hall effect sensor leads are placed into the tube while the sensor itself remains exposed. The tube is then filled with molten hot glue, when hardened the wiring is insulated from the water and strengthened.

The ESC is attached to the carriage and therefore not susceptable to submersion. However, it is waterproofed in the same manner as the ESCs on the vehicle, which do get submerged. Castle Creations Micro Mamba X ESCs have some mea-

sure of waterproofing from the manufacturer, however they are only rated for splash protection. Additional waterproofing is achieved by disassembling the ESC casing to isolate the circuit board. The circuit board is then covered in a Fine-L-Kote HT silicone conformal coating. Once dry, the casing is reattached and exposed leads are coated in silicone sealant. Additionally, the on-off switch is placed in the on position and sealed in silicone as well.

A typical BLDC motor is fundamentally made out of coils of wire and permanent magnets, and will work underwater with no modifications because no semiconductor devices or shorting risks are present. However, if waterproofing is not applied, corrosion will occur and can degrade the function of the motor over time. Additionally sensored motors are a subcategory of BLDC motors that feature circuit boards with Hall effect sensors and often temperature sensors. These boards are susceptible to shorting and will fail in water.

For use on the test stand, BLDC motors are waterproofed by adding CorrosionX HD dielectric grease to all surfaces. Standard CorrosionX has a low viscocity and the rapid rotation of the motor displaces it, CorrosionX HD is more viscous and does not get displaced by the motor rotation. Sensored motors undergo the same treatment, with additional Fine-L-Kote HT silicone conformal coating on the circuit boards.

2.4 Rotors

Rotors were created with known airfoil sections and geometric properties to develop the analytical model. Due to the high loads in underwater operation, special attention was paid to the structural integrity of the rotor blades and hub during design and manufacture.

Two airfoil sections are chosen for validating the analysis, a flat plate and a 10% cambered plate. Both plate airfoil sections allow manufacturing consistency and provide contrasting symmetric and strongly cambered airfoils for insight in the performance of both airfoil types. Additionally at this scale (up to 15 inches in diameter) many commercial rotors have cambered or flat plate airfoil sections, meaning the manufactured rotors will simulate commercial models well.

The rotor hub is designed as an assembly of a hub frame with a fixed pitch set by a modular pitch setting block component. This allows many pitch angles to be set for both the cambered and flat plate airfoil. The various parts can be seen in Figure 2.6: (a) A single pitch setting block, (b) Cambered and flat plate pitch setting blocks at 5° ,10°,and 15°, (c) The hub frame, (d) An assembled hub.

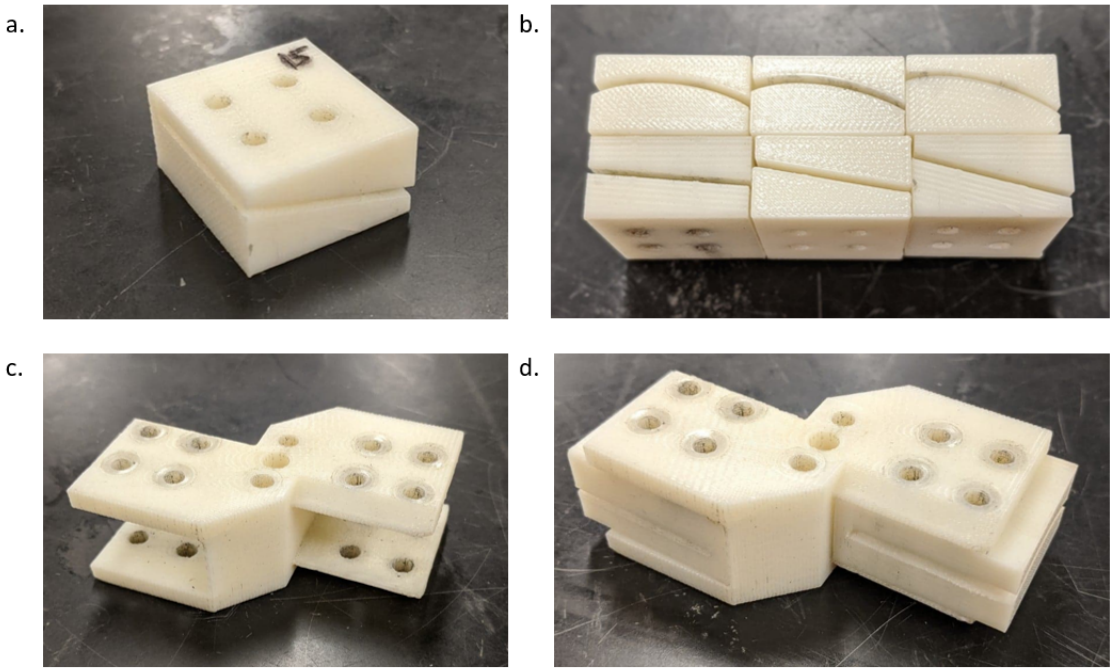

Figure 2.6: Rotor hub components

The rotor hub is 3D printed out of high strength ABS and features prongs and a standardized mounting hole pattern to accept the pitch setting blocks. The height between the prongs is chosen to fit up to a 35° flat plate pitch block. The blocks are likewise 3D printed out of high strength ABS and are designed to fit into the prongs at any pitch setting. The change in the lateral position of the 3/4 chord at different pitch angles is accounted for in the pitch setting blocks, their hole patterns are positioned such that the 3/4 chord line of both rotor blades is in-plane with the axis of rotation. This ensures proper balancing of the blades and minimizes variance between pitch settings and airfoil types. The hub was validated using finite element analysis (FEA) to ensure failure would not occur.

Three sets of rotor blades are made from custom layups of pre-pregnated (prepreg) carbon fiber sheets and one set is made from aluminum. The blades can

be seen individually in Figure 2.7, their properties are tabulated in Table 2.1, and an assembled rotor is shown in Figure 2.8.

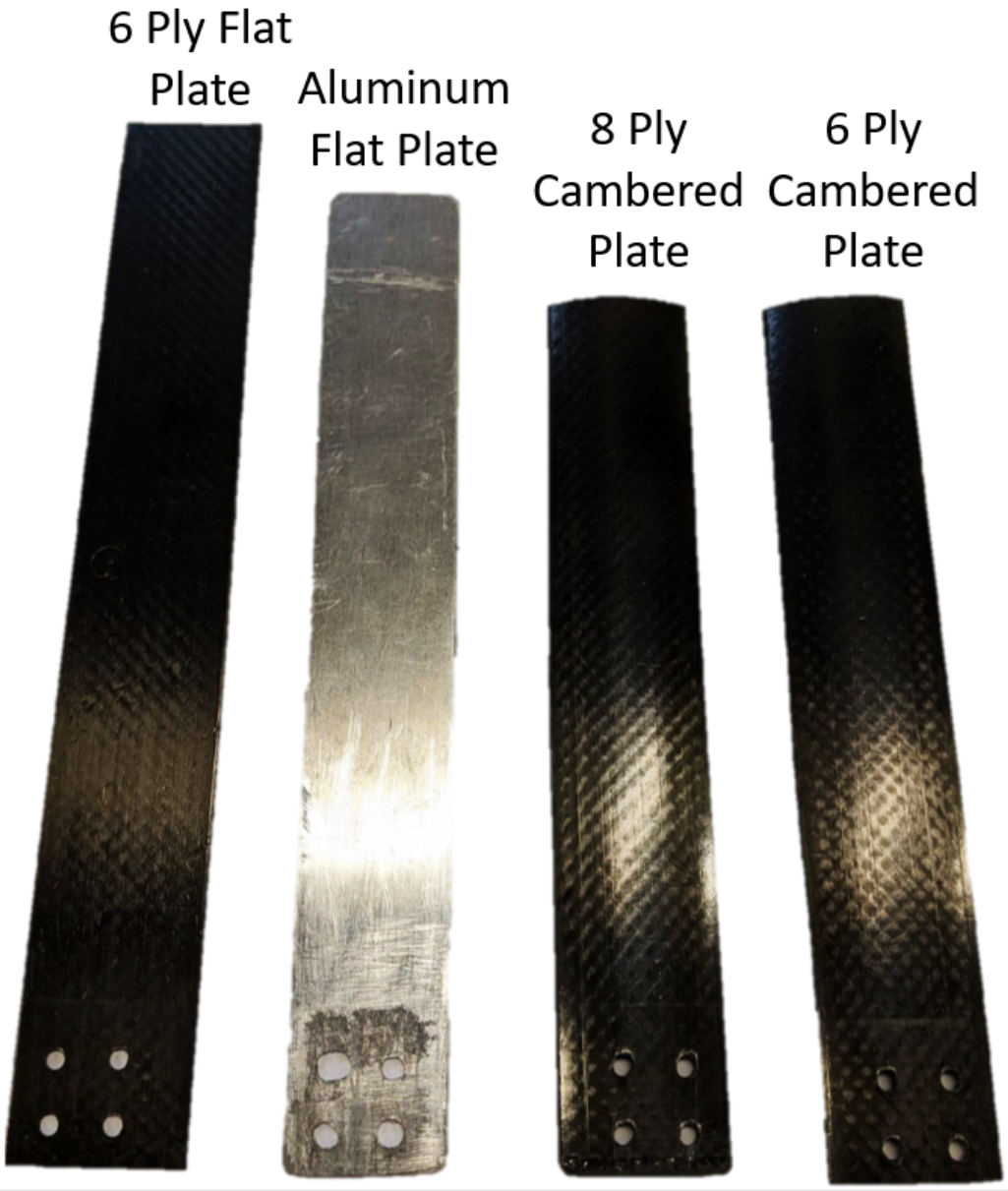

Figure 2.7: The various rotor blades made for testing

Figure 2.8: An assembled test rotor

Two types of prepreg were used: the first is a ±45° Hexcel HexPly IM7/8552 SPG 196-P graphite/epoxy weave with a cured ply thickness of 0.2 mm. The second is a 0° Hexcel HexPly CMH-17 IM6 12k/3501-6 unidirectional tape with a cured ply thickness of 0.15 mm.

The aluminum set of rotor blades has a flat plate airfoil. The high isometric strength of aluminum made it desirable for stability under the high loads of

submerged water operation.

Table 2.1: List of Manufactured Rotors

	6 Ply Flat Plate	Aluminum Flat Plate	6 Ply Cambered Plate	8 Ply Cambered Plate
Length (in)	7.5	7	6	6
Width (in)	1	1	1	1
Material	$[0°, 0°, \pm 45°]_S$	6061 Aluminum	$[0°, 0°, \pm 45°]_S$	$[0°, 0°, \pm 45°, \pm 45°]_S$
Thickness (mm)	1.1	1.24	.87	1.3
EI (Nm^2)	.151	.299	.91	1.6
GJ (Nm^2)	.046	.416	.04	.14
M (g)	7.1	16	5	7.2

Chapter 3: Fully in Air and Water Rotor Dynamics

3.1 Introduction to BEMT modeling

To understand the significant differences between rotor operation in air and water Blade Element Momentum Theory (BEMT) is used. By modeling known rotors in fully in air and fully in water conditions and comparing predicted results with experimental data important insights can be obtained.

BEMT is an analytical framework to estimate rotor thrust and power by calculating the inflow and resulting angle of attack over a range of blade elements. This approach eliminates 3D aerodynamic effects and assumes the rotor blade is composed of 2D airfoil sections, which allows for a simple and accurate theoretical performance predictions.

The advantages of this approach lie in the categorization of rotor forces from various sources, the opportunity to use detailed airfoil tables, and the flexibility to include effects such as tip-loss and elastic deformation. These advantages allow for the comparison of the significance of various effects on the rotor performance in different conditions.

3.1.1 Inflow

Fundamental to BEMT is the determination of the non-dimensional inflow velocity λ, it is derived by equating incremental thrust coefficients dC_T produced by an annulus of the rotor disk from momentum theory (MT) and blade element theory (BET). In momentum theory, the Froude-Finsterwalder equation can be used to derive Equation 3.1 where λ_c is the non-dimensional climb velocity [20]. Because the rotor is assumed to be in hover for these analysis $\lambda_c = 0$.

$$dC_T = 4r\lambda(\lambda - \lambda_c)dr \tag{3.1}$$

In order to account for the loss of lift at the tip of the blade, Prandtl's tip loss factor F is applied given by Equation 3.2.

$$F = \frac{2}{\pi}\cos^{-1}(e^{N_b/2(1-r/r\phi)}) \tag{3.2}$$

This turns Equation 3.1 into Equation 3.3.

$$dC_T = 4Fr\lambda^2 dr \tag{3.3}$$

BET and BEMT approaches characterize a blade element as a 2D airfoil section subject to a relative air velocity U. The resulting angle of attack α drives the lift and drag forces generated by the airfoil. The various components of U and relevant angles are depicted in Figure 3.1.

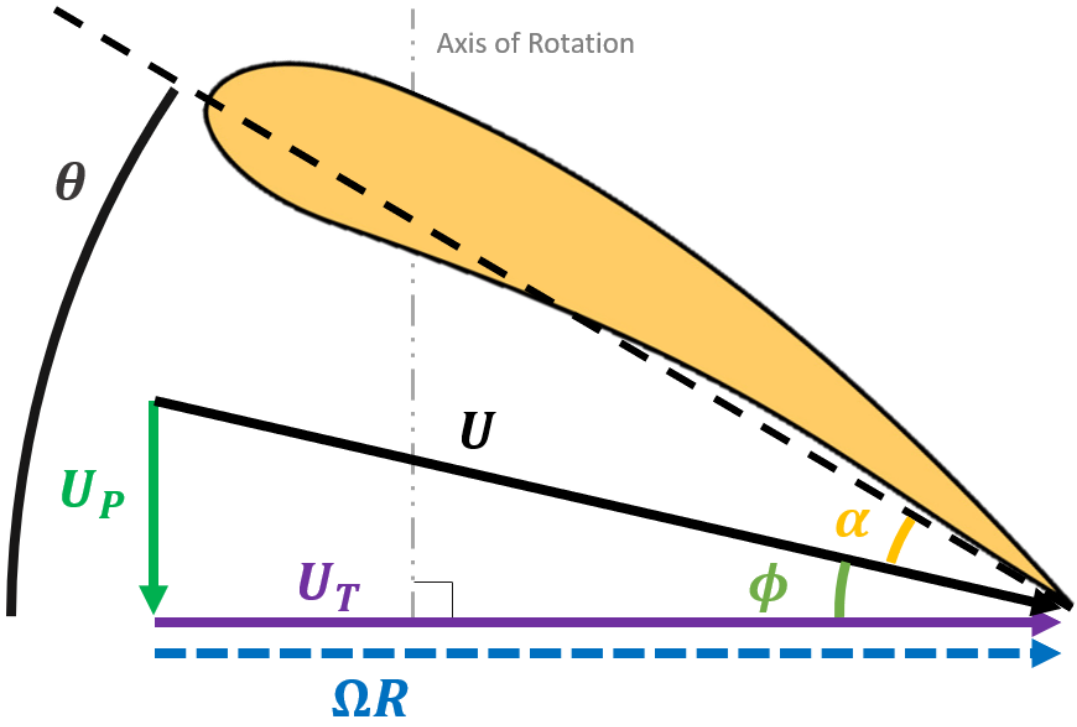

Figure 3.1: Component air velocities relative to a 2D airfoil section

From BET, the inclusion of the lift curve slope C_{l_α} allows the derivation of Equation 3.4.

$$dC_T = \frac{1}{2}\sigma C_{l_\alpha}(\theta r^2 - \lambda r)dr \tag{3.4}$$

Equating the right side of Equations 3.3 and 3.4 results in a quadratic equation in λ which has the solution shown in Equation 3.5 when $\lambda_c = 0$.

$$\lambda = \frac{\sigma C_{l_\alpha}}{16F}\left(\sqrt{1 + \frac{32F}{\sigma C_{l_\alpha}}\theta r} - 1\right) \tag{3.5}$$

Equation 3.5 does not have an algebraic solution for λ because F is a function of λ. Therefore fixed point iteration is used.

The inflow equation (Equation 3.5) is the fundamental equation which allows for the calculation of the velocity U_P and therefore determination of α at each blade element. α is critical to the calculation of the forces on the airfoil section.

3.1.2 Forces

The airfoil generates an aerodynamic force distribution along the blade which is broken down into a lift component dL and drag component dD at each blade element. These forces are diagrammed in Figure 3.2 and defined in Equations 3.6 and 3.7. The direction of drag is parallel with the incident air velocity U, and lift is perpendicular.

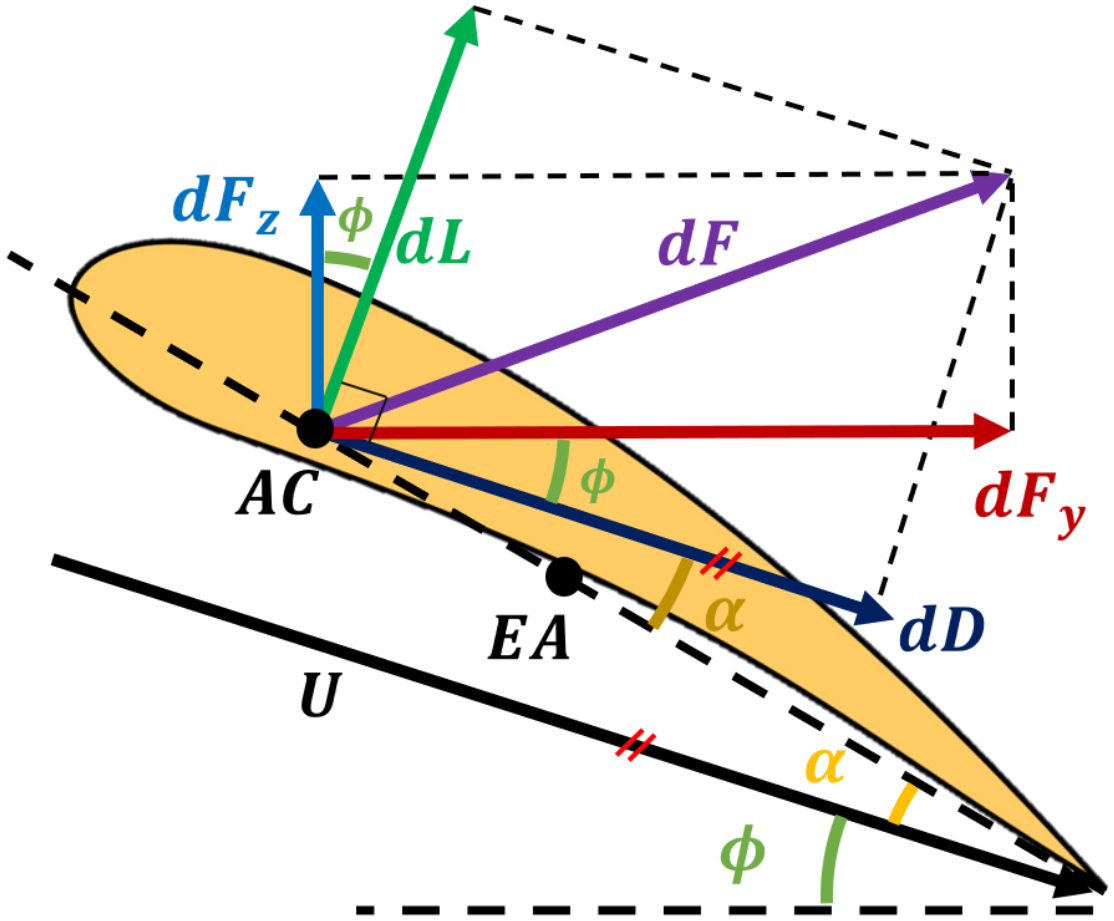

Figure 3.2: Diagram of airfoil force definitions

$$dL = \frac{1}{2}\rho U^2 c C_l dy \tag{3.6}$$

$$dD = \frac{1}{2}\rho U^2 c C_d dy \tag{3.7}$$

In order to obtain rotor thrust and torque requirements, the lift and drag must be transformed into forces acting parallel with and perpendicular to the axis of rotation, labeled dF_z and dF_y respectively. The definition of these forces is shown in Equations 3.8 and 3.9.

$$dF_z = dL\cos\phi - dD\sin\phi \tag{3.8}$$

$$dF_y = dL\sin\phi + dD\cos\phi \tag{3.9}$$

3.1.3 Moments

In addition to lift and drag the airfoil produces an aerodynamic moment distribution along the blade. The blade element differential aerodynamic moment is dM_{aero} and is defined in Equation 3.10, and its positive direction is depicted in Figure 3.2.

$$dM_{aero} = \frac{1}{2}\rho U^2 c^2 C_m dy \tag{3.10}$$

While dM_{aero} is the only moment applied directly to the blade element, it is useful to identify dM_{tot}, the total moment about the neutral axis of the rotor blade. The forces and moments relevant to dM_{tot} are diagrammed in Figure 3.3.

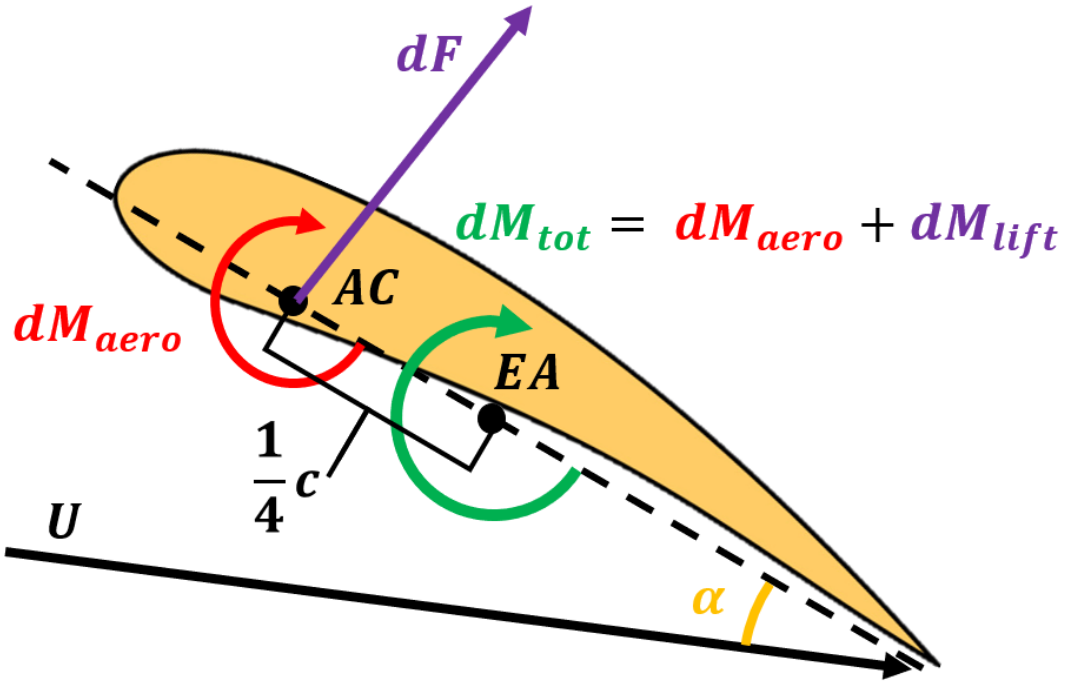

Figure 3.3: Diagram of airfoil moment definitions

The aerodynamic forces are assumed to act on a single point at the aerodynamic center of the airfoil, labeled AC. Because the airfoils analyzed are thin, it is assumed that AC is at a constant location at the 1/4 chord. When elastic effects are considered, the rotor blade is assumed to be a non-uniform beam. Because the airfoils analyzed are thin, symmetric about the half chord, and have a constant thickness, the elastic axis EA of the beam is assumed to be at the half chord. Therefore, the moment acting about the elastic axis includes the moment created by the aerodynamic forces dM_{lift}, defined in Equation 3.11, as well as the aerodynamic moment dM_{aero}. The differential total moment dM_{tot} about NA is then defined by Equation 3.12.

$$dM_{lift} = \frac{c}{4}(dL\cos\alpha + dD\sin\alpha) \tag{3.11}$$

$$dM_{tot} = dM_{lift} + dM \tag{3.12}$$

When elastic effects are ignored and the blade is assumed to be rigid the moment has no effect on the thrust and torque of the rotor. In the rigid case $\theta = \theta_{tw}(r) + \theta_0$, $dFz = dT$ and $U_P = v_i$. These definitions change when elastic effects are included.

3.1.4 Elastic Effects

The inclusion of elastic effects accounts for blade flap (out of plane bending) and blade twist due to torsion. Blade lead-lag (in plane bending) is ignored due to the high bending stiffness of the analyzed rotors in that direction and low sensitivity of lead-lag on steady rotor thrust and torque in hover conditions.

Using the equations described in Sections 3.1.1, and 3.1.2 a bending force and a twisting force at each blade element are found as dFz and dM_{tot}. These forces are used in the determination of the static bending and twisting deformation distributions $w(r)$ and $\theta_f(r)$ of the blade via the finite element method (FEM).

FEM is used for both bending and torsional deflection analysis by using 6 nodal degrees of freedom, 4 for bending and 2 for torsion. Hermite polynomials are used to describe the shape function and calculations are performed using Legendre-Gaussian integration.

Because only the static response is of interest in the analysis, the kinetic energy and therefore mass matrix are ignored in both cases. In the bending deflection calculation the rotation of the rotor is accounted for in addition to bending stiffness at each element station. In the torsional deflection calculation only the rosional rigidity is considered.

FEM returns a twisting deflection distribution $\theta_f(r)$ caused by the torsional moment dM_{tot} at each element. The resulting pitch angle at each blade element $theta$ is therefore described by Equation 3.13, where θ_{tw} is the built in rotor blade twist and θ_0 is the collective pitch setting.

$$\theta = \theta_{tw}(r) + \theta_f(r) + \theta_0 \tag{3.13}$$

Furthermore, the flap of the blade impacts the transformation of velocities and forces in a frame relative to the airfoil shown in Figures 3.1 and 3.2 into a frame relative to the rotor when determining rotor thrust and torque. The bending angle of the deformed blade element relative to the undeformed blade at span-wise location r is written $\tan^{-1}\frac{dw(r)}{dr} \approx \frac{dw(r)}{dr}$ when the angle is small. In the presence of flapping deformation $dT \neq dF_z$. Figure 3.4 and Equation 3.14 describe the new relationship.

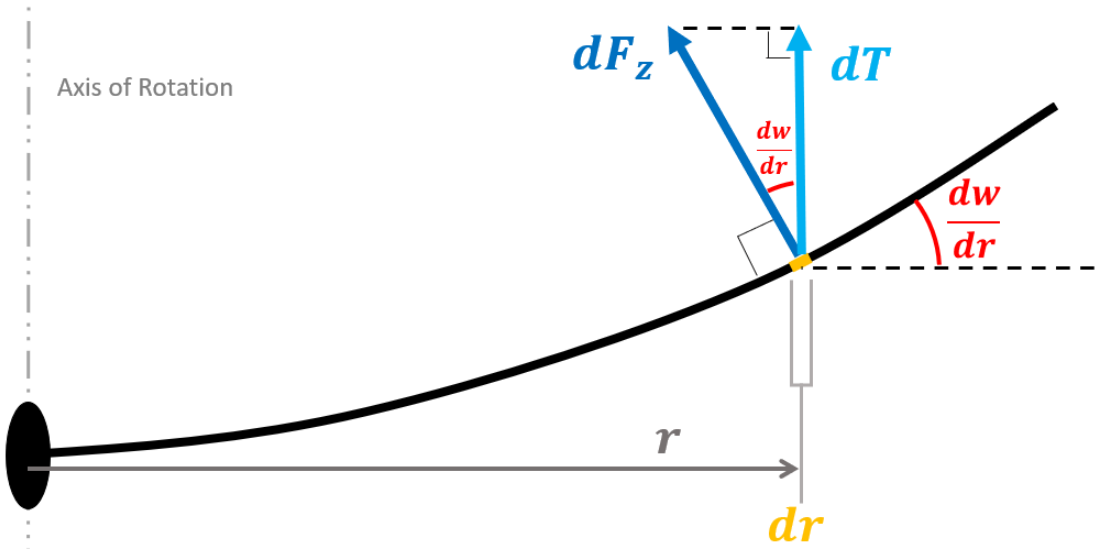

Figure 3.4: Diagram of bending angle impact on thrust

$$dT = dF_z \cos \tan^{-1} \frac{dw(r)}{dr} \tag{3.14}$$

3.2 Airfoil Considerations

To determine the thrust and torque of the rotor in the above equations C_l, C_d, and C_m are necessary. These values are functions of angle of attack α and are dependent on the airfoil. Due to both the small scale of the rotors (up to 15 inches in diameter) and the variable medium they operate it, the encountered Reynolds numbers vary significantly and tend to be below 200,000. As a result, the airfoil lift, drag and moment coefficients are considered functions of Reynolds number as well as angle of attack. Reynolds number is defined by Equation 3.15 where L is the characteristic length, which is the chord length ($L = c$) in the case of 2D airfoil sections.

$$Re = \frac{UL}{\nu} \tag{3.15}$$

The kinematic viscosity ν is the dynamic (or absolute) viscosity normalized by the density. For air and water at 25° C ν is 0.893e-6 and 15.52e-6 m^2/s respectively. However due to the higher power required the rotor speed in water is roughly an order of magnitude lower than in air at the same throttle. This impacts the U term in Equation 3.15 proportionally. As a result, the Reynolds number in water is roughly 60% larger in water than it is in air since $Re_{water}/Re_{air} \approx 10\nu_{air}/\nu_{water}$.

3.2.1 Flat Plate

The C_l and C_d of a flat plate airfoil are not sensitive to Reynolds numbers at the values encountered at this rotor scale [21]. As a result the flat plate airfoil force and moment coefficients are not considered to be functions of Reynolds number.

Airfoil tables were generated using experimental flat plate data collected by Okamoto et al. at Re in the range: 11,000 - 15,000 [22]. The resulting C_l, C_d, and C_m curves are shown in Figure 3.5.

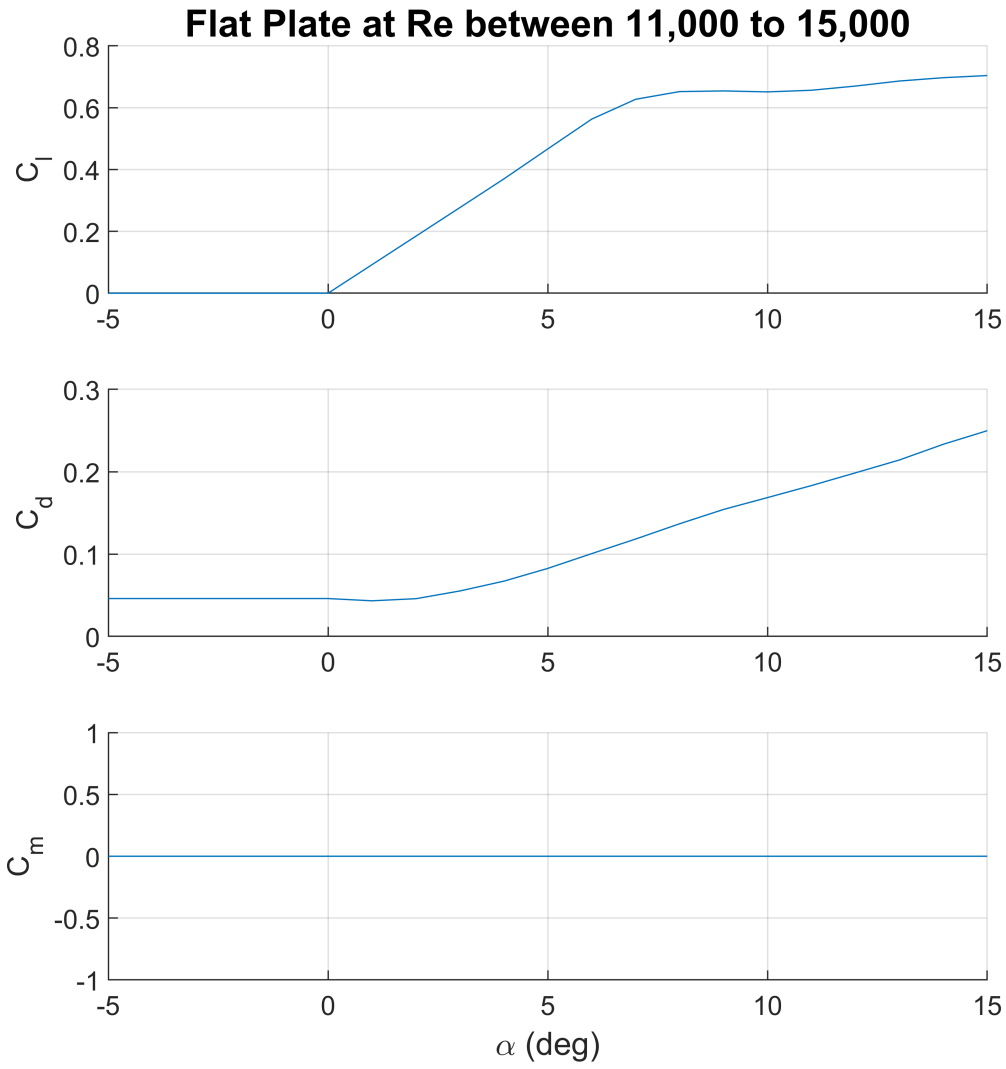

Figure 3.5: Flat plate airfoil properties based on Experimental data by Okamoto et al. [22]

3.2.2 Cambered Plate

To determine the airfoil characteristics the specific cambered plate airfoil made for testing was measured and input into a Navier-Stokes computational fluid dynamics (CFD) solver called TURNS2D. This program outputs the C_l, C_d, and C_m and various angle of attacks and Reynolds numbers. Meshing was performed using an

O-grid approach due to the blunt trailing end. The 10% cambered plate airfoil and near grid can be seen depicted in Figure 3.6. It should be noted that although the leading and trailing edge shapes are accurately modeled, the overall thickness of the physical airfoil sections varies along the surface of the blade and between blades from the manufacturing process, which is not represented in the model.

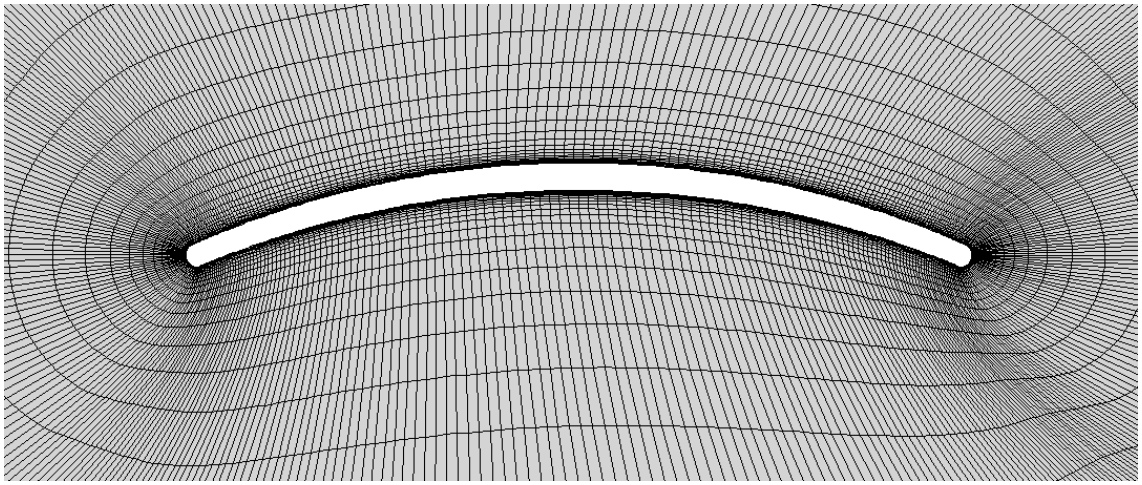

Figure 3.6: O-grid for the cambered plate airfoil

The resulting force and moment coefficients found by TURNS2D for the cambered plate airfoil at Reynolds numbers of 10,000 - 200,000 are shown in Figure 3.7.

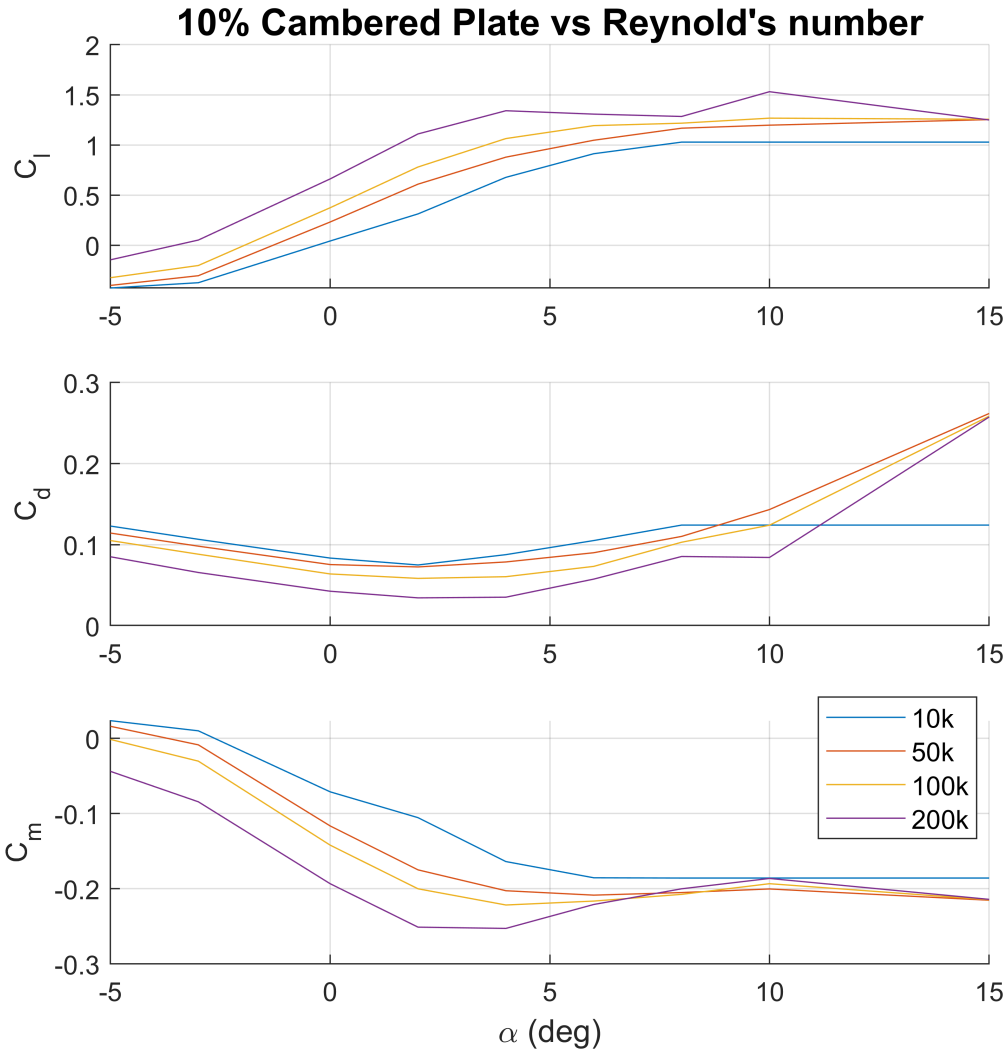

Figure 3.7: TURNS2D results for the cambered plate airfoil

It can be seen in Figure 3.7 that the cambered plate performance is sensitive to Reynolds number effects. Notably, as Re increases the zero lift angle magnitude also increases. This is the angle at which the airfoil C_l is 0, a more negative number suggests a larger impact of camber. This can also be seen as C_l generally increases with increasing Re. Additionally, C_d generally decreases with increasing Re which points to a much higher C_l/C_d for cambered airfoils at higher Re. However, the

stall angle after which the C_l/α slope drops is lower at higher Re. C_m also increases in magnitude and is negative at higher Re indicating that the airfoil will produce a larger pitch down moment as well. The effect of Reynolds number on a cambered airfoil is visualized in Figures 3.8 and 3.9. The pressure distribution found by TURNS2D and streamlines are depicted. Locations where streamlines spiral and overlap appear darker and indicate a zone of sperated flow. It can be seen that at 200,000 Reynolds number the separated zones underneath and behind the airfoil are smaller and the pressure distribution is significantly different than the 10,000 Reynolds number case. Notably the large separated zone underneath the airfoil at 10,000 Reynolds number causes lower pressures, minimizing the pressure difference between the top and bottom of the airfoil. This effect on pressure causes the changes in C_l seen in Figure 3.7.

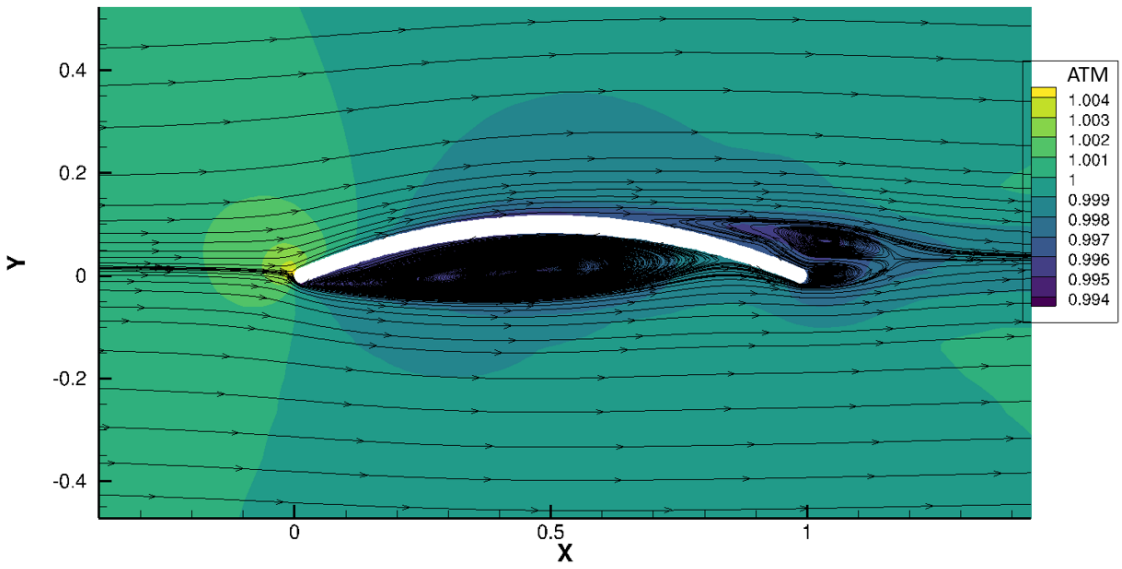

Figure 3.8: Streamlines and pressure distribution of 10 % cambered plate airfoil at 10,000 Reynolds number and 0° angle of attack

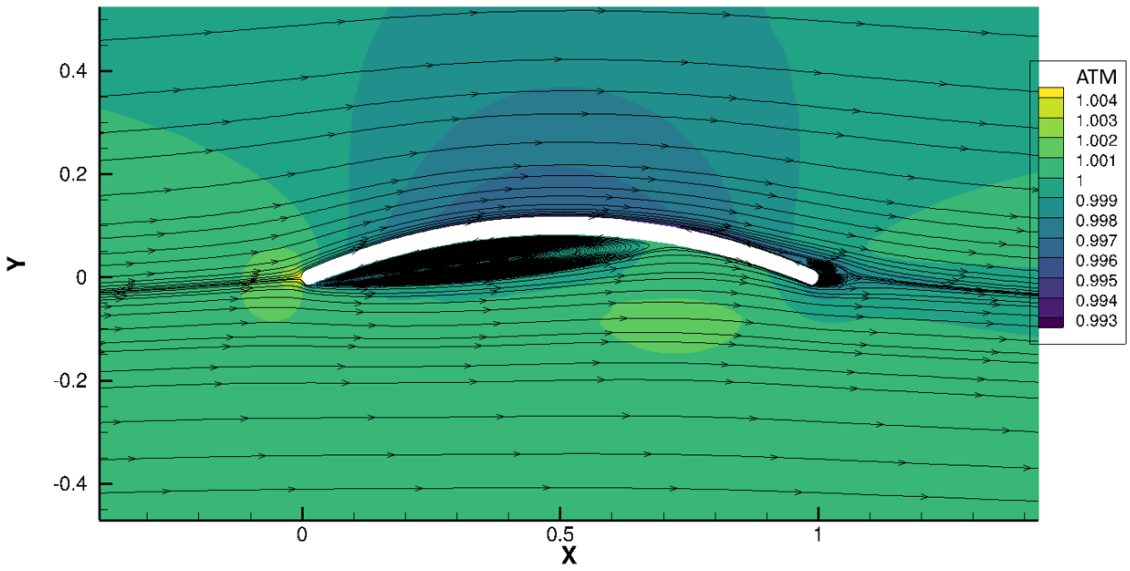

Figure 3.9: Streamlines and pressure distribution of 10 % cambered plate airfoil at 200,000 Reynolds number and 0° angle of attack

3.3 Comparison with Experimental Data

Experimental thrust, torque and rpm data of the custom blade rotors were collected in fully in air and fully in water conditions. Some observations made during testing are described below. The rotor was also modeled using BEMT as described above in Section 3.1 using experimental airfoil data and CFD generated airfoil tables described in Section 3.2 and the results are compared with experimental data below.

3.3.1 Experimental Observations

The four manufactured rotor blades described in Chapter 2 were tested at 5°, 10°, and 15° collective pitch settings in air and water. It was found that the 6 ply composite blades had insufficient structural strength to demonstrate nominal

performance in the water. Both exhibited large deflections and were sensitive to the length of the rotor stack assembly mounting the rotor to the structurally stiff test stand carriage.

Additionally, the large deflections caused vibration of the rotor stack, which added significant noise to the data collected.

While the data is invalidated by the structural issues of these rotors, the observations demonstrate the importance of a structurally strong and stiff rotor for water applications. The 6 ply composite blades have the lowest torsional rigidity of the rotors tested (), indicating that torsional rigidity is an important consideration for aerial rotors operating in the water. Additionally, many aerial rotors are flexible and rely on centrifugal stiffness to minimize bending deformation. This approach is valid in the air, where the operating speed is generally large (thousands of RPM). However, in the water the same thrust is produced when the operating RPM in water is an order of magnitude lower, reducing centrifugal stiffness considerably.

Furthermore, during testing an oscillatory deflection phenomenon was observed at 15° pitch conditions in the water with the 6 ply composite flat plate rotor. It can be observed in the video stills shown in Figure 3.10. These oscillations are not sensitive to the addition of a leading edge weight equal in mass to the unaltered blade. The lack of sensitivity of this phenomenon to the chordwise location of the blade center of gravity indicates it is unlikely to be flutter. This phenomenon is not fully understood, and was avoided by the use of the aluminum flat plate blade, which has a significantly larger torsional stiffness.

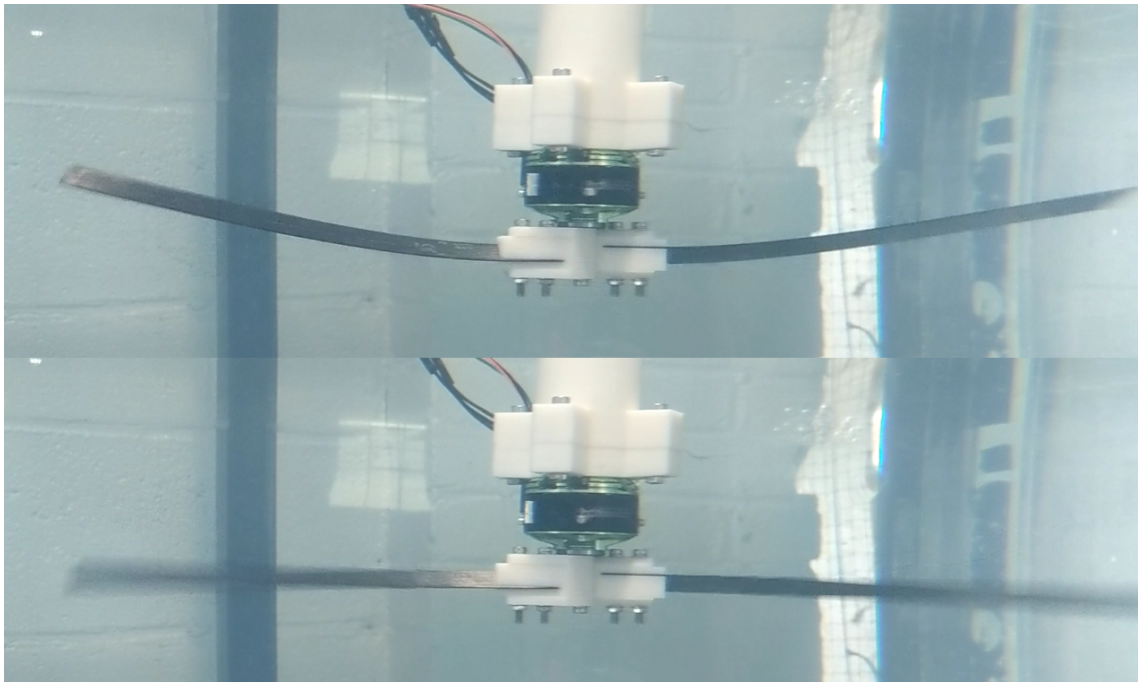

Figure 3.10: Successive video frames showing oscillatory deflection of carbon composite flat plate blade in water

3.3.2 Flat Plate Rotor

3.3.2.1 Air

The rotor thrust and power versus RPM in the air can be seen in Figures 3.11 and 3.12 respectively.

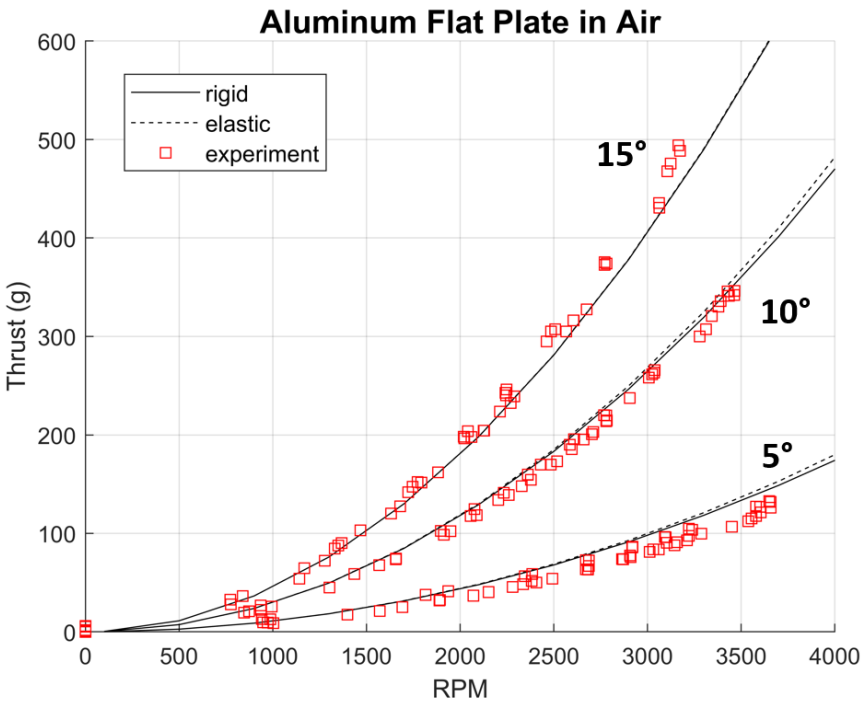

Figure 3.11: Aluminum flat plate rotor thrust in air

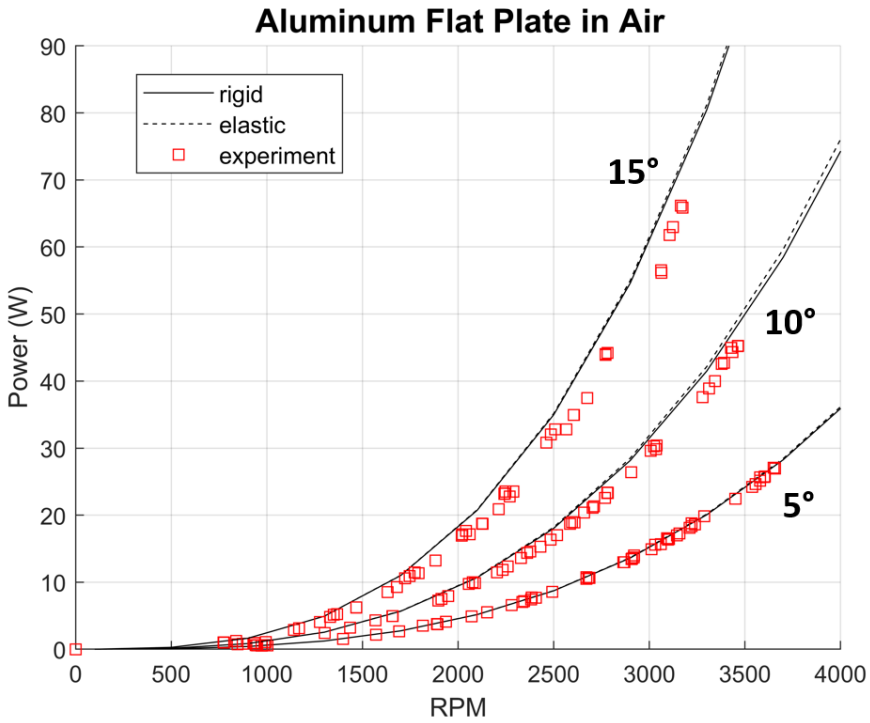

Figure 3.12: Aluminum flat plate rotor power in air

BEMT reasonably predicts the thrust and power at all three pitch cases. It can be seen that the impact of elasticity on the results in the air is minimal.

3.3.2.2 Water

The flat plate rotor thrust and power in the water can be seen in Figures 3.13 and 3.14 respectively.

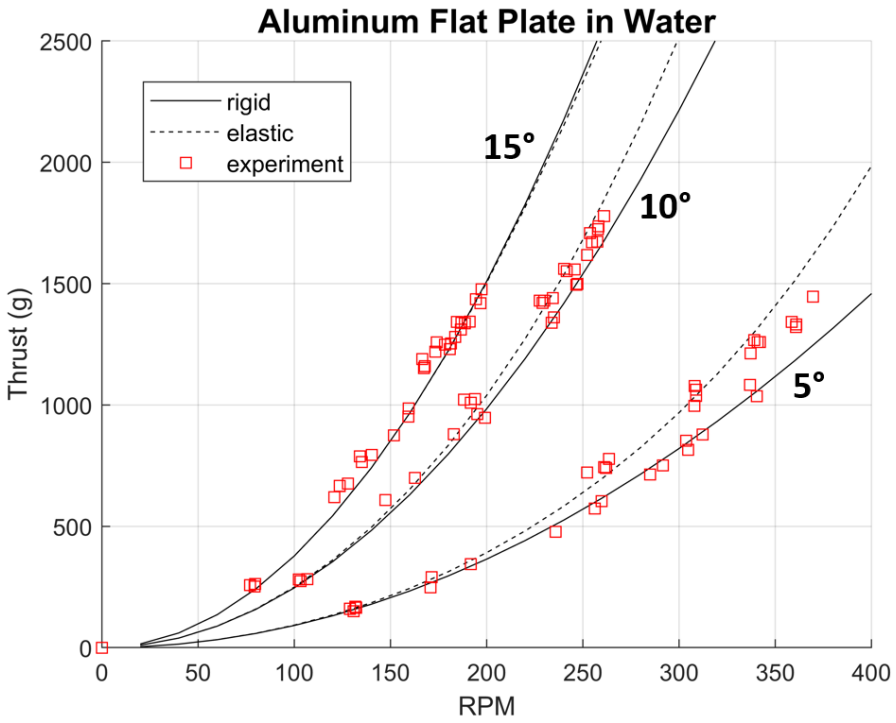

Figure 3.13: Aluminum flat plate rotor thrust in water

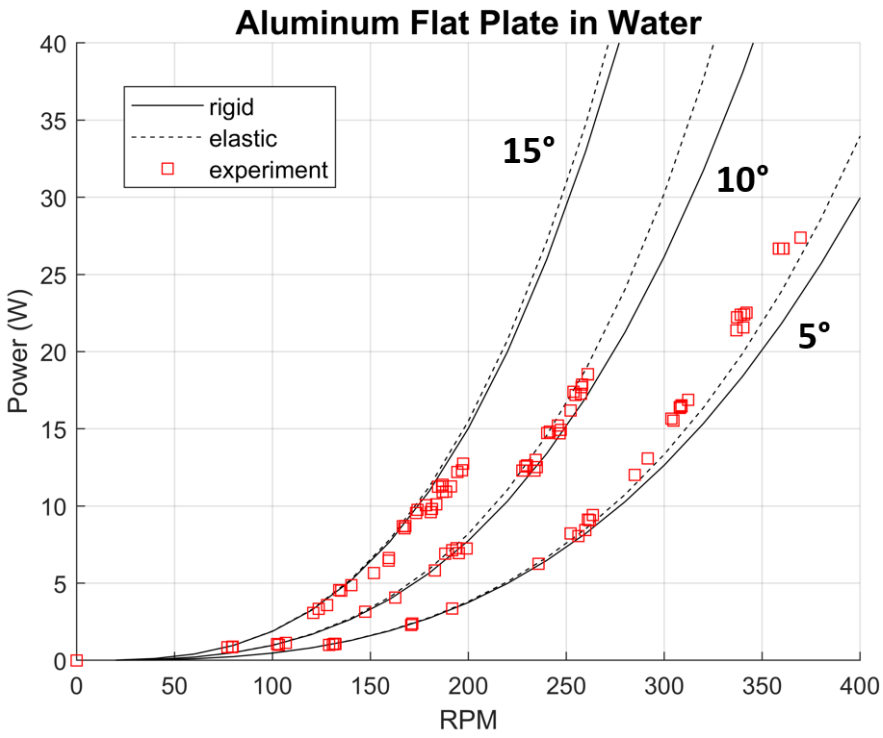

Figure 3.14: Aluminum flat plate rotor power in water

The effect of elastic deformation on rotor performance in the water is evident. BEMT predicts a large impact of elasticity on thrust at low pitch settings, this is confirmed by the experimental results by comparing the difference between the rigid theoretical performance and the experimental data. In the air rigid BEMT results overpredict the thrust by roughly 10% at the highest RPMs, however in the water the rigid BEMT results underpredict the thrust by roughly 10%. This suggests that the difference is caused by elastic effects in the experimental data.

Elastic effects at higher pitch settings are found to have a smaller relative impact. This is due to the minimized sensitivity of the flat plate C_L to changes in $/alpha$ after stall. To illustrate this, the 5° and 15° pitch cases are compared at 300 and 160 RPM respectively. At these rational speeds the thrust predicted with

elastic BEMT analysis is the same for both pitch settings. Because the thrust is similar, so too is the twisting moment and the resulting $\theta_f(r)$. The twist deflection between the two cases is within 0.1° as seen in Figure 3.15. However, because the angle of attack of the 15° pitch case is larger and the airfoil is already in stall, the twist has a smaller effect. This is evidenced in Figure 3.16 where the C_L distribution difference between elastic and rigid cases is shown. The 5° pitch case experiences a larger change in C_L which results in a larger change in thrust.

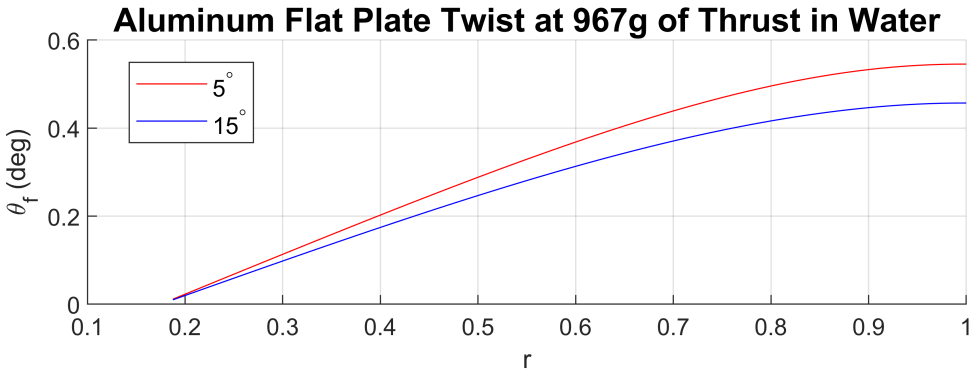

Figure 3.15: Elastic twist distribution of aluminum flat plate rotor at at 5° and 15° pitch settings

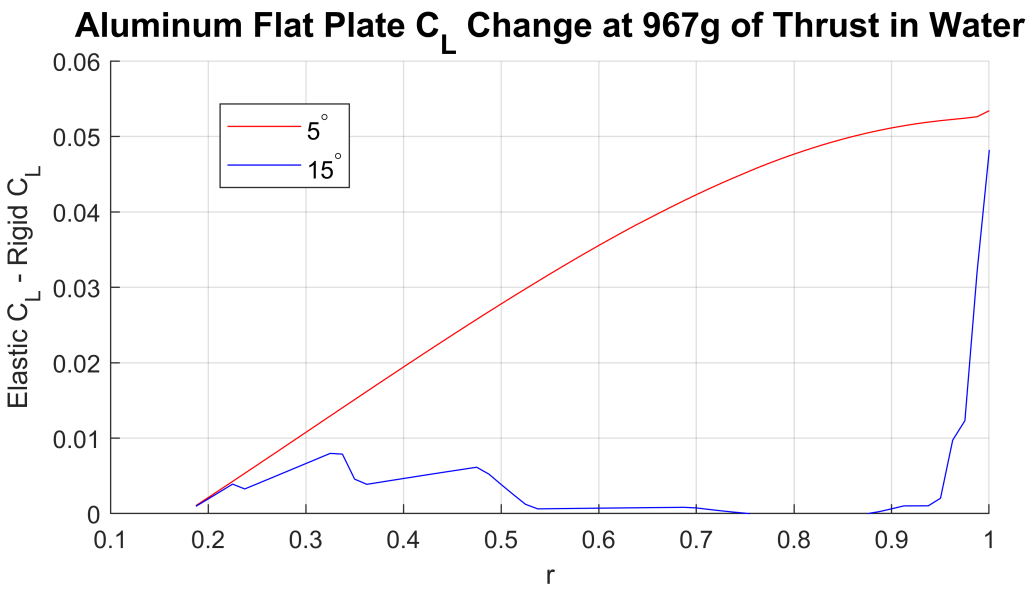

Figure 3.16: Change in C_L distribution between elastic and rigid cases of aluminum flat plate rotor in water at 5° and 15° pitch settings

Finally, it is useful to evaluate the rotor in air and water using the non-dimensional thrust C_T and power C_P. Figure 3.17 shows an increase in experimentally observed and BEMT predicted C_T and C_P between air and water for lower pitches. This is caused by elastic effects, as evidenced by a lack of C_T or C_P change in the rigid BEMT analysis results. Additionally it can be seen that at the highest pitch case the difference between air and water results is lower. The dashed line is a rigid BEMT prediction over many pitch settings that indicates stall for pitch settings above 15°.

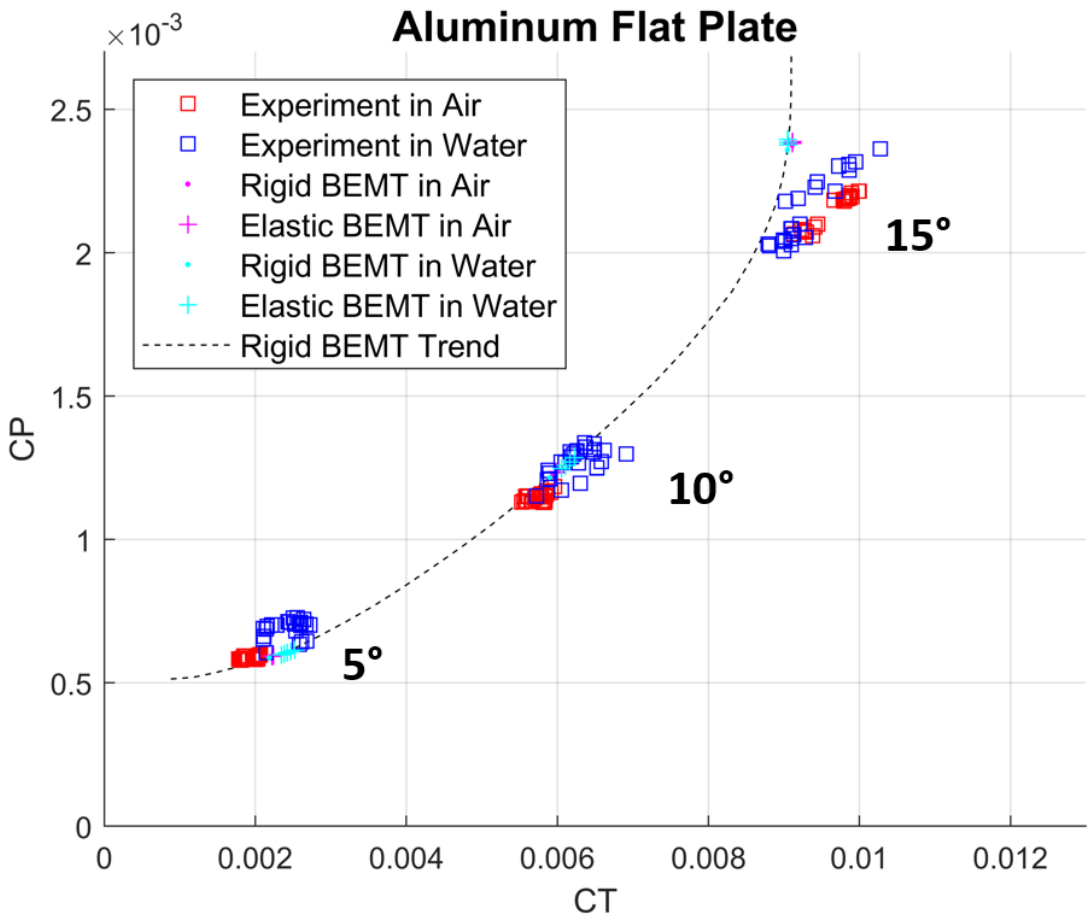

Figure 3.17: Aluminum flat plate rotor thrust and power coefficients in air and water

3.3.3 Cambered Plate Rotor

3.3.3.1 Air

The 8-ply carbon composite cambered plate rotor thrust and power versus RPM in the air can be seen in Figures 3.18 and 3.19 respectively.

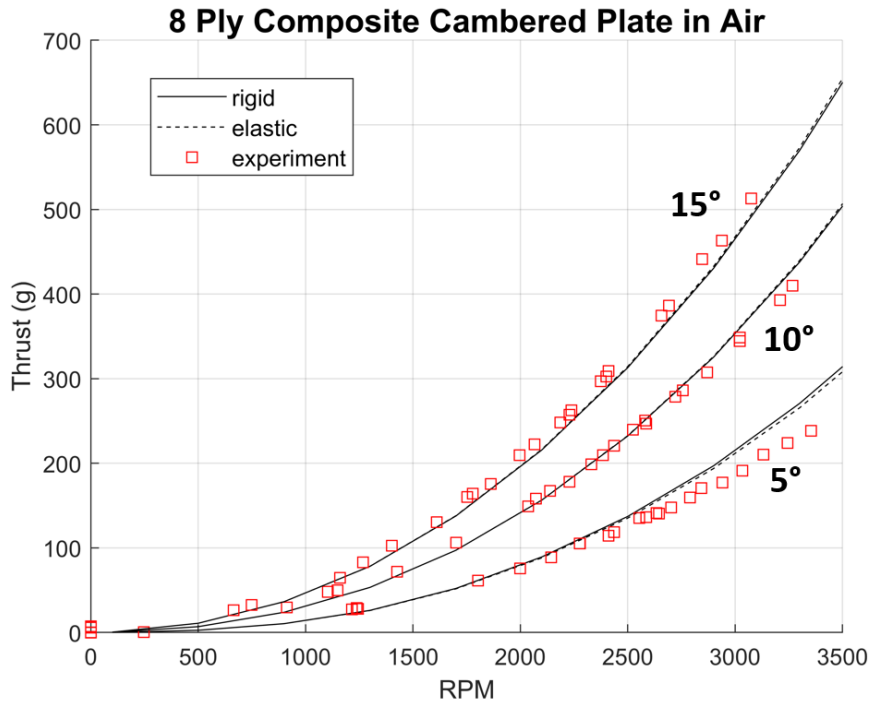

Figure 3.18: Carbon composite cambered plate rotor thrust in air

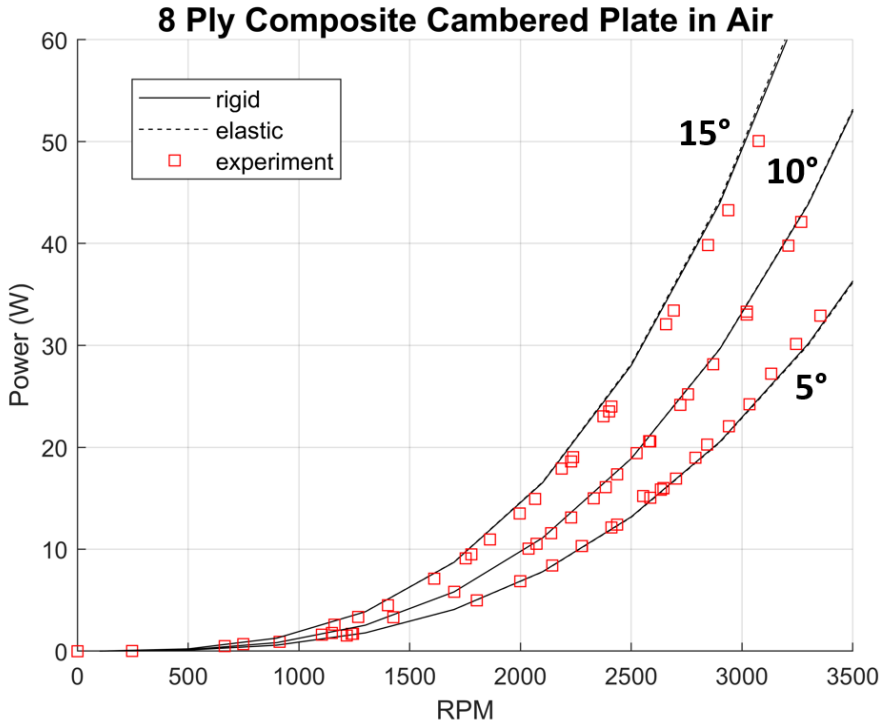

Figure 3.19: Carbon composite cambered plate rotor power in air

The BEMT prediction shows good agreement with the experimental data for thrust and power in the air. As with the flat plate airfoil case, the elastic effects in air show little impact on the prediction.

3.3.3.2 Water

The rotor thrust and power versus RPM in a fully in water condition can be seen in Figures 3.20 and 3.21 respectively.

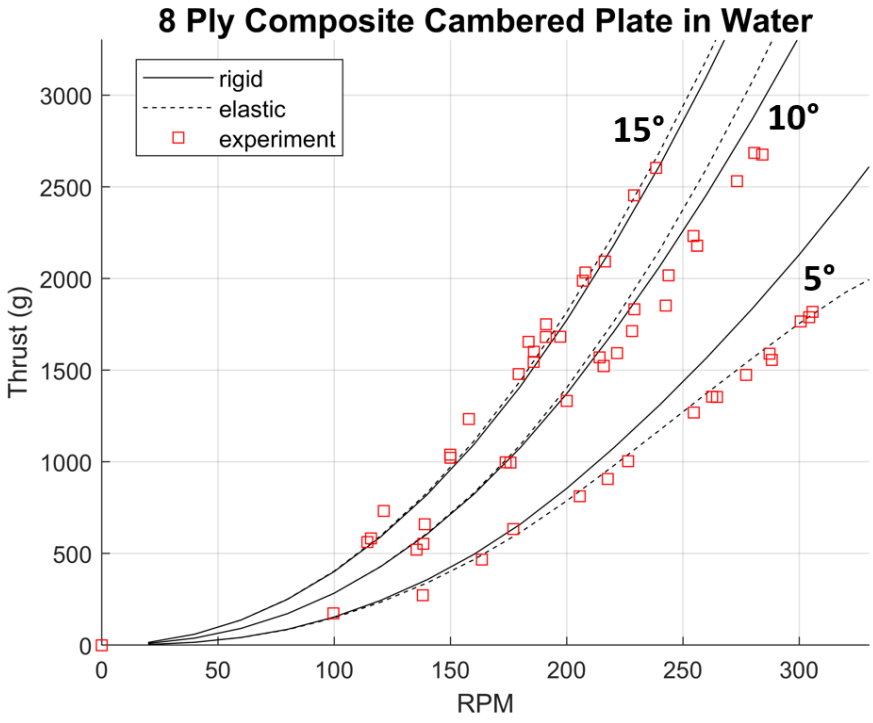

Figure 3.20: Carbon composite cambered plate rotor thrust in water

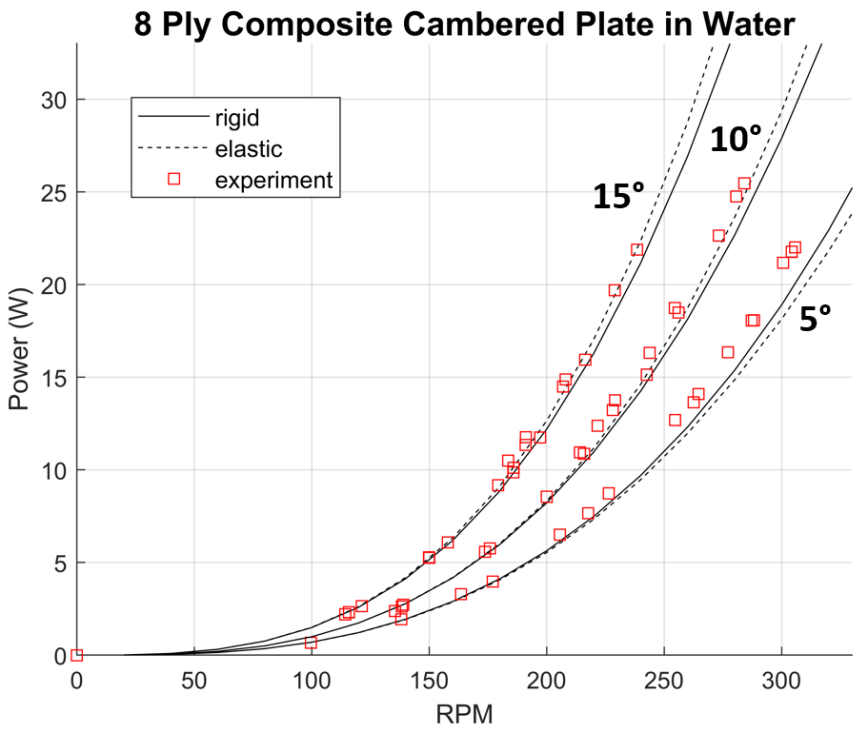

Figure 3.21: Carbon composite cambered plate rotor power in water

It can be seen that elastic effects have a greater impact in water than in air. Note the significant decrease in thrust caused by elastic effects in the 5° pitch case. This is caused by the large negative C_M of the cambered airfoil. It can be seen in the air case in Figure 3.18 that elastic effects also slightly decrease the thrust, indicating dM_{aero} is opposite in direction and greater in magnitude to dM_{lift} even in the air. In the water the high density increases the forces involved, exaggerating the difference.

Overall BEMT predictions show good agreement with experimental data for thrust and power in the water as well. This rotor blade has a lower torsional stiffness and experimental results are sensitive to small discrepancies in M_{tot}.

When the non-dimensional results for the cambered plate rotor in air and

water conditions are evaluated, the larger effect of Reynolds number can be seen. Figure 3.22 shows that the experimentally observed difference between air and water C_T and C_P is similar to the flat plate case, except the 15° pitch cambered airfoil case has the largest difference while the flat plate 15° pitch case has the smallest. Additionally the impact of Reynolds number on the airfoil is evident, as not only do the elastic BEMT results show increased C_T and C_P, but so does the rigid case. The rigid BEMT prediction over many pitch settings shown as a dashed line again indicates stall for pitch settings above 15°.

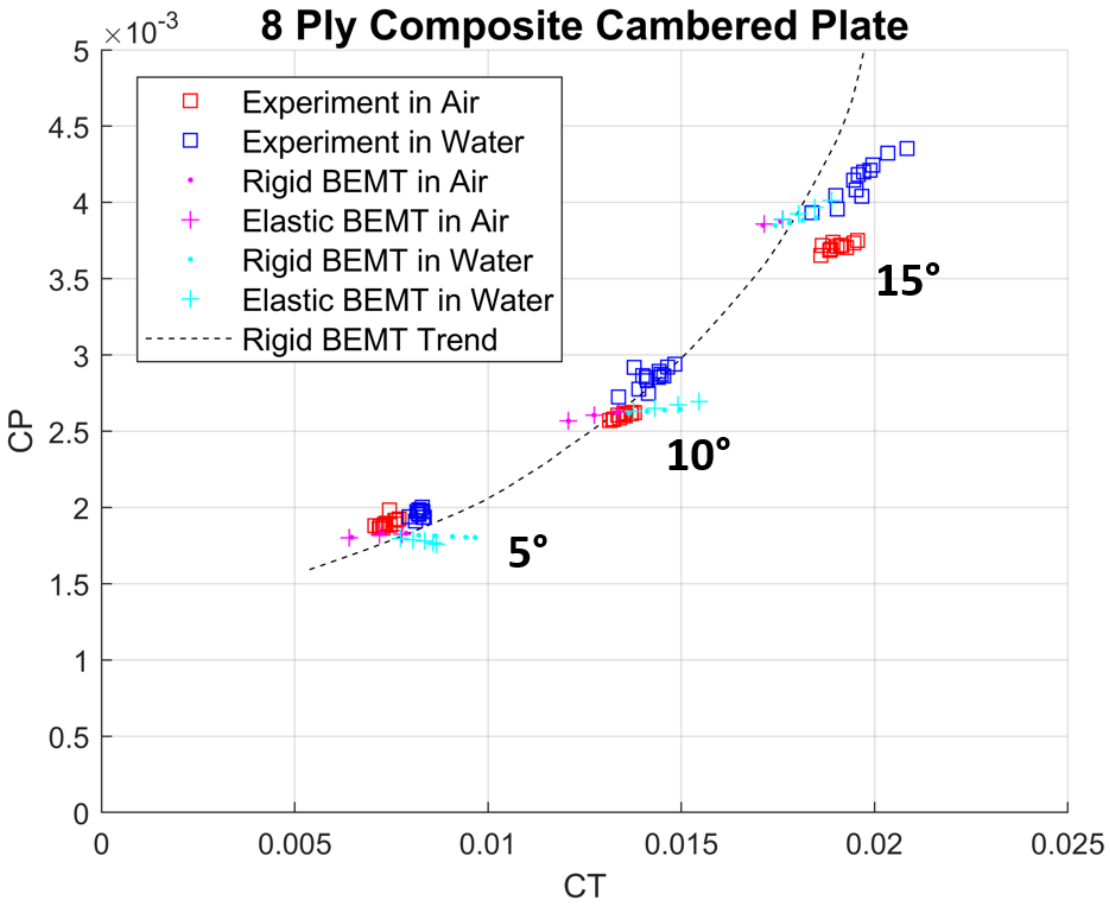

Figure 3.22: Carbon composite cambered plate rotor thrust and power coefficients in air and water

3.4 Chapter Summary

This chapter covers the formulation of BEMT used to analyze rotor performance, the use of experimental data and TURNS2D CFD software to generate airfoil tables, and the predicted rotor performance relative to experimental data.

It was found that Reynolds number effects have a large impact on cambered airfoil performance. Additionally, it was found that BEMT is able to show good agreement with experimental rotor data.

BEMT analysis reveals that elastic effects are minimal in air, but have a larger impact on rotor performance in water in both the cambered plate and flat plate airfoil cases. This is due to the larger aerodynamic moment and moment due to lift distributions along the blade. The aerodynamic forces scale with density and rotational speed squared, and the increase in density overcomes the decrease in rotation speed at the same shaft power.

Chapter 4: Rotor Transition Modeling

The experimental test stand described in Chapter 2 was used to collect rotor performance data in the transition between air and water. The rotor used is a commercial 1555 carbon fiber rotor shown in Figure 4.1 with a 22 pole sensorless motor.

Figure 4.1: Commercial rotor used for transition testing

The air-water mixture that the rotor operates in near the free surface is characterized in this paper by an effective density ρ_{eff}, defined as the density of a single medium homogeneous fluid that would produce the same rotor performance. This value is not measured, but is estimated to contextualize the mixed medium.

First the rotor performance was tested with varied throttle at constant depths near the water surface.

4.1 Constant Depth

The time averaged thrust at different constant heights of the rotor center above the water surface (negative height indicating depth, or a submerged rotor) are shown

in Figures 4.2 and 4.3. The lowest rotor surfaces first contact the water when the center is 0.8 cm above the surface, which corresponds to $\bar{h} = 0.042$.

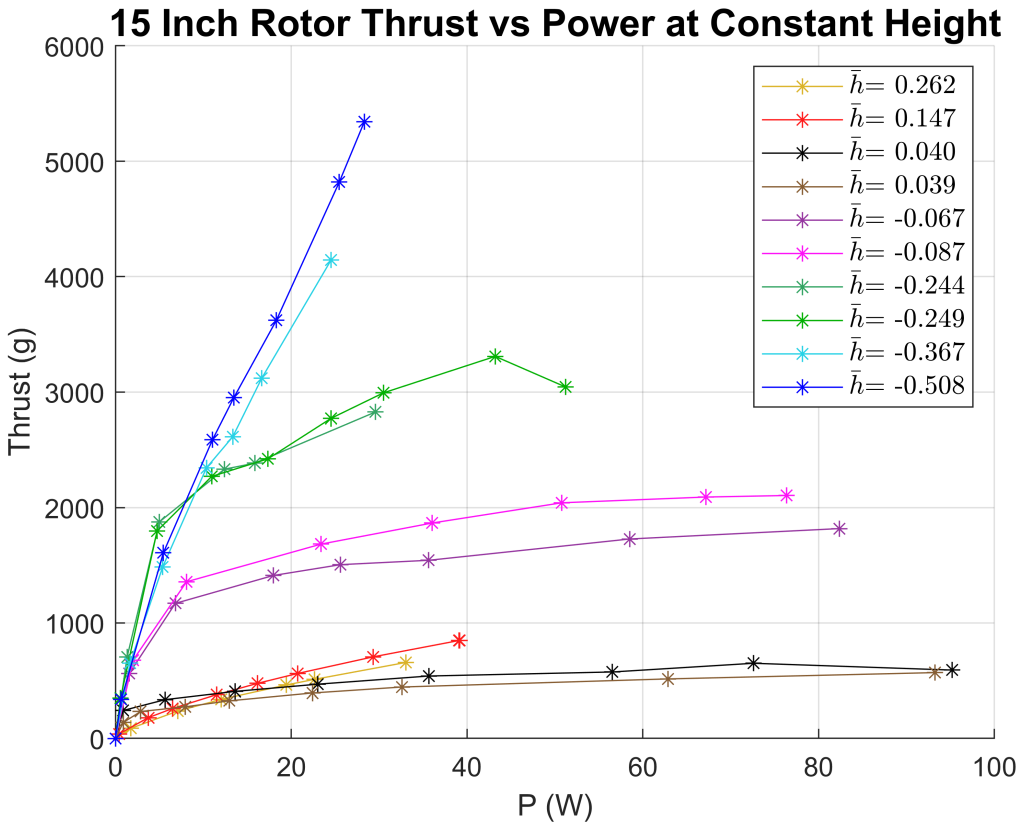

Figure 4.2: Thrust versus power of 15 inch rotor tested at constant heights

The thrust versus power at various heights is plotted in Figure 4.2. It shows that as the depth increases so does the thrust, with the exception of minimal positive height with water contact (near $\bar{h} = 0.04$). At this height the thrust range is the same, but takes more power. By inspecting the thrust plotted against RPM shown in Figure 4.3, it can be seen that the increase in power at $\bar{h} \approx 0.04$ corresponds to a decrease in RPM.

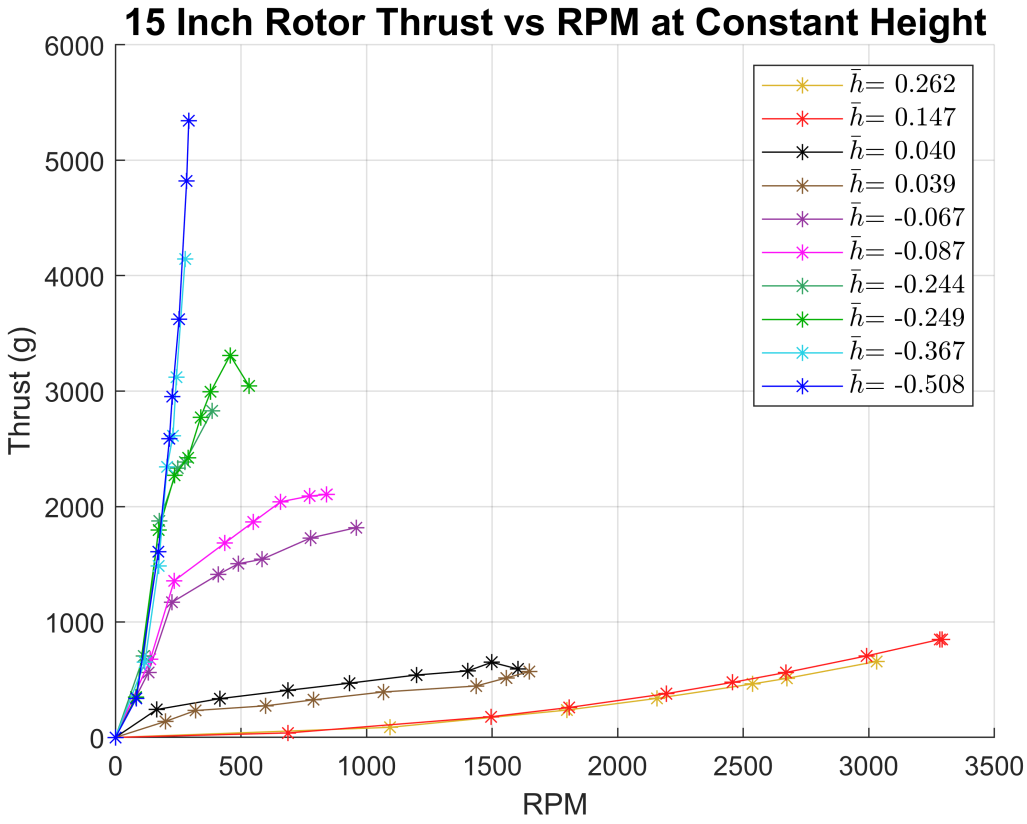

Figure 4.3: Thrust versus RPM of 15 inch rotor tested at constant heights

Figures 4.2 and 4.3 show that the rotor thrust and power curves gradually transition to the fully submerged case as the depth increases past initial contact. This indicates that the rotor water entry and water exit transitions can not be modeled as a step change in medium density at the water surface due to the mixing of the air and water. These results also indicate that at depths within $-.37 < \bar{h} < 0$ the rotor is in a transition state between fully in water and fully in air.

It was observed that at these depths, the rotor would operate in a mixed air-water medium. Throughout the rotation the rotor would splash water into the air and the void left by the displaced water would be filled by water from below and air from above. Some portion of the splashed water remains in the vicinity of the rotor

disk above the water free surface as well. As a result a highly turbulent air-water mixture forms in the neighborhood above and below the original free-surface of the water. The rotor disk intersects this volume and the resulting performance characteristics are not indicative of either fully in water or fully in air rotor performance. This thesis assumes this mixed air-water medium that the rotor operates in during the transition has a homogeneous "effective" density of ρ_{eff} where $\rho_a \leq \rho_{eff} \leq \rho_w$.

In addition to the observations of the gradual variance of rho_{eff} within $-.37 < \bar{h} < 0$, this experiment indicates that ρ_{eff} is a function of both depth and rotational speed. Previous work on the topic assumed ρ_{eff} to be a function of depth only [23]. However, it was observed during rotor tests near the water surface that as the RPM increased, the blades displaced more water and operated in a lower density air-water mixture. This can be seen in Figure 4.4, the top image shows a smaller splash at lower throttle, and the bottom image shows a larger splash at higher throttle at the same height. The water around the rotor disk in the bottom image is noticeably whiter, implying more aerated water and therefore a lower ρ_{eff}.

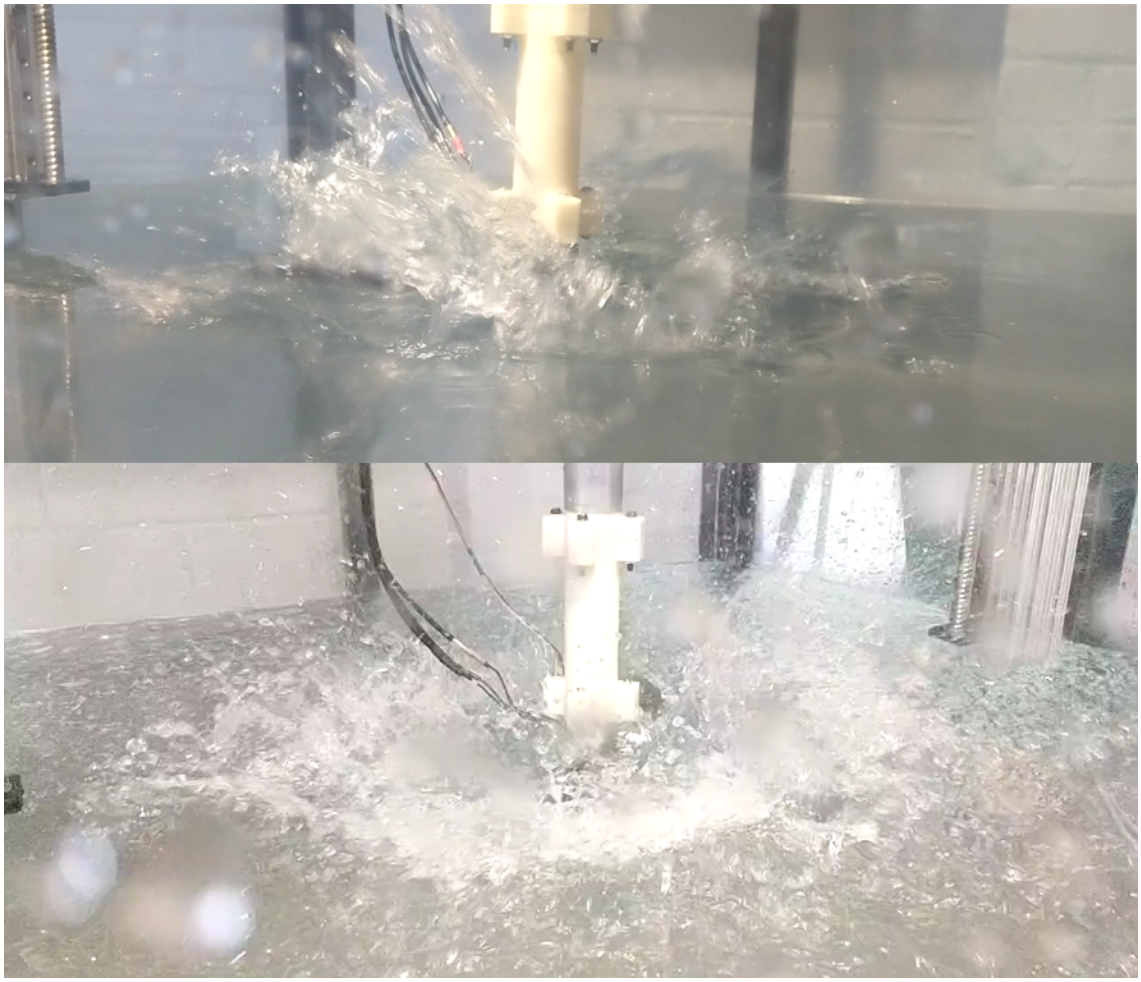

Figure 4.4: Top: Image of rotor in transition at low throttle
Bottom: Image of rotor in transition at high throttle

This dependence is confirmed by inspecting Figure 4.5. When the height is kept constant and RPM is increased a clear peak exists in thrust as the RPM increases. If ρ_{eff} were a function of depth only, the thrust would monotonically increase with RPM.

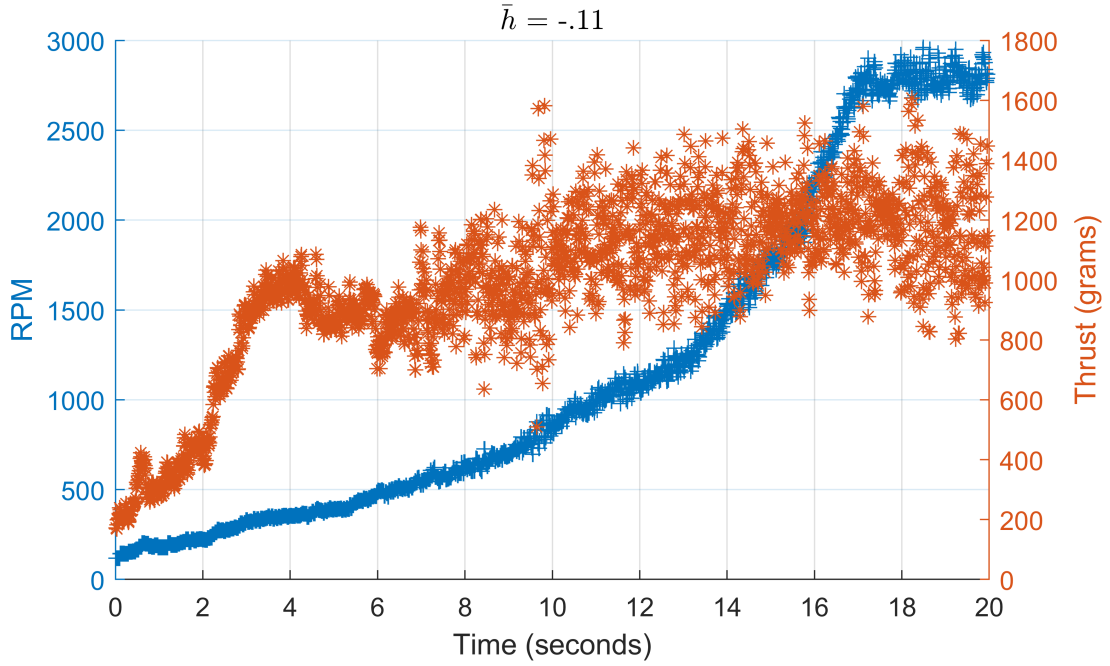

Figure 4.5: A peak in thrust exists as the RPM increases at a constant height due to more displacement of water at higher RPM

When the height is kept constant at various positions and RPM is increased, the results indicate a transition state where $\rho_a \leq \rho_{eff} \leq \rho_w$ that is a function of the depth as well as the RPM. Next, experiments with varying height were conducted.

4.2 Entrance and Exit from Water

Experiments were conducted with varying height and a fixed throttle. The rotor is set to thrust up, and the carriage is lowered and raised into and out of the water. The carriage movement is tested at 3 constant speeds: 2.4 cm/s 5.1 cm/s and 7.3 cm/s. These speeds are termed slow, medium, and fast respectively. By maintaining a constant throttle input, the variation of rotor parameters at a given input setting is found, which is informative in designing a controller for throttle

control.

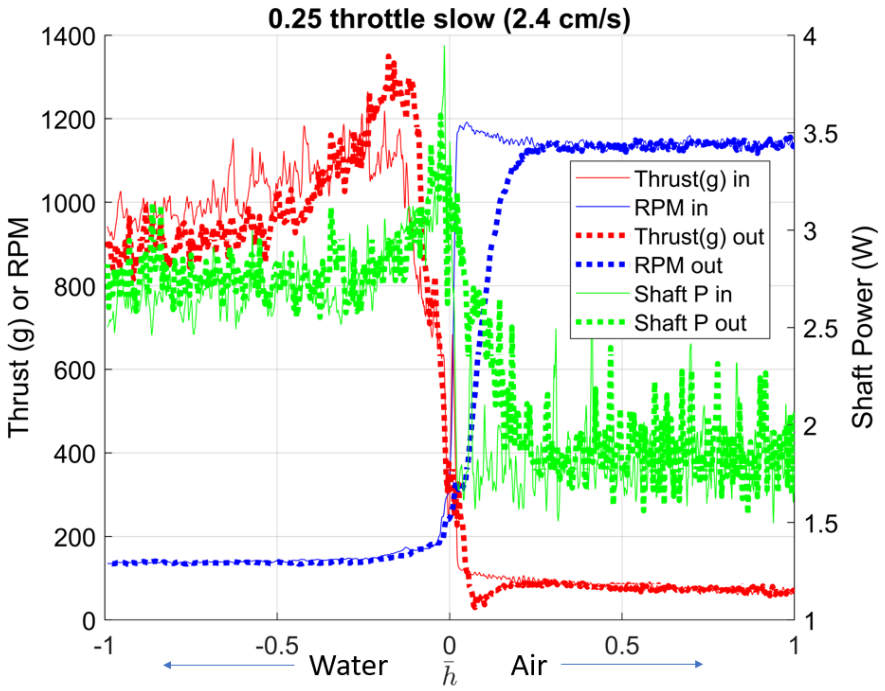

Figure 4.6: 25 % throttle transition at slow vertical speed

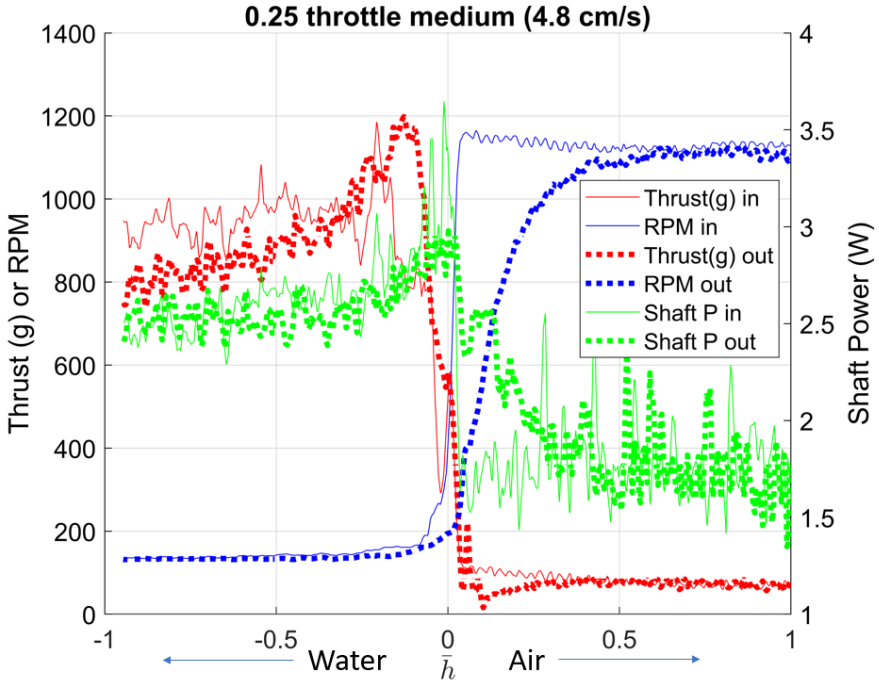

Figure 4.7: 25 % throttle transition at medium vertical speed

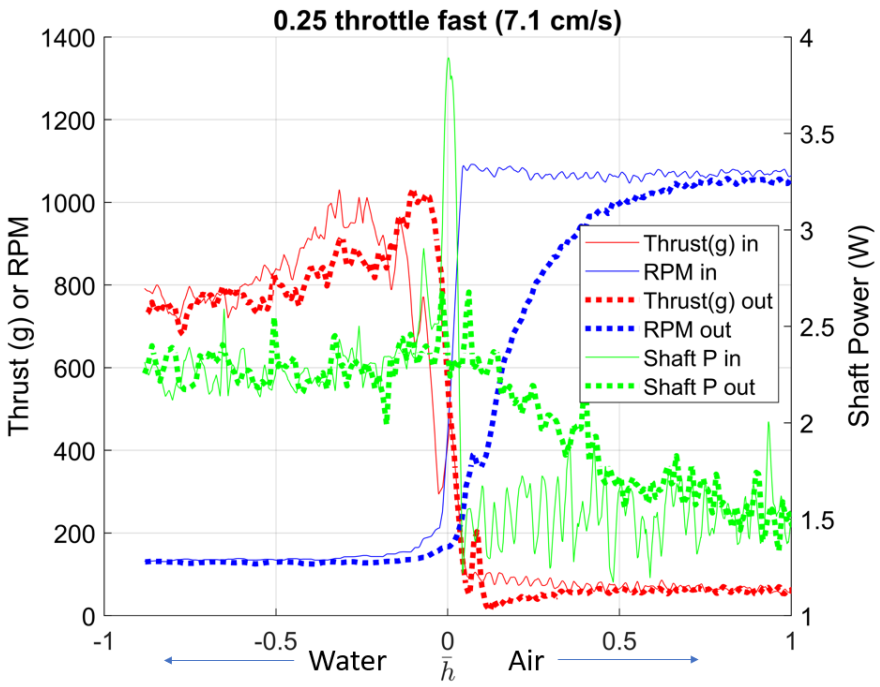

Figure 4.8: 25 % throttle transition at fast vertical speed

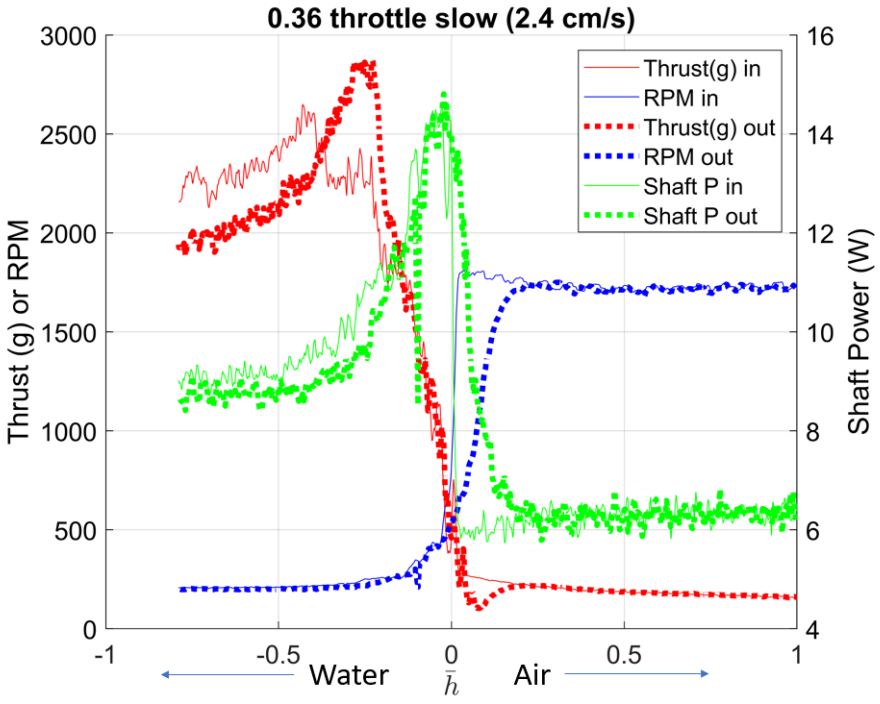

Figure 4.9: 36 % throttle transition at slow vertical speed

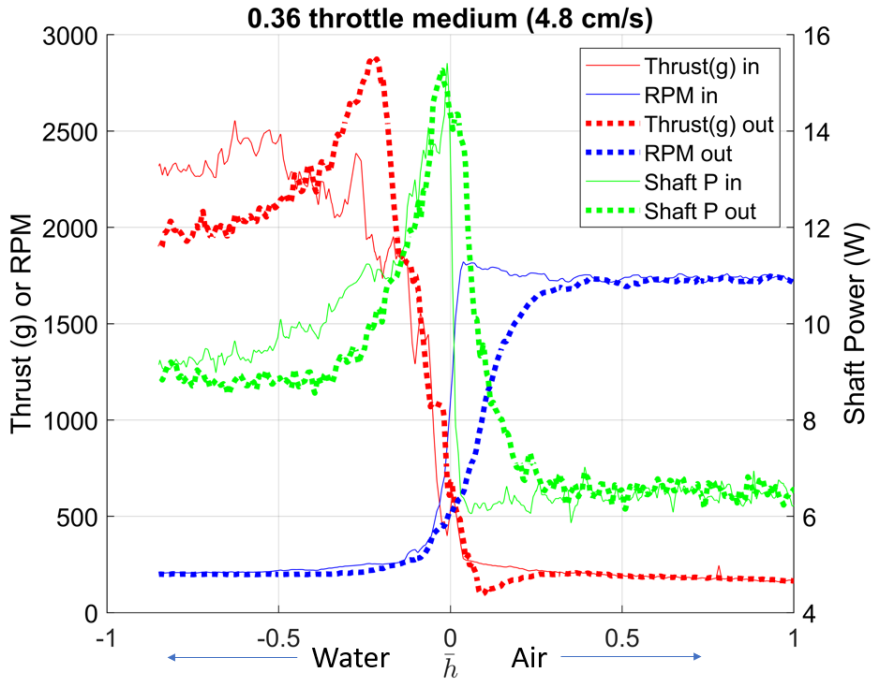

Figure 4.10: 36 % throttle transition at medium vertical speed

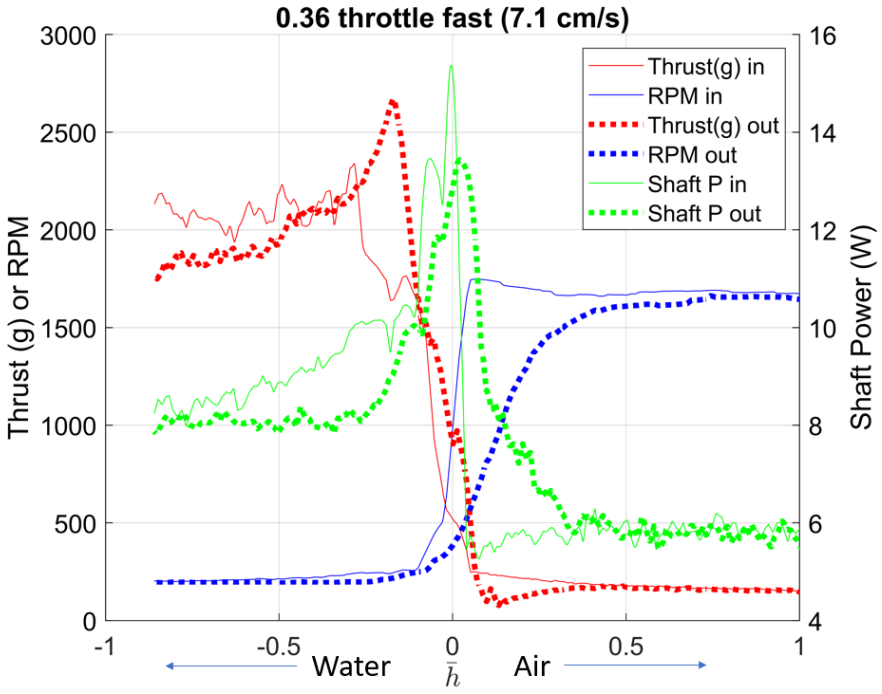

Figure 4.11: 36 % throttle transition at fast vertical speed

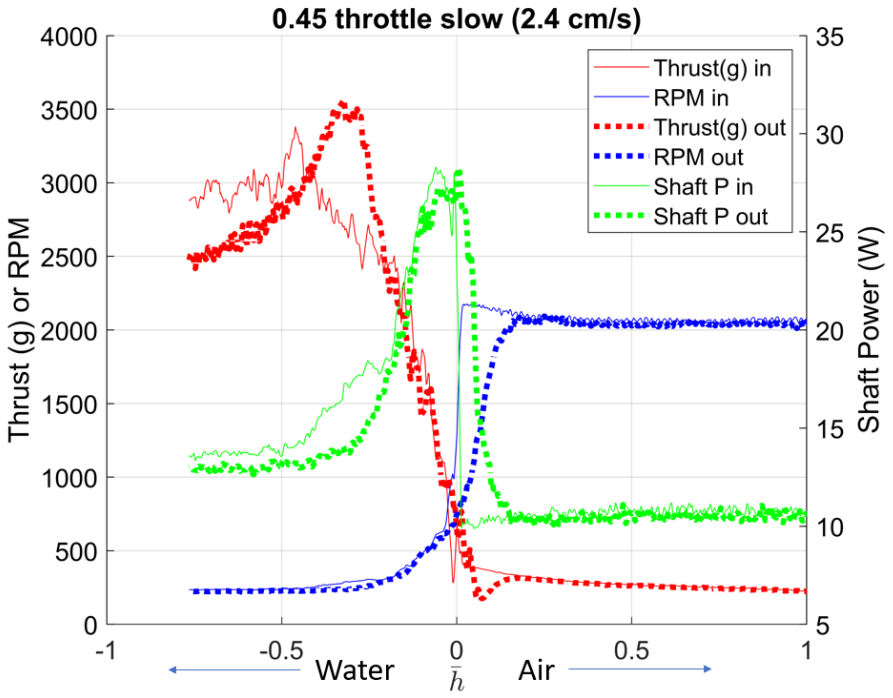

Figure 4.12: 45 % throttle transition at slow vertical speed

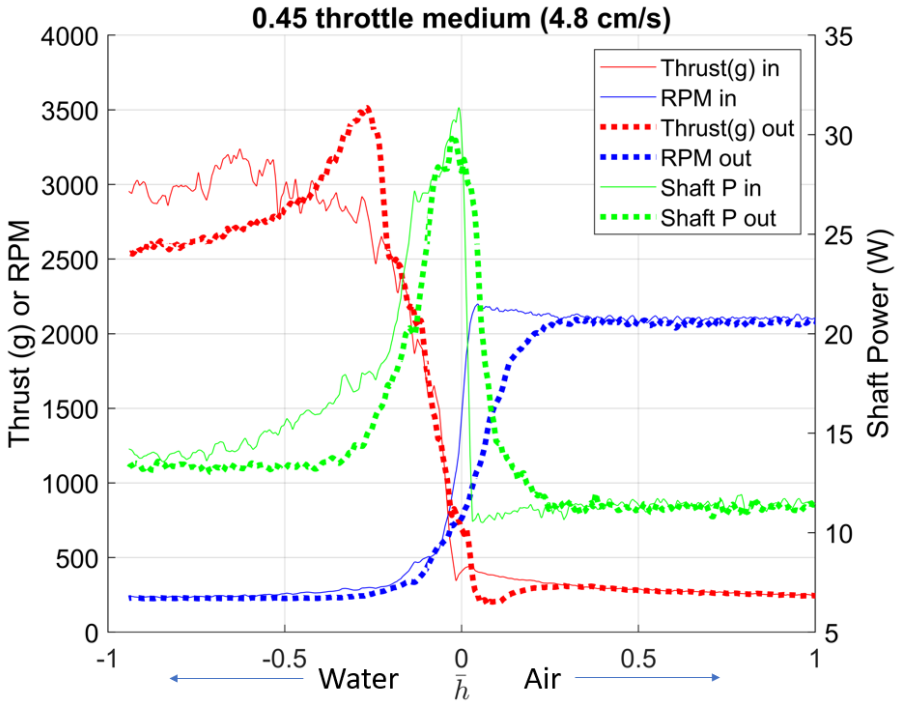

Figure 4.13: 45 % throttle transition at medium vertical speed

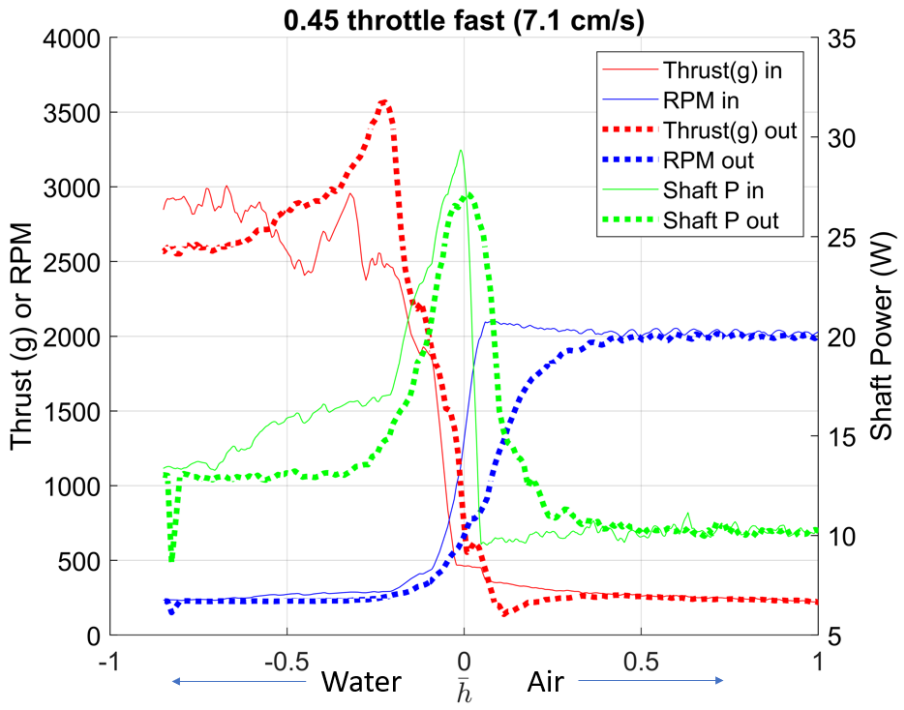

Figure 4.14: 45 % throttle transition at fast vertical speed

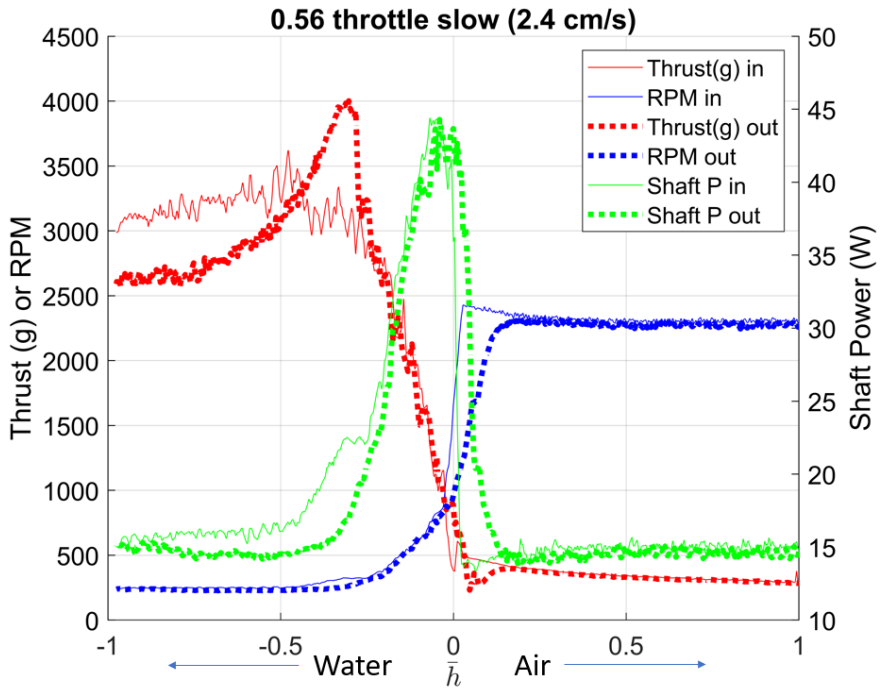

Figure 4.15: 56 % throttle transition at slow vertical speed

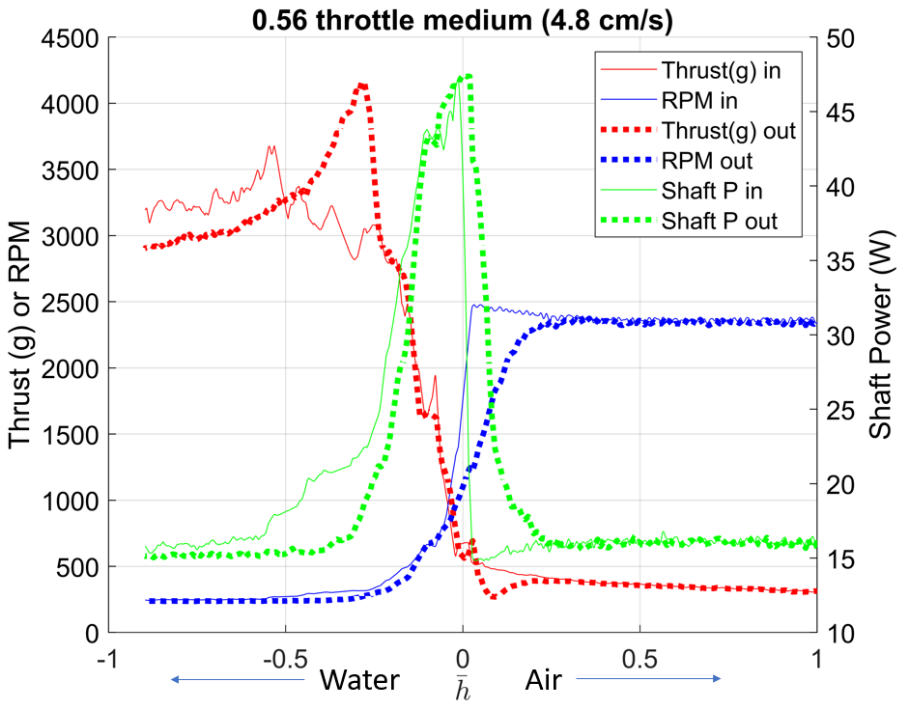

Figure 4.16: 56 % throttle transition at medium vertical speed

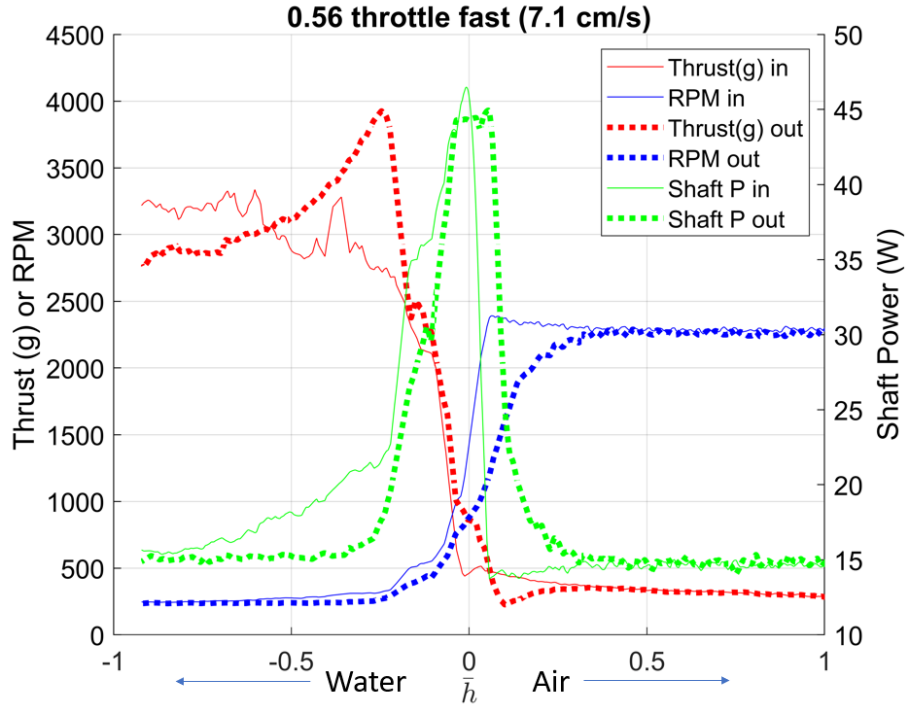

Figure 4.17: 56 % throttle transition at fast vertical speed

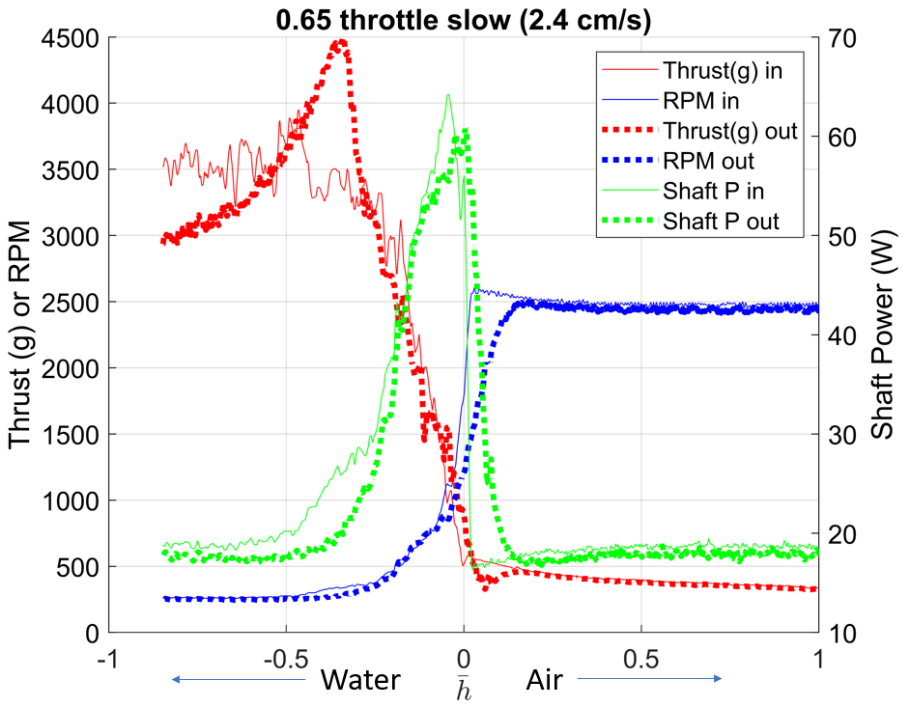

Figure 4.18: 65 % throttle transition at slow vertical speed

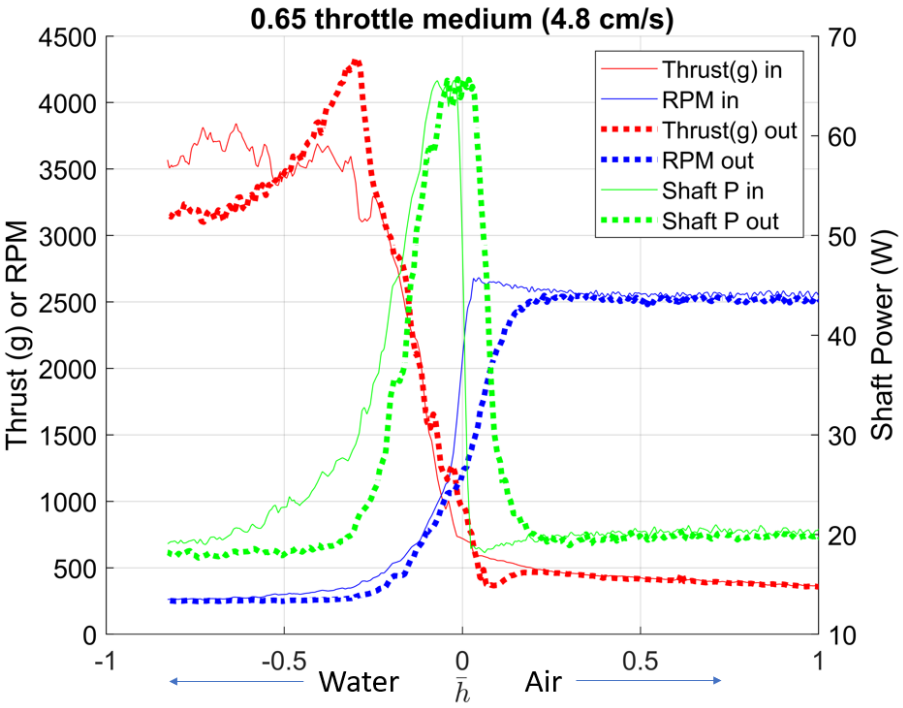

Figure 4.19: 65 % throttle transition at medium vertical speed

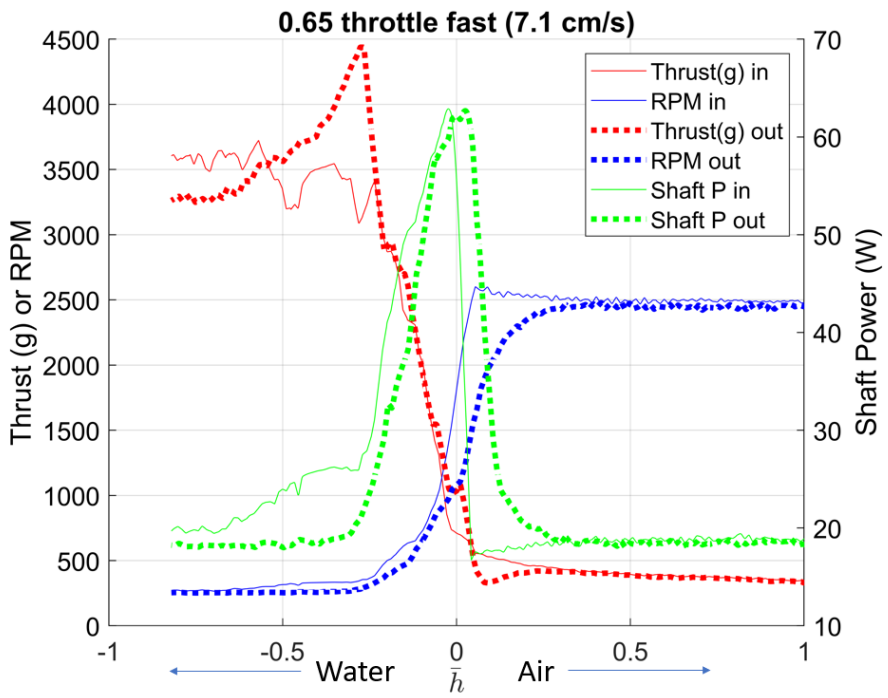

Figure 4.20: 65 % throttle transition at fast vertical speed

Constant throttle transitions reveal several characteristic effects of a flat rotor air-water transition and differences between water entry and exit transitions.

4.2.1 Effect of vertical speed

First, it can be seen that there is minimal difference in rotor performance during the transition into or out of the water between the tested vertical speeds. Comparing the results of the three speeds at any throttle, it is evident that the peak amplitudes of the thrust and power coming into and out of the water are at approximately the same level. The level of scatter in the data seems to decrease with increasing speed, but this can be attributed to fact that the data sample rate is a constant attribute of the experimental setup. As a result the number of data points

per cm of vertical travel decreases with increasing vertical speed, adding apparent smoothness to the curves.

The shape of the RPM, thrust, and power curves also change negligibly with varying vertical speed during the transition. There is a noticeable difference in the height above the water at which the RPM and power of the rotor during water exit reach match the RPM and power of the rotor during water entry. For instance, in the slow speed case shown in Figure 4.6 the RPM and power of the water exit curve match the RPM and power of the water entry curve at roughly $\bar{h} = 0.262$. However, in the medium speed case and fast speed case shown in Figures 4.7 and 4.8 that height is roughly $\bar{h} = 0.577$ and $\bar{h} = 0.787$ respectively. This change is attributed to the time it takes for the ESC to accelerate the rotor rotation to nominal fully in air RPM, which in all throttle cases is roughly constant with varying vertical speed.

Despite that the vertical speed has minimal effects on rotor performance in transition, some change can be seen in the magnitude of the power and thrust at the deepest conditions, were the rotor is operating fully in water. This is attributed to the influence of the rotor climb and descent velocities, and their magnitude relative to the inflow velocity.

4.2.2 Underwater Ceiling effect

It may seem intuitive that the maximum thrust generated by a rotor at a constant throttle moving into or out of the water would occur during water entry as the rotor initially strikes the water before losing rotational speed. However, the

experimental results indicate the contrary, the maximum thrust occurs during water exit, just below free surface. This peak in thrust on water exit can be seen in all Figures 4.6 - 4.20 and occurs near $\bar{h} = -0.262$. This is attributed to the underwater ceiling effect.

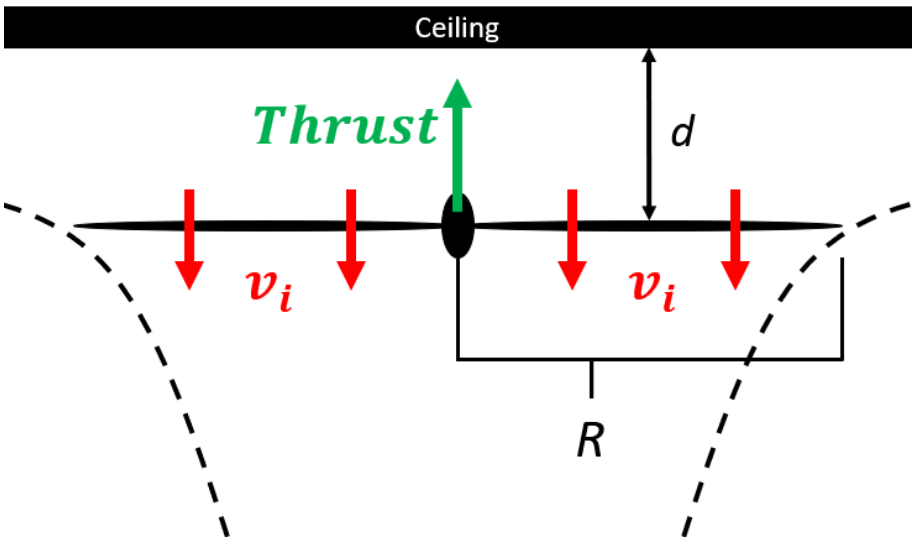

Figure 4.21: Ceiling effect diagram

When a horizontal surface restricts the airflow above the rotor as shown in Figure 4.21, the power required to generate a given thrust is reduced [24]. The surface acts as a cushion, increasing the lift produced for the same power. The effect is analogous to the ground effect, except the surface location is above the rotor, and is commonly observed during indoor flight of a rotorcraft near the ceiling, hence the name.

In the case of water exit, the "ceiling" is the water surface. As the rotor operates in water, before the beginning of the transition to a fully in air state, the streamlines of the flow near the rotor do not cross the water free surface. As result, the flow pattern of water around a rotor just underneath the free surface is akin to

the flow of air around a rotor underneath a ceiling. This effect breaks down as soon as the transition begins because the ingestion of air removes the constraint imposed by the "ceiling" and flow streamlines intersect the free surface.

This effect can be is characterized by the momentum theory derived Equation 4.1 found by Hsiao and Chirattanonon [24] where γ is defined by Equation 4.2 and d is the vertical distance from the rotor to the ceiling.

$$P = \frac{1}{\gamma}\kappa T\sqrt{\frac{T}{2\rho A}} + P_0 \tag{4.1}$$

$$\gamma = \frac{1}{2}(1 + \sqrt{1 + \frac{1}{8}(\frac{R}{d})^2} \tag{4.2}$$

It can be seen that the ceiling effect influences the induced power only. The ratio of induced to profile power in air is not significantly different to that in water. As a result the profile power can be ignored for simplicity, which allows for a concise expression for relative increase in thrust due to proximity to the ceiling, shown in Equation 4.3, where $T_{ceiling}$ is the thrust near the ceiling.

$$\frac{T_{ceiling}}{T} = \gamma^{2/3} \tag{4.3}$$

By plotting the relative increase in thrust against the distance from the water free surface it is evident that at low throttle and low speeds the ceiling effect formulation agrees with the experimental data. This can be seen in Figure 4.22.

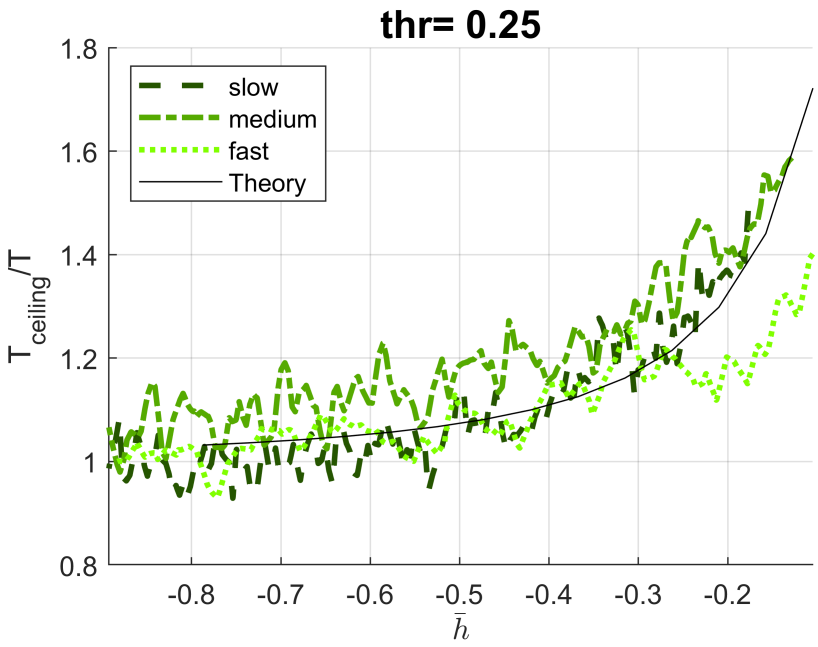

Figure 4.22: Ceiling effect under low throttle, negative $\bar{h}$ indicates depth

However as the throttle increases Equation 4.3 underpredicts the thrust response as seen in Figure 4.23. Additionally the increasing climb speed of the rotor decreases the thrust response. This is caused by the breaking of an assumption of the ceiling effect derivation. In [24] it is assumed that the ceiling is rigid. However, under high throttle, it is apparent that the low pressure zone above the rotor deforms the free surface of the water and lowers the distance between the rotor and the boundary. This can be seen in the stills from a water exit test at high throttle shown in Figure 4.24. The impact of climb speed is evident under slow motion video review, where it can be seen that a faster climb speed does not allow enough time for the surface deformation to be maximized, and therefore the distance to the free surface is larger than in a slower climb velocity case at the same depth. Lastly, it should be noted that the ceiling effect formulation assumes the ceiling to be flat,

but the video evidence shows the rotor creating an torus shaped depression in the free surface.

For these reasons, the simplified formulation in Equation 4.3 breaks down at high thrust cases. Despite this, by taking into account the water surface displacement seen in video, the ceiling effect provides a reasonable prediction of the thrust based on the physical distance between the rotor and the water surface.

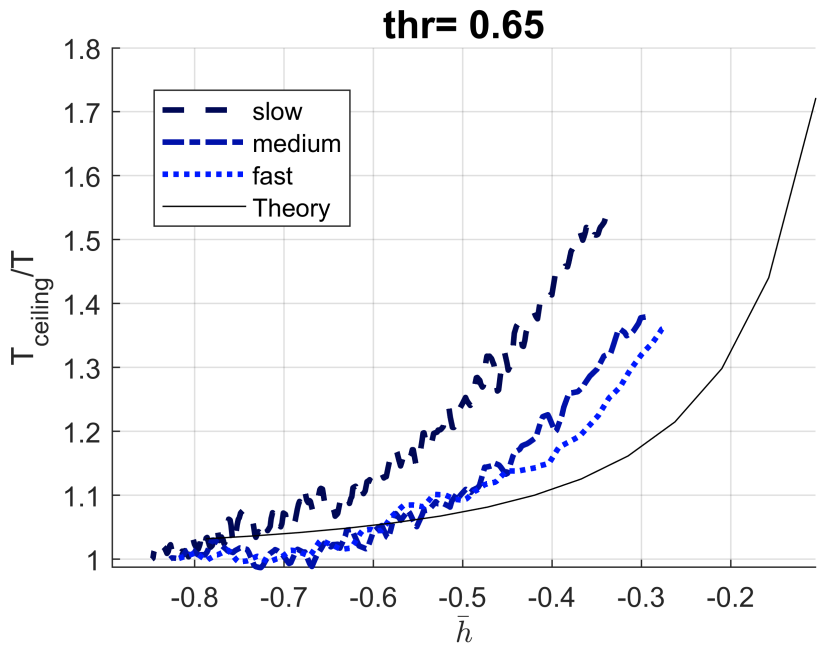

Figure 4.23: Ceiling effect under high throttle, negative $\bar{h}$ indicates depth

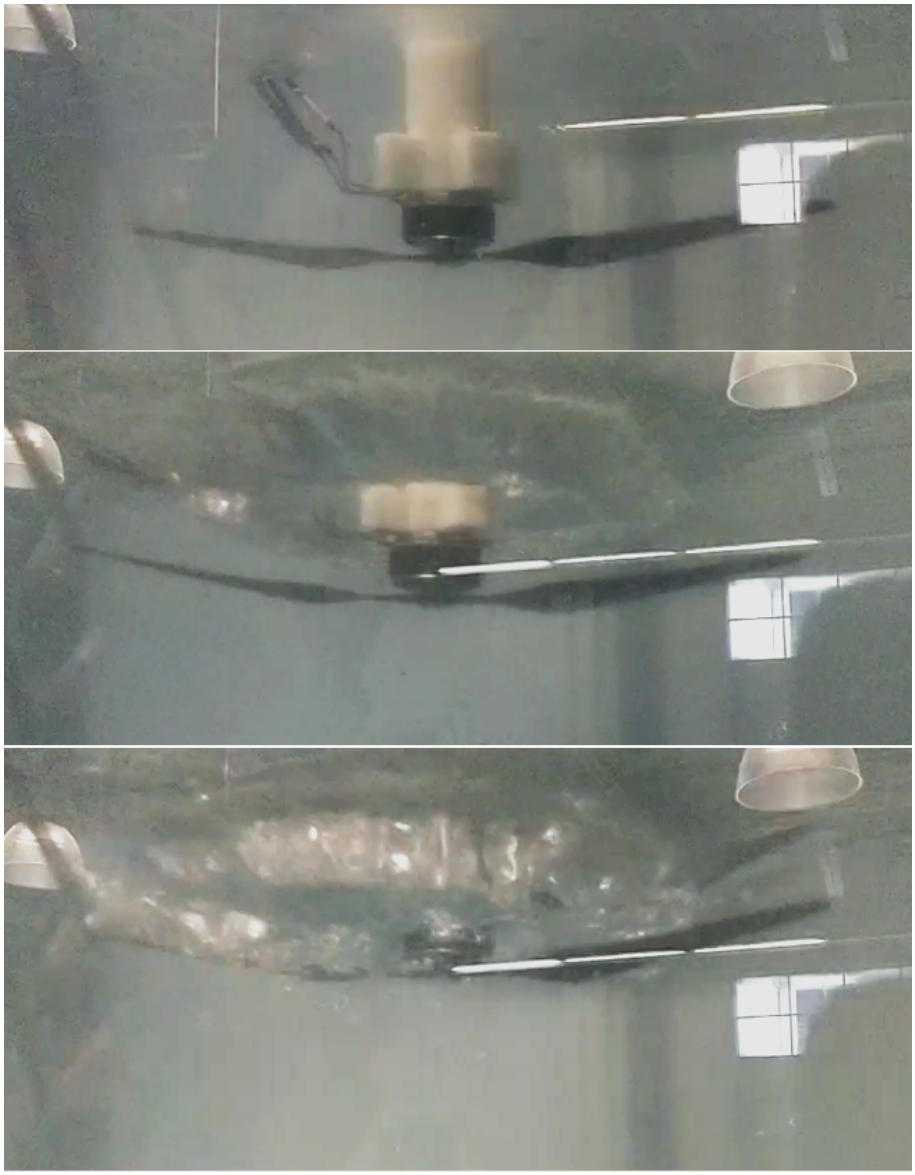

Figure 4.24: Stills from water exit test showing free surface deformation

4.2.3 Exiting the Water

The characteristics of the water exit are not akin to the water entry. Two observations are made that result in these differences; first, during the water exit the rotor tends to splash some water upwards and encounters it at a height above the water free surface at which no water is encountered during water entry. This

can be best observed in Figure 4.17, the thrust curve on the way out of the water is higher than the curve on the way in around the free surface at $\bar{h} = 0$. The RPM are also lower at that height, indicating that the rotor during water exit is not operating in a fully in air state at heights where the rotor during water entry is.

The second observation is that due to the time necessary for the rotational speed of the motor to accelerate back to a nominal air level, there is a transient state where the rotor operates in air with a lower RPM than nominal. This can be seen in the same Figure 4.17 as the region where the thrust on the way out is lower than on the way at a height above the water around $\bar{h} = 0.131$. This effect can be a challenge during water exit of a HAW vehicle due to the loss of thrust.

4.3 Transition Index

During the variable height rotor transition the only variable that can be kept constant is the motor throttle thr. Furthermore the throttle is the only variable with a consistent range in air and water and is also the only input to the motor used to control the thrust. As a result, a method to estimate the ρ_{eff} of the medium that the rotor operates in at any given time based on thr is desired. Additionally, in flight, it is assumed that the thrust and torque of the motor are not measured. A practically useful estimation can therefore only be a function of parameters readily available in flight, such as thr and the motor RPM.

The Transition Index TI is introduced: a variable that is 0 for a fully in air state and 1 for fully in water. It is a function of the expected motor RPM in fully in

air and fully in water conditions (RPM_a and RPM_w respectively), and the current motor RPM. RPM_a and RPM_w are found with respect to the throttle sent to the motor. The definition of TI is shown in Equation 4.4. This equation is a novel formulation for estimating the medium state during rotor transition, and is a key contribution of this thesis.

$$TI = 1 - sign(RPM - RPM_w)\sqrt{\frac{|RPM - RPM_w|}{RPM_a - RPM_w}} \tag{4.4}$$

The logic behind the definition of TI is evident by inspecting Figure 4.25. As the depth increases and the rotor operates in a medium with an increasing ρ_{eff}, the RPM curve tends toward the RPM curve in a fully submerged condition. By comparing the current RPM at any given point to RPM_a and RPM_w, which are shown as dashed thick lines in the graph, the relative difference between the current condition and fully in air or fully in water conditions can be found.

Additionally, it can be seen that the RPM curve of the transition does not linearly approach the RPM_w curve with depth. The change in the transient RPM curve is large between $\bar{h} = 0.147$ and $\bar{h} = 0.039$, but between $\bar{h} = -.087$ and $\bar{h} = -.244$ the change is smaller despite a larger change in height. This nonlinearity prompts the square root term in Equation 4.4. Lastly, due to unsteady conditions during throttle modulation, the term $RPM - RPM_w$ may be negative. This prompts the absolute value and $sign(RPM - RPM_w)$ terms to prevent errors during TI calculation in unsteady throttle conditions, an important consideration for the development of a controller based on TI.

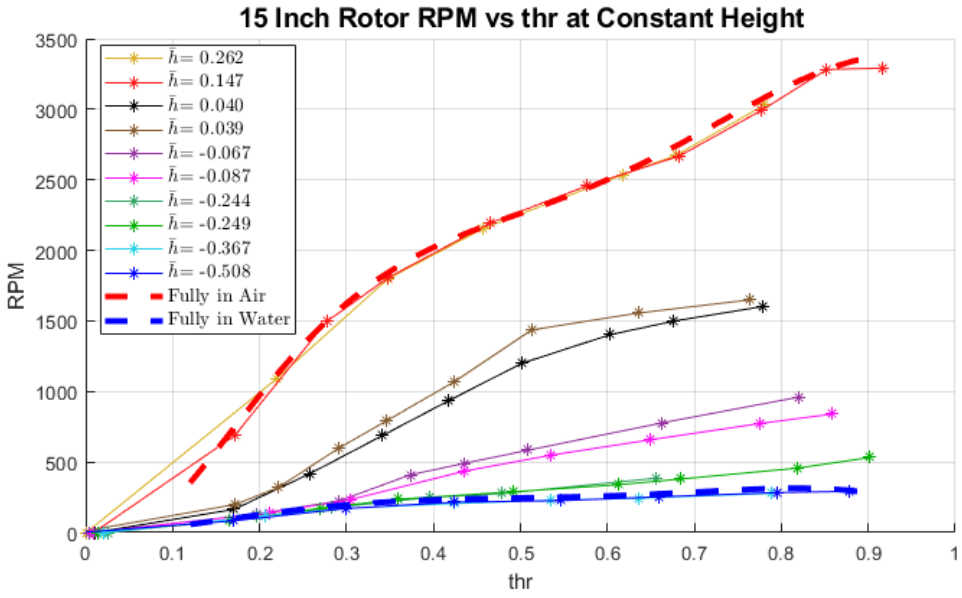

Figure 4.25: RPM versus throttle at various heights between fully in air and fully in water results

The validity of this formulation can be seen by comparing the depth during the vertical transitions described in Section 4.2 to the Transition Index, shown in Figure 4.26. When the rotor first contacts the water on the way in TI becomes non-zero, and only when the rotor enters a fully submerged state does TI become near 1. Likewise, TI approaches 0 as the rotor exits the water and demonstrates the carrying of water on exit past the nominal free surface height discussed above in Section 4.2.3. Additionally, the specific throttle setting has little effect on the TI, indicating it is valid for all throttles. However, some inaccuracies of the TI formulation are also apparent, for instance the transient state where rotor speed is accelerating is interpreted as a TI of about 0.1 Additionally the effect of climb or descent velocity are not accounted for, and result in a $TI > 1$ for a climb state in the water. Despite these minor issues, the Transition Index is a novel metric with a

simple formulation to estimate rotor state, the like of which has not been attempted prior. Furthermore, it has useful applications for the evaluation of data as well as to inform a controller.

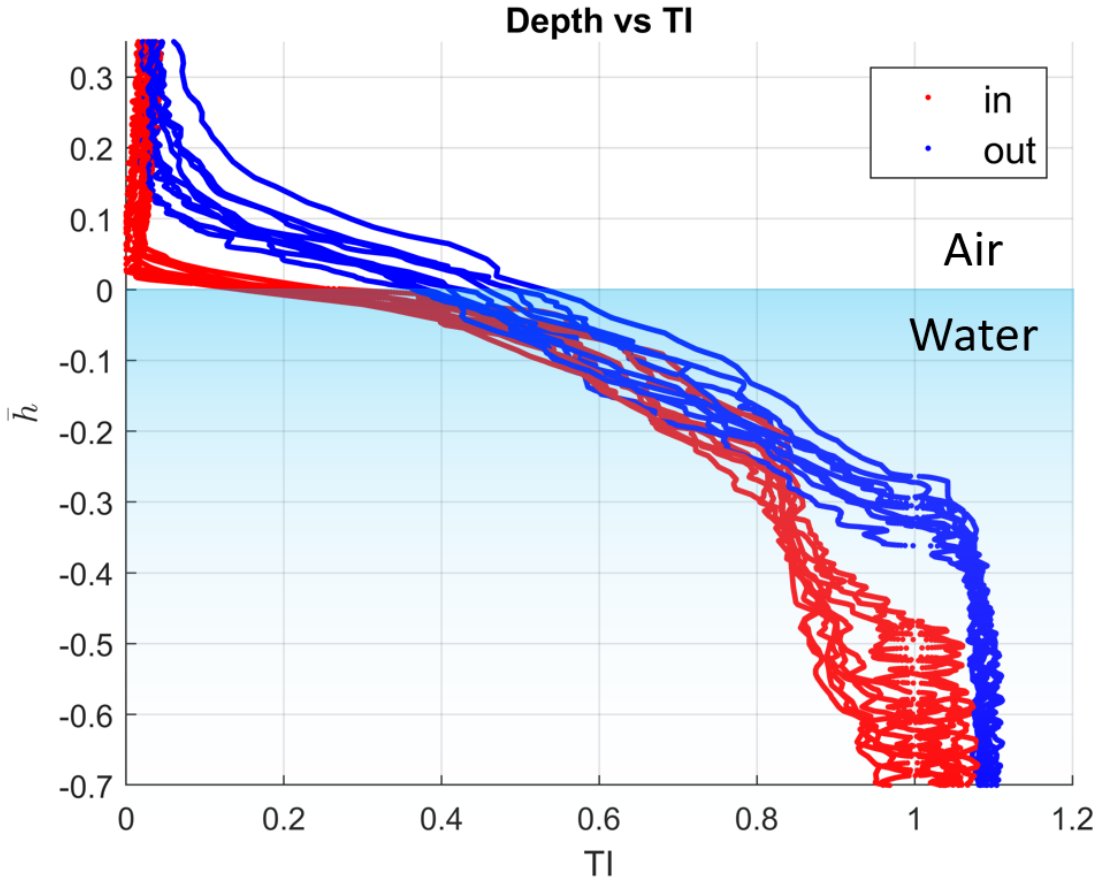

Figure 4.26: The variance of the Transition Index as the rotor enters or exits the water at various throttles

Figure 4.26 validates the formulation of TI and provides insight on the transition dynamics. It can be seen that TI varies significantly only in a limited height range regardless of the vertical speed, direction, or throttle setting of the motor. This range is $0.04 < \bar{h} < -.33$, which is consistent with the findings of experiments at constant heights described in Section 4.1.

Additionally, this formulation shows a region of transition that occurs only

on the way into the water at depths lower than 1/3 radius. In this height range the water entry tests show that TI continues to vary between 0.85 and 1, while the water exit tests stay constant. This is attributed to the aeration of deeper water caused by water entry. It was observed that during water entry there are visible bubbles at those depths that do not exist during water exit. This can most easily be seen in motion as shown in Figure 4.27.

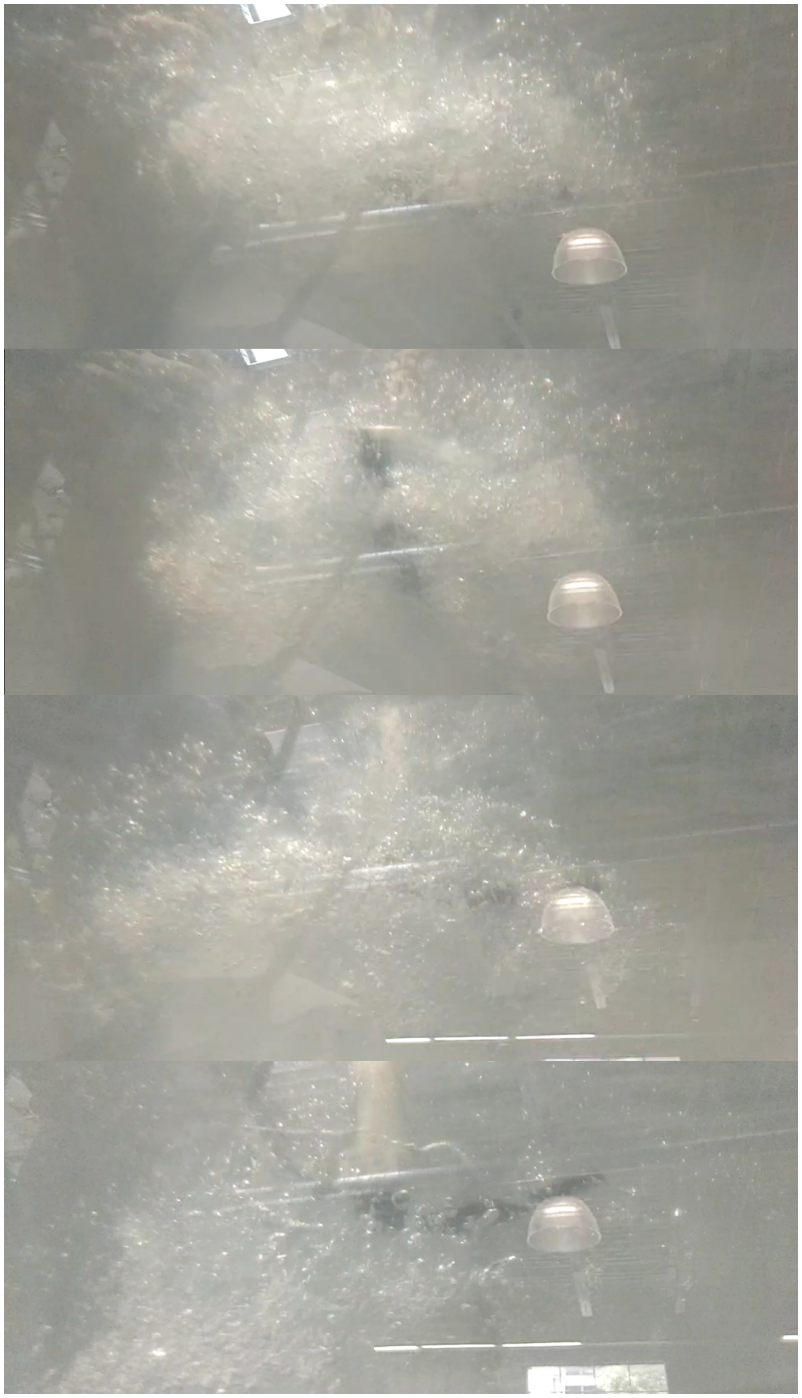

Figure 4.27: Successive video stills showing the motion and dispersion of an aerated region of water during entry.

4.4 Thrust Prediction

One of the main motivations for developing the Transition Index is to inform the flight controller. This is best achieved by predicting the thrust of the rotor as a function of TI and other variables available in flight. This formulation is structured similarly to the TI where the resulting thrust prediction is the fully in water curve at $TI = 1$ and fully in air curve at $TI = 0$. For $0 < TI < 1$ the result is an interpolation between the two curves.

To define the fully in air (T_a) and fully in water (T_w) thrust values the known non-dimensional thrust coefficients in air and water (C_{Ta} and C_{Tw} respectively) of the rotor are used. This can be found via BEMT or simple experimental testing, removing the need for the involved experimental testing performed in this thesis with the setup described in Chapter 2. The definitions of T_a and T_w are shown as Equations 4.5 and 4.6 respectively, where the $\pi/30$ term converts RPM to radians per second.

$$T_a = C_{Ta}\rho_a A(RPM_a \frac{\pi}{30} R)^2 \tag{4.5}$$

$$T_w = C_{Tw}\rho_w A(RPM_w \frac{\pi}{30} R)^2 \tag{4.6}$$

The formulation for the predicted thrust is then:

$$T_{pred} = (T_w - T_a)(1 - |1 - TI|^2) + T_a \tag{4.7}$$

Equation 4.7 scales the predicted thrust between T_a and T_w with the square of TI. The addition of the absolute value prevents the predicted thrust from surpassing T_w. This provides robustness to the equation from transient states with respect to throttle. For instance, TI may be greater than 1 if the rotor is fully in water, and the throttle is increased rapidly: while the rotor speed accelerates to RPM_w the rotor RPM will be less than RPM_w, resulting in a $TI > 1$. This does not imply that the rotor is in some state denser than water, and should not result in $T_{pred} > T_w$. The absolute value makes the predicted thrust lower in this event, which is appropriate.

T_{pred} is validated against experimentally recorded thrust to ensure adequate prediction. It should be noted that this formulation does not address the underwater ceiling or ground effects directly.

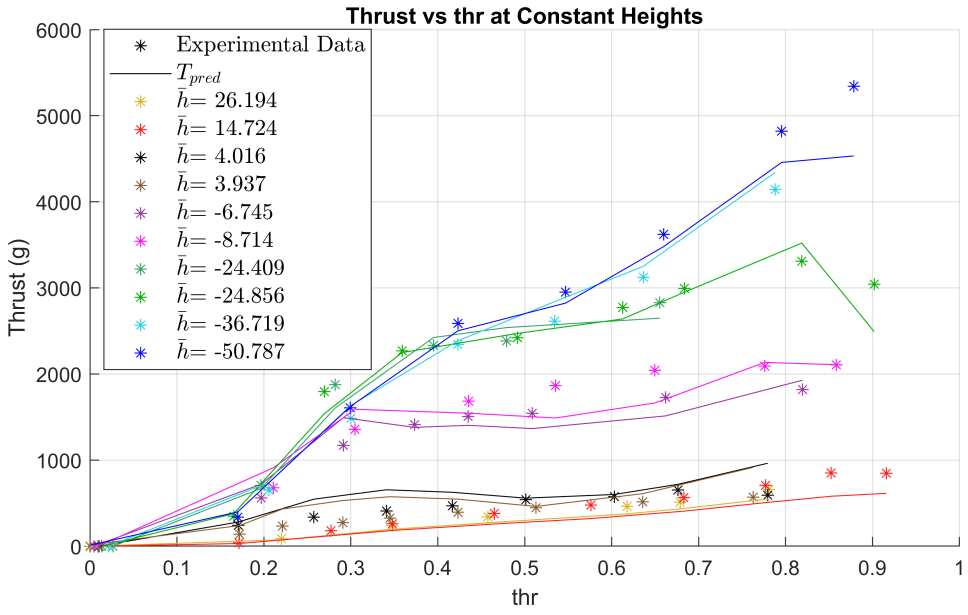

Figure 4.28: Experimental thrust values and predicted thrust values at constant heights

Figure 4.28 compares T_{pred} to experimental values of the rotor in transition at

constant heights. It can be seen that the formulation accurately predicts the thrust. Thrust during the transition has not been predicted without using CFD at anytime before, this is the first transition thrust prediction that can be preformed on an onboard microprocessor.

T_{pred} was also compared against experimental data in constant climb and descent speed transitions. Example results at a medium throttle setting going in and out of the water are shown in Figures 4.29 and 4.30 respectively.

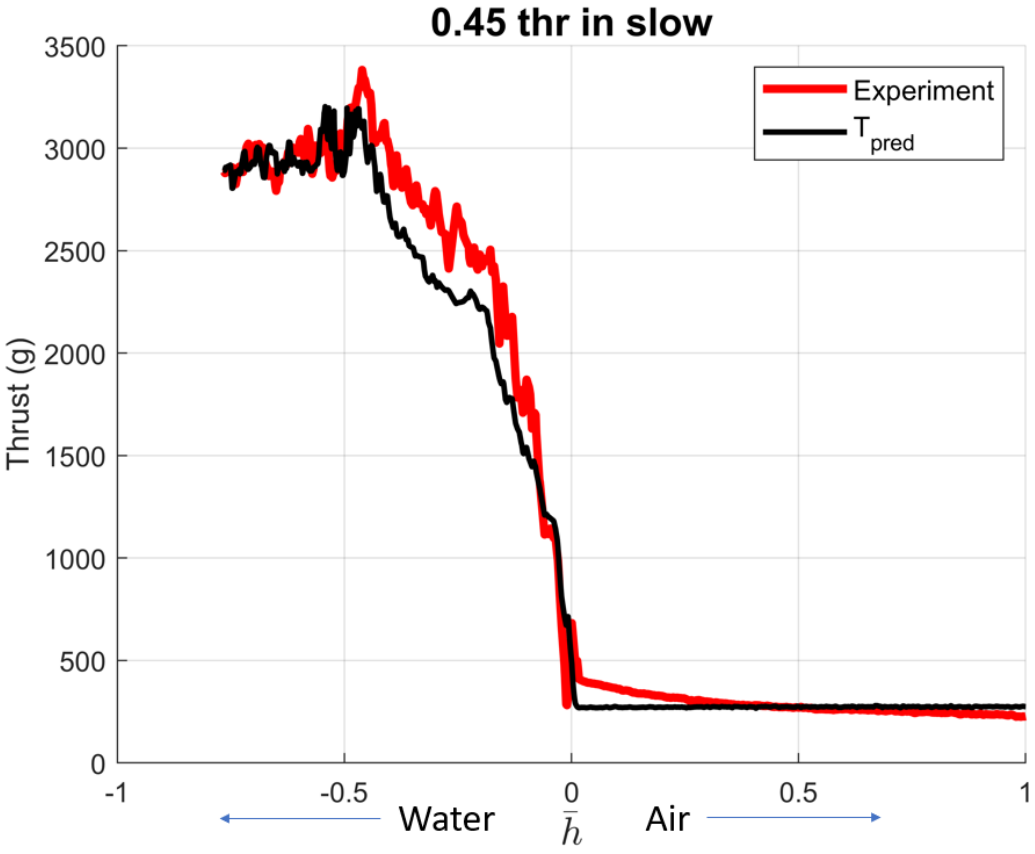

Figure 4.29: Comparison of predicted thrust to experiment at 45% throttle during slow entry into the water

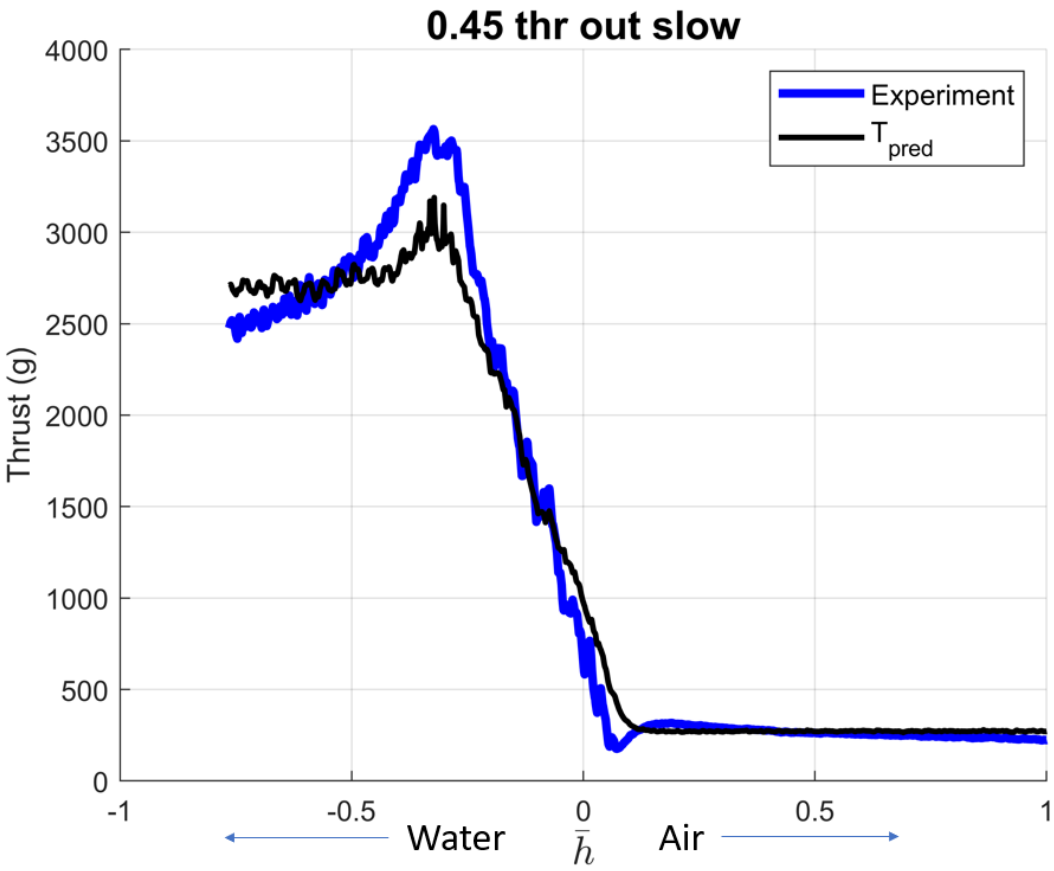

Figure 4.30: Comparison of predicted thrust to experiment at 45% throttle during slow exit out the water

These results show that the predicted thrust formulation shown as Equation 4.7 results in a good prediction of rotor thrust in transition states between air and water using only throttle input, motor RPM, and rotor non-dimensional properties as inputs. This strategy can be generalized easily to provide thrust predictions with any ESC, motor, rotor combination, as long as the rotor C_T and the RPM throttle response in air and water are known.

4.5 Controller Enabled Transitions

An application of the TI and T_{pred} formulations is in informing a controller on board a vehicle. The ability to predict thrust and transition state can be useful to precisely modulate the desired rotor thrust during a powered rotor water entry or exit without the need for specialized sensors or large computing capability. The only real-time information necessary for this prediction is the rotor RPM, which is within the set of standard sensor outputs required for multirotor flight, allowing this strategy to be easily generalized to many vehicles. One of the main reasons powered rotor transitions have not been widely attempted is the difficulty in predicting rotor performance, this restriction is now relieved.

As a proof of concept, a TI based feedback motor control loop is developed and tested on the test stand used for previous experiments. The goal of this controller is to maintain constant thrust through the transition. It should be noted that the setpoint can be variable based on vehicle bouyancy or desired transition characteristics in other applications. The design of the controller is diagrammed in Figure 4.31.

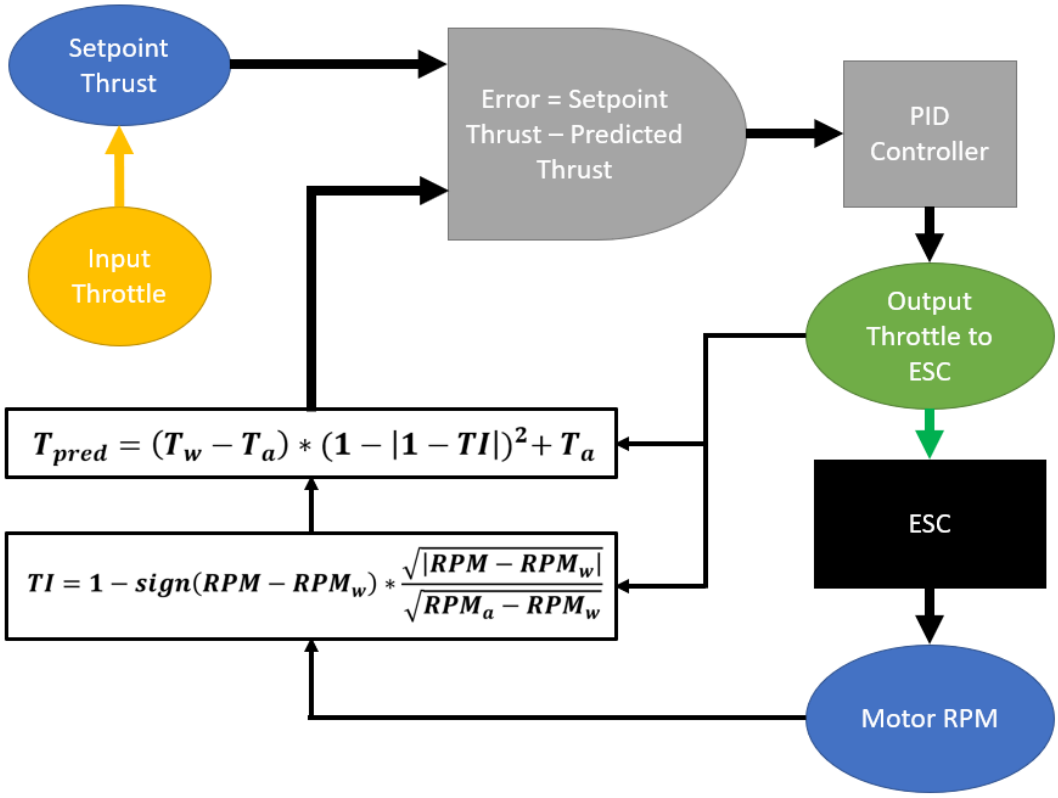

Figure 4.31: Diagram of the constant thrust TI feedback controller

This controller was tested with vehicle hardware, which includes 14 pole sensored 750KV motors and 1575 carbon fiber commercial propellers (pictured in Figure 4.32). As a result the ground effect characteristics are more prevalent in these tests than those shown prior. Because Equations 4.4 and 4.7 do not directly account for the underwater ceiling effect or ground effect, the impacts of these phenomenon on thrust persist.

Figure 4.32: 1575 carbon fiber propellers used on the AQWUA and during controller testing

Controller testing consists of data points taken without climb or descent velocity (labeled "stationary") as well as points taken during slow entrance into and exit out of the water. This allows the comparison of the final steady state thrust, as well as transition thrust in climb and descent.

Thrust and RPM as the rotor moves into the water with a constant input throttle are compared with TI controller disabled and enabled in Figures 4.33 and 4.34. In Figure 4.33 the peak thrust with the controller enabled during the transition is about half of the peak thrust without a controller, and the peak only occurs over a range of 5 cm ($\bar{h} = -.262$) below the water surface. The final thrust in the water is also much lower compared to the case without a controller. Additionally, it can be seen that the RPM decreases rapidly as the rotor hits the water in both controller enabled and disabled cases, however, at $\bar{h} = -.075$ the controller makes the RPM decrease further, wheras the baseline case RPM starts to stabilize. This RPM decrease mitigates the thrust peak and decreases the final thrust level.

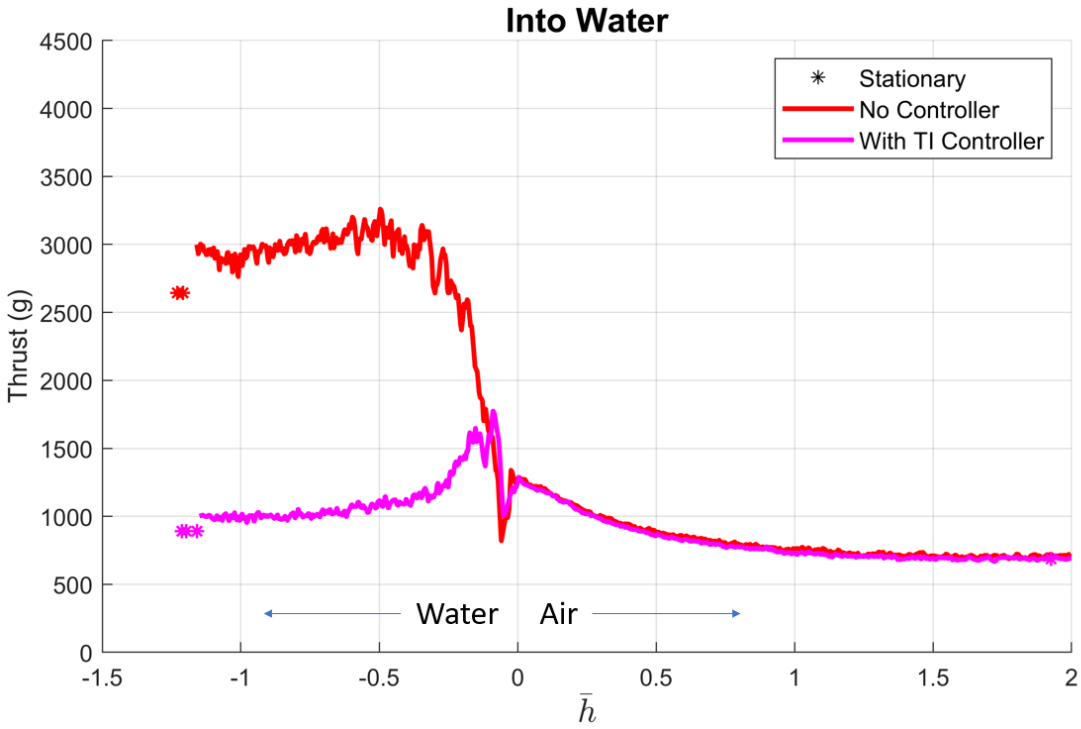

Figure 4.33: Comparison of thrust with no controller to controller modulated thrust during water entry

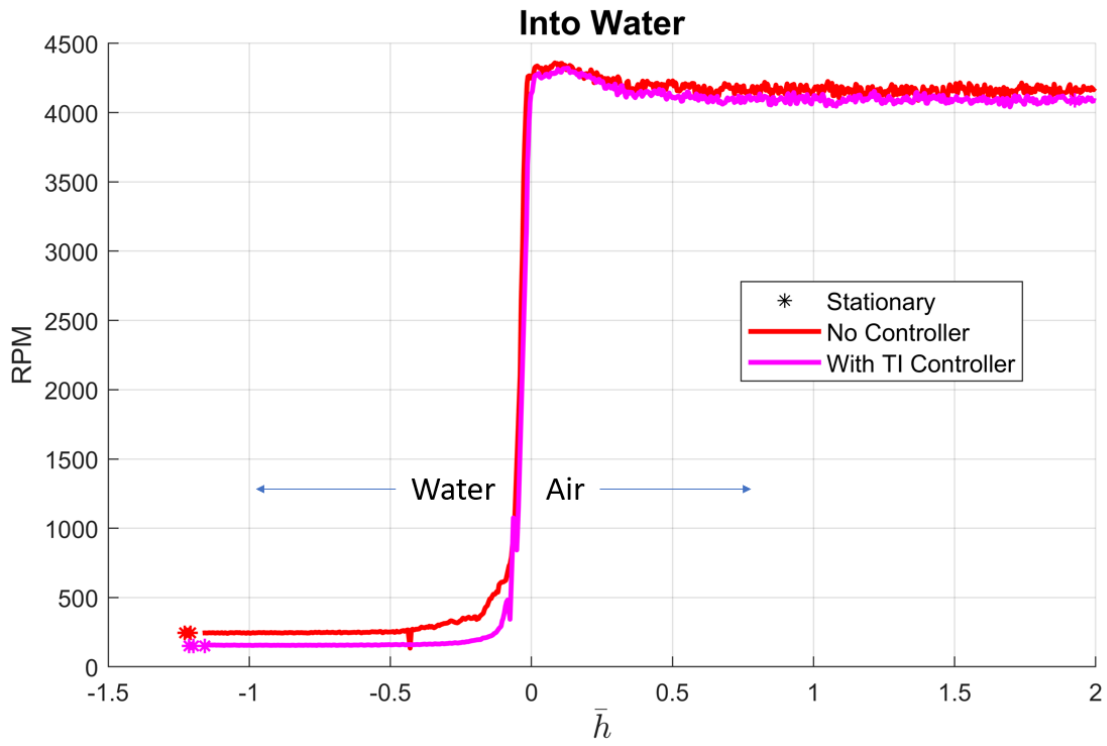

Figure 4.34: Comparison of RPM with no controller to controller modulated thrust during water entry

The controller was tested in a similar manner during exit out of the water. The thrust versus $\bar{h}$ plot reveals that the controller is able to increase the minimum thrust produced by the rotor from 16.7 g to 242 g. This effect is achieved by the controller increasing the RPM above the baseline case starting at $\bar{h} = -.16$, and adjusting the RPM in air to a higher point.

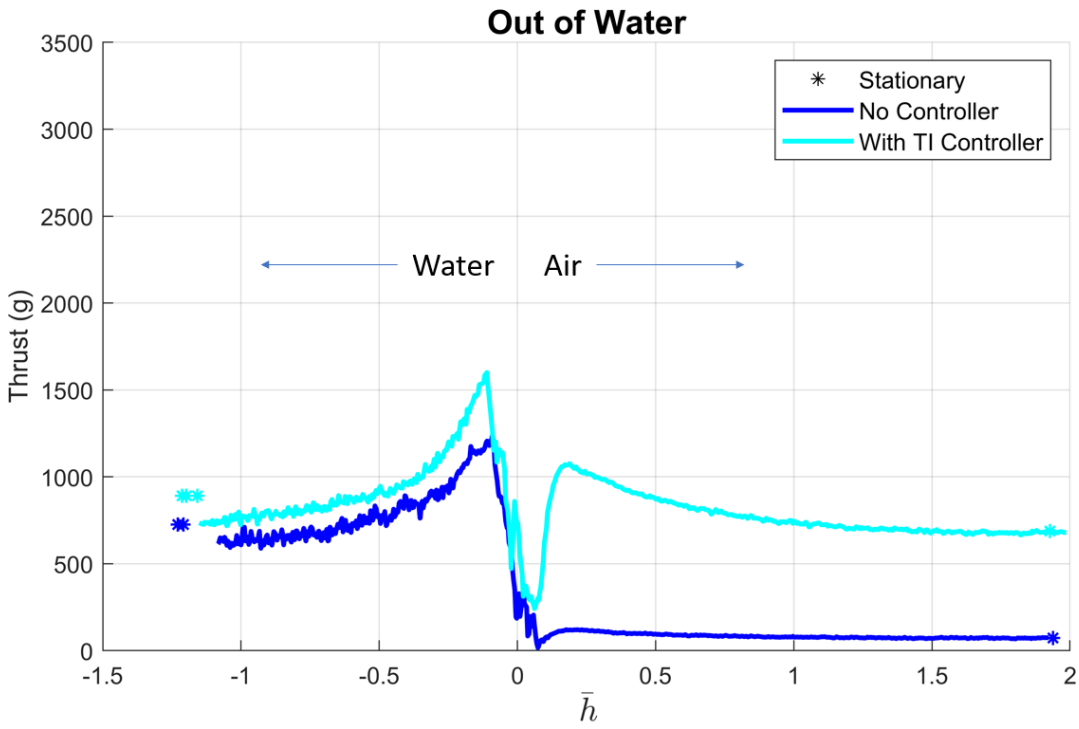

Figure 4.35: Comparison of thrust with no controller to controller modulated thrust during water exit

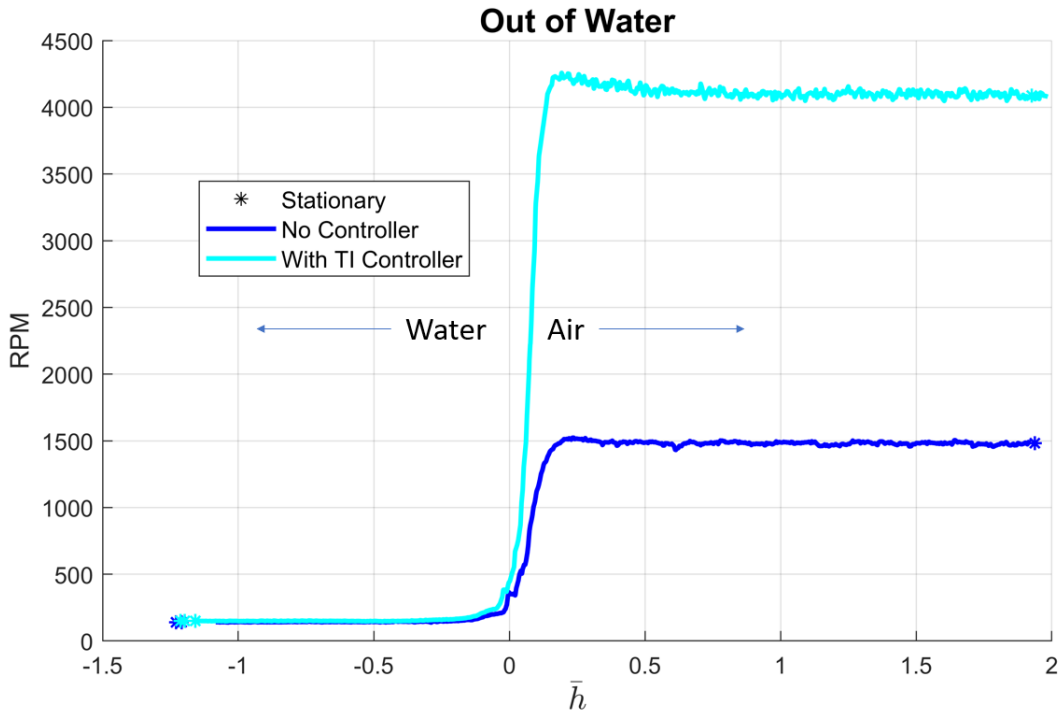

Figure 4.36: Comparison of RPM with no controller to controller modulated thrust during water exit

It is clear that the controller enabled transitions maintained a more consistent thrust. There is potential for the controller performance to be further improved with the addition of TI dependent gains and more optimal tuning.

4.6 Chapter Summary

The transition between air and water of a powered rotor has been characterized. It is shown that the state of the mixed air-water medium progresses gradually to a fully in air or fully in water state between $-0.33 < \bar{h} < 0.08$, and cannot be assumed to be a step change at $\bar{h} = 0$. Additionally, the overall density of this medium is sensitive the RPM of the rotor as well as $\bar{h}$.

Additional phenomenon of the rotor transition are found with regards to axial descent and climb through the air-water interface. It is shown that the transition at a constant throttle is relatively unaffected by vertical speeds between 2.4 cm/s and 7.3 cm/s.

Rotor performance at small positive heights above the water free surface is shown to be dependent on if the rotor is exiting or entering the water. At these heights during water entry, the rotor is operating in a fully in air state in ground effect. However during water exit the rotor operates in a mixed air water medium as the water is carried above the nominal free surface.

The maximum thrust during entry and exit transitions is found to occur during the exit at heights just below the water surface due to the underwater ceiling effect phenomenon.

The Transition Index TI is formulated to characterize the state of the rotor. It is found to appropriately predict the state of the mixed air-water medium the rotor operates in. The Transition Index also identifies the aeration of water during entry that does not occur during exit.

TI is used in a formulation to predict rotor thrust as well, and shown to have good agreement with experimental data for both stationary height tests as well as axial entry and exit tests. This thrust prediction is applied in a proof of concept controller to maintain constant thrust through the transition.

Chapter 5: Vehicle Description

5.1 AQWUA Overview

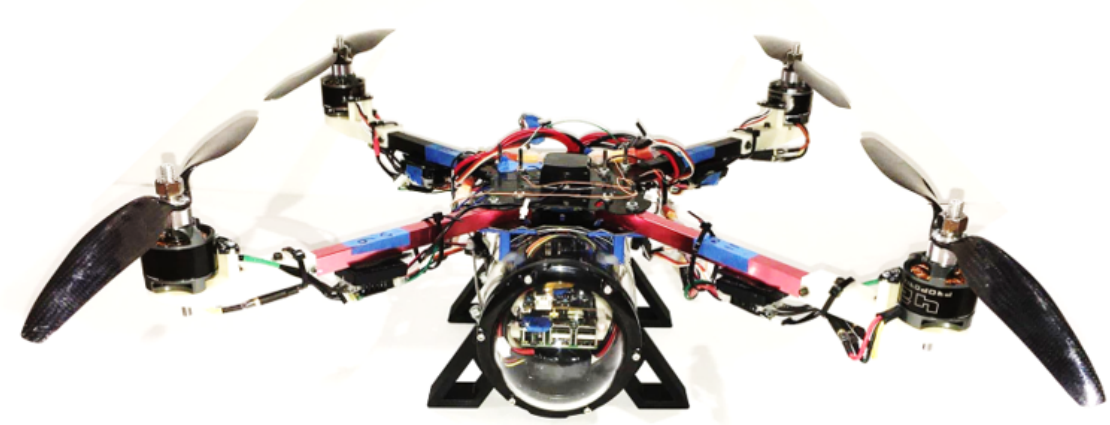

Figure 5.1: The AQWUA HAW vehicle

A prototype to demonstrate and test the implementation of the Transition Index control strategy was produced. A Quad With Underwater Ability (AQWUA) is a 3.5 kg quadrotor with a waterproof enclosure containing the main electronics and featuring waterproofed sensored motors and ESCs with 15 inch carbon fiber rotors.

The various features and components unique to this type of vehicle are described below.

5.2 Waterproofing

Any HAW vehicle must be capable of operating electronic components in the water, this necessitates a robust waterproofing strategy. AQWUA components inside the waterproof enclosure, shown in Figure 5.2, need no additional treatment. Components outside of it are treated individually.

5.2.1 Waterproof Enclosure

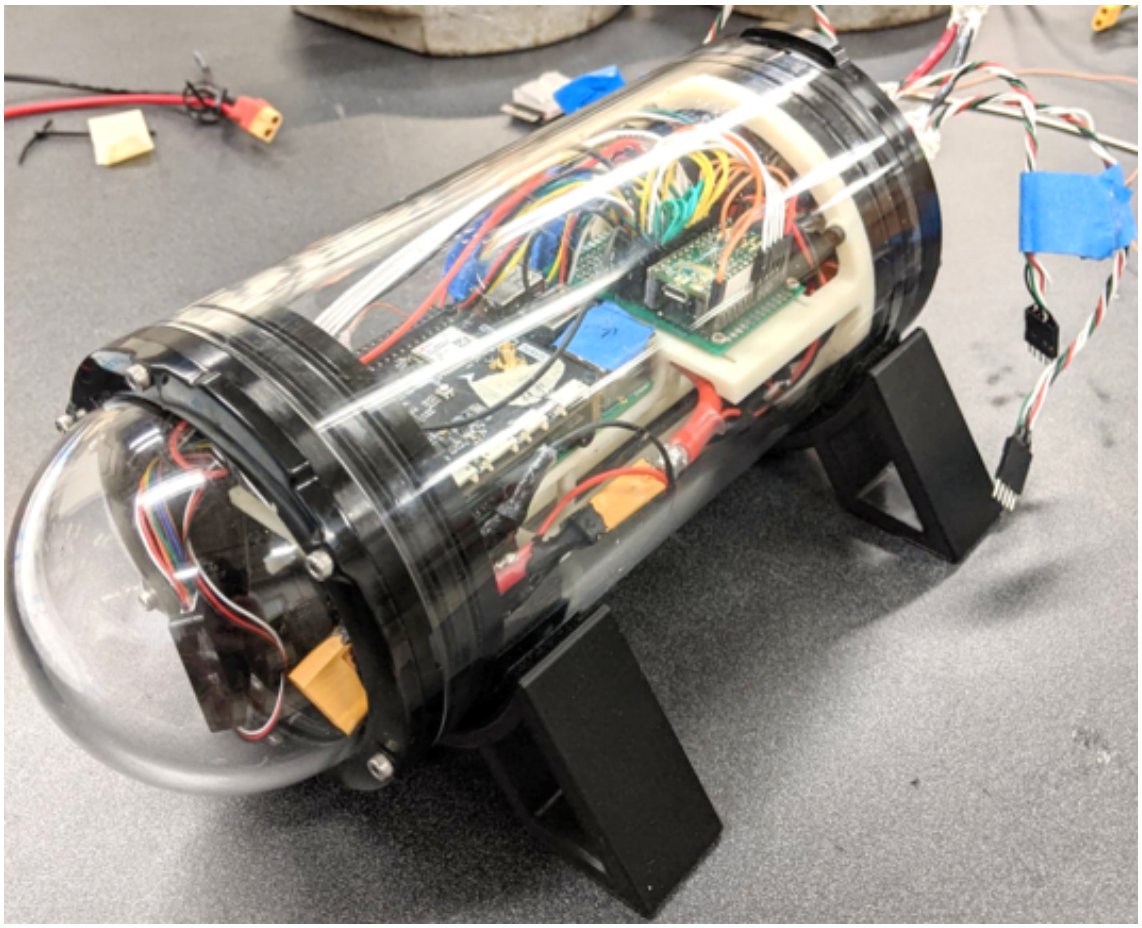

Figure 5.2: Photo of the waterproof enclosure

After multiple enclosure iterations the final design utilizes a Blue Robotics waterproof enclosure assembly. By using an enclosure designed for submersible ROVs, reliable performance is guaranteed. Lighter approaches were attempted, but exhibited repeated failure of waterproofing around the entrance and exit of cables.

The enclosure is centered around an acrylic tube with a 4 inch inner diameter. Two flanges with double 4 inch O-rings are inserted into each end. These flanges are bolted to an acrylic dome part in the front of the vehicle and an aluminum plate in the rear. There is an embedded O-ring between the flange and bolted part. These flanges are designed to be removed to allow access into the waterproof enclosure, whereas all other enclosure components are permanently bolted together.

All cables that carry signals and power out of the enclosure are attached to the alumnium end of the enclosure. These cables pass through cable penetrator components which can be seen in Figure 5.3. They pass the cable through a hollow part that bolts to the aluminum plate with an embedded O-ring. The cable is securely attached to the penetrator with marine epoxy, this forms a watertight seal around the cable and fixes it in place.

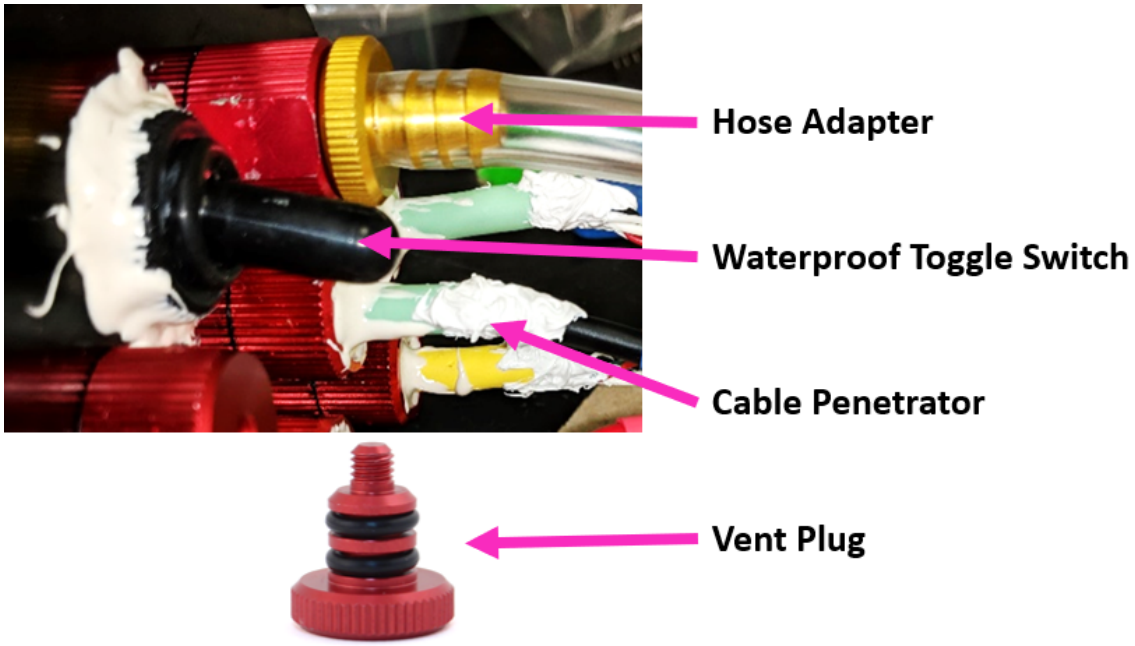

Figure 5.3: Photo of various components in aluminum endcap

One of the common locations of waterproofing failure is in the cable penetration locations. A robust implementation that has been designed and tested for submersible vehicles is critical.

The aluminum plate has two additional features that are not cable penetrators. First is a vent. This component is similar to a penetrator, except the inside is threaded and fits a vent plug that can be bolted in with two O-rings. The vent with a hose adapter and the vent plug can be seen in Figure 5.3. The vent is necessary for assembly and disassembly of the enclosure, the vent plug is absent during these steps to avoid pressure fluctuation in the enclosure that opposes the attachment or removal of an end cap. Additionally the vent allows the installation of a hose that leads to a pump via an adapter. The pump is used for waterproofing evaluation and troubleshooting.

The second is a waterproof toggle switch, this is a custom safety addition to the enclosure seen in Figure 5.3. A toggle switch with a waterproof rubber boot is bolted into the aluminum plate and permanently fixed with marine epoxy. The seamless rubber boot and epoxy form a watertight seal and allow the switch to be physically toggled. A switch allows for shutoff of the vehicle without requiring disassembly of the enclosure.

5.2.2 Enclosure performance

Measuring the water-tightness of the enclosure and identifying leak locations is done by utilizing the vent plug. The vent plug fits a hose adapter that connects a hose from a pump into the enclosure. The adapter with attached hose can be seen in Figure 5.3.

Performance is estimated by measuring the vacuum leak rate of the enclosure. An acceptable measure is a leak rate of less than 1.7 mbar per minute when the enclosure is evacuated to a pressure of 506 bar. This measure is ensures a negligible water leak rate.

It was found that a critical source of enclosure leakage occurs at the wire insulation. Despite a watertight seal at the cable penetrator, if a gap in the wire insulation exists, a leak may occur between the wire conductor and insulation. These types of gaps occur at connectors and were sealed with Loctite PL Marine Adhesive Sealant which is a flexible watertight compound that seals the leak and prevents wire damage.

To find leaks a soapy water method is used. The enclosure ends are mechanically clamped, and the enclosure is pressurized. Then water mixed with concentrated liquid dish soap is applied to various seams. Leaks will form an easily visible soap bubble as air escaping from the pressurized enclosure gets captured by the soap water film, an example of this can be seen in Figure 5.4.

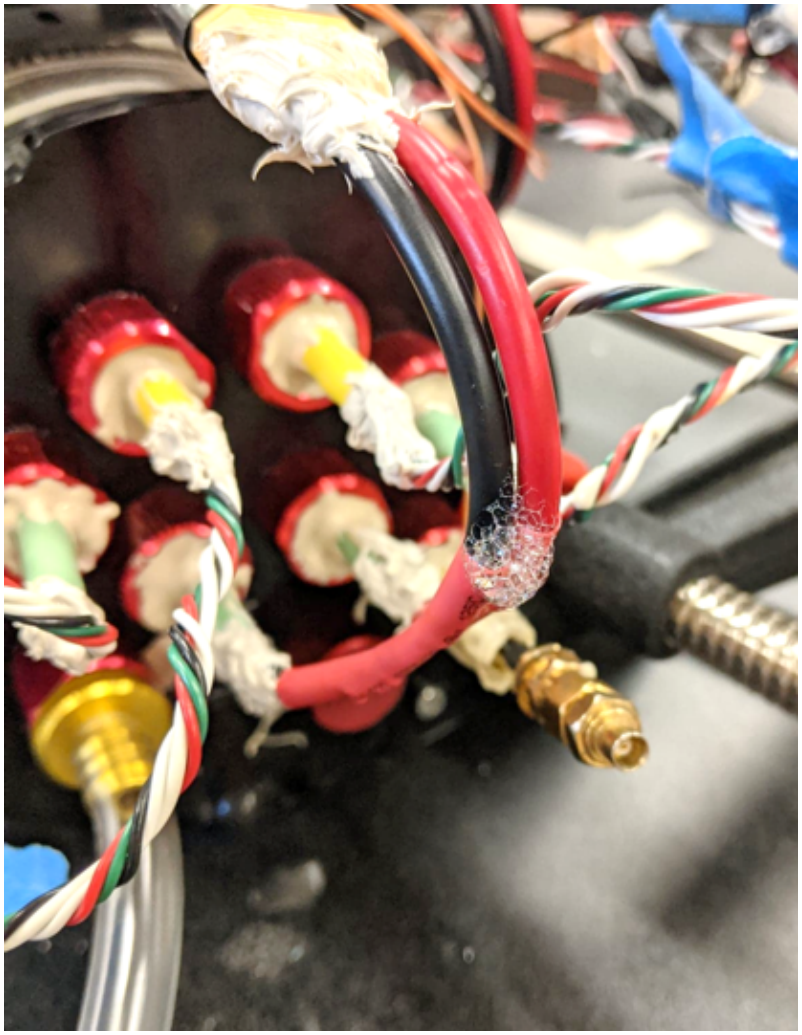

Figure 5.4: Photo of soapy water method revealing a leak at a wire splice

These methods allow for a reliable waterproof enclosure without requiring a water submersion, which risks damage to components. A submersion is only used

to verify the enclosure before a flight test.

5.2.3 Component Waterproofing

Three components outside of the enclosure require waterproofing: the ESCs, motors, and sensor boards. The waterproofing of these parts is done in the same manner as that described in Chapter 2.

The ESCs are dissasembled and the circuit board is coated with multiple layers of conformal coating, after reassembly all exposed wire areas near connections are treated with silicone. Due to the sensitivity of the sensor wire signal to interference from the water, the sensor wire connectors are treated with CorrosionX, a waterproofed ESC is shown in Figure 5.5. The motors are treated with CorrosionX HD in all exposed stator locations using a syringe.

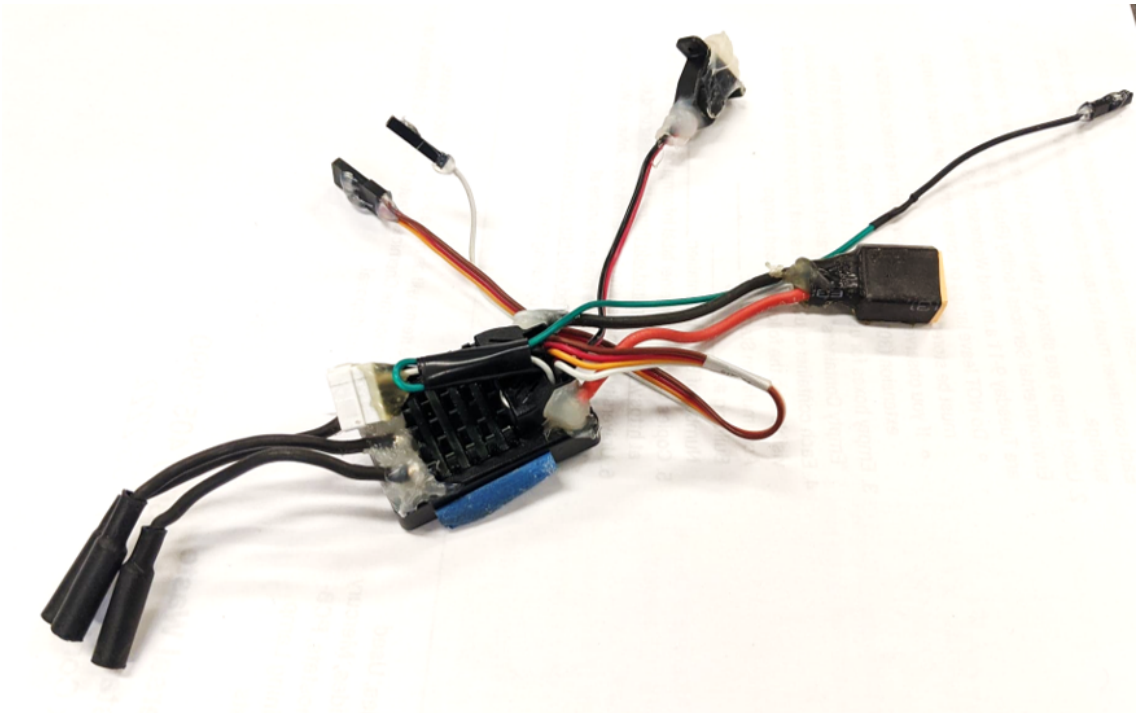

Figure 5.5: A waterproofed electronic speed controller (ESC)

Sensor boards are sensitive to interference and have multiple measures to prevent water damage. The boards are coated with multiple layers of conformal coating, then exposed solder pads and joints are additionally coated in silicone. Lastly, the entire board is treated with CorrosionX.

The various wires and connectors are treated with silicone and marine sealant to prevent interference of signals. Lastly it is critical that the conductor in the 72MHz whip antenna is insulated from the water. If contact were made the impedance of the antenna would change, and reciever function would be affected. This prompts a silicone seal at the end of the whip antenna, and thorough inspection of the insulation for breaks

5.3 Sensored Motors

A significant challenge of creating a single propulsion system HAW vehicle such as the AQWUA is the selection of BLDC motors capable of powering the rotors in both air and water conditions.

The design process featured a significant investigation into motor choice. Many motors were tested, including a 22 pole 320KV sensorless, and 14 pole 750KV sensorless, a 4 pole 1900KV sensored, and a 14 pole 750KV sensored motor.

It was found that sensorless motors were unable to achieve adequate performance in both air and water. BLDC motors without sensors rely on back-emf to estimate speed and position and have a reduced initial torque due to the heuristic motor start and slow speed commutation [25]. This is often a limiting factor for

motor operation in the water. For instance, the 14 pole sensorless 750KV motor showed good performance in the air, reaching top speeds of over 5000 RPM, but was unable to start rotation in the water. Conversely, the 22 pole 320KV motor has sufficient starting torque due to the high pole count, large coil size, and low KV rating. This allows acceptable performance in the water, delivering up to 0.93 Nm of torque. But, the low KV rating limits the maximum theoretical RPM on a 3S battery to 4032 RPM, and practically reaches top speeds of 3500 RPM. This low rotational speed provides insufficient thrust in the air for takeoff. Such a motor would only be acceptable for smaller vehicles.

Sensored motors use hall effect sensors to precisely measure the rotor position and allow smooth commutation through start and low speed regimes [26]. However, most commercially available sensored motors are 4 pole high KV BLDC mtoors designed for geared operation in surface vehicles. One such example is the 4 pole 1900KV motor investigated for the AQWUA. It showed good performance in the water with the ability to start and throttle, and achieved rotational speeds of over 4500 RPM. However, the 4-pole design is intended for low torque operation at high speed, and direct drive of a rotor at high speed in air resulted in a low efficiency causing excessive current draw and heat build up.

The 14-pole sensorless 750KV was then modified to feature a hall effect sensor board. This solution allows the motor to operate with smooth start and low speed throttling in the water, as well as achieve rotational speeds of 5000 RPM in the air. The motor efficiency in the air is decreased due to the inclusion of a sensored commutation adjusted for low speed timing, but the overall air and water performance

is increased to acceptable levels.

5.4 Avionics and Control

The AQWUA features an avionics suite that is centered around a standard quadrotor implementation, there are minimal additional hardware or sensor components. As seen in Figure 5.6, the design is based on a separate PJRC Teensy 4.0 control board between the autopilot and motors. Principally, this control board can be installed on any quadrotor vehicle that is waterproof and has a propulsion system with sufficient performance and RPM feedback. There are no limitations on configuration of sensor suite for this system to function (RPM feedback is considered a standard sensor). Additionally, the function of the control board and autopilot can be made to be one component if a custom autopilot is used.

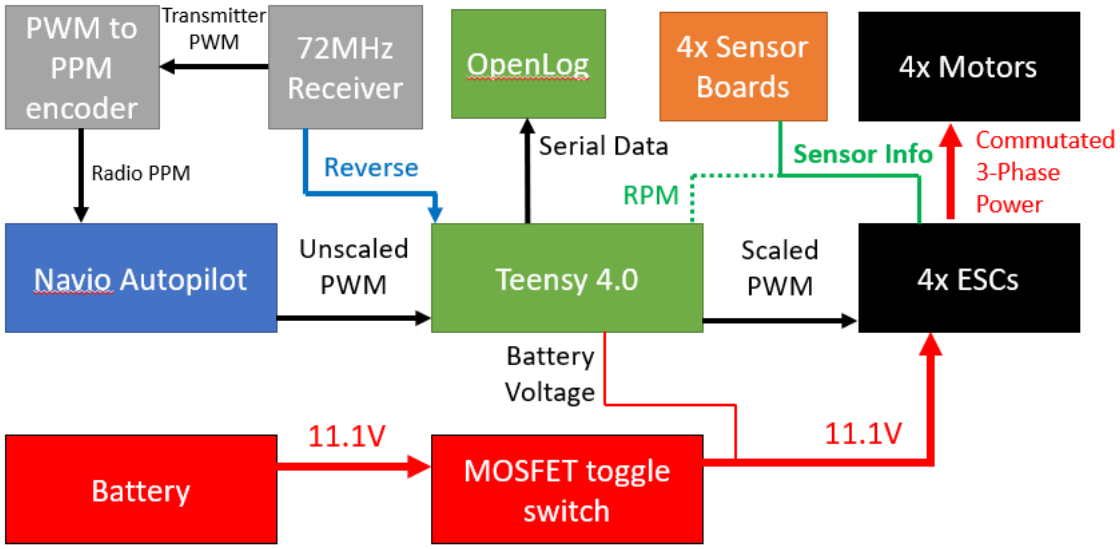

Figure 5.6: Schematic of AQWUA avionics

The Emlid Navio2 autopilot is a commercially available board that this vehicle

is built around, it is able to log flight data to internal memory. The Corona RP8D1 receiver and Pixhawk PPM encoder deliver pilot inputs to the autopilot. The battery powers the Castle Creations Micro Mamba X ESCs and PropDrive 42-38 motors, and a custom MOSFET battery shutoff switch allows the pilot to toggle the vehicle power from outside of the waterproof enclosure. The Equals Zero Designs motor sensor boards deliver position information to the ESCs to inform the commutation, and one of the hall effect sensor lines is also sent to the Teensy control board. The Teensy communicates with a Sparkfun OpenLog board over serial to log data to an SD card, and is installed on a custom breakout board designed to accept 5V signal.

It should be noted that the use of a 72 MHz radio system is a critical design feature. The modern 2.4 GHz radio systems more commonly used in aerial vehicles have poor penetration of water due to the short wavelength [27]. It is for this reason that the lowest frequency radio system commercially available is used for the AQWUA.

The Teensy control board is able to operate in a controller off mode, where the throttle from the autopilot is proportionally scaled to the accepted input range of the ESC, as well as a controller on mode. With the controller on, the Teensy enables the feedback controller described in Chapter 4 on the motor throttles with the input throttle set by the autopilot output. Additionally, this mode enables reverse thrust operation.

5.5 Flight Testing

The vehicle was flight tested with and without the controller enabled with partial success. Unfortunately, malfunctioning wire connections caused inaccurate RPM readings in the water, which misinformed the TI calculations and TI controller. However, despite the malfunction, partial function of the controller still resulted in improved performance and allowed air-water transitions. No leaks in the waterproofing were found, and radio connection was maintained at all times.

With the controller disabled, the AQWUA was unable to perform the transition into the water with powered rotors. Even at minimal thrust upon approaching the water, when the rotors hit the water, the large thrust forced an immediate exit. This resulted in the vehicle floating on the water surface, and whenever a rotor struck the surface it caused a pitch or roll such that the rotor lifts out of the water. The opposite rotor would then strike the water and the same process would occur. An instance of this is pictured in Figure 5.7 with the right most rotors striking the water and the left most rotors having just exited.

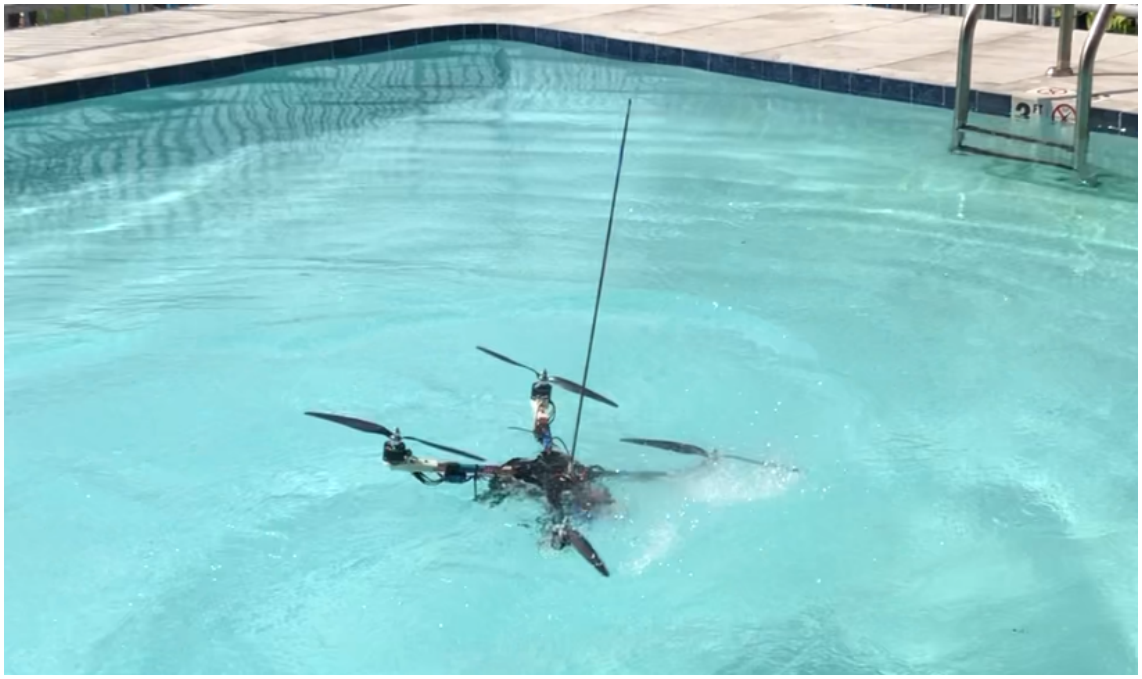

Figure 5.7: Photo of AQWUA unable to perform transition with controller disabled

The controller used faulty RPM data during the flight, with very large scatter obscuring accurate readings. Despite this, the occasional accurate reading would prompt a decrease in throttle, which allowed for a successful transition. The transition was furthered by reversing thrust to increase the depth. An image of this is shown in Figure 5.8.

Figure 5.8: Photo of AQWUA performing transition with controller enabled

It should be noted that although attempted, water-air transition were not possible due to an unbalanced center of buoyancy. The center of mass and center of thrust are aligned vertically, however the center of buoyancy is forward from the center of mass. This caused a pitch up moment underwater that could not be corrected.

5.6 Chapter Summary

The AQWUA HAW vehicle and design is described. The waterproof enclosure design, and procedures for testing and waterpoofing external components are detailed. Avionics implemented for flight with and without the TI controller enabled are also detailed, with consideration to unique aspects.

Flight testing with attempted transitions into the water was performed with partial success due to equipment malfunction. This demonstration platform proved promising, although more time is required to fully realize its potential.

Chapter 7: Conclusions

7.1 Summary of Research

This thesis focuses on the development of an understanding of rotor performance in the air-water transition.

This understanding is built with an experimental setup that can move a powered rotor through an air-water transition and record RPM, thrust, and torque data. First, an understanding of rotor performance differences between fully in air and fully in water environments is achieved by testing manufactured rotors with known parameters, and comparing their performance to results modeled with BEMT using airfoil tables generated by TURNS2D.

Transition performance of the rotor is characterized by performing tests at various throttles and stationary heights, as well as constant throttles and fixed speeds into and out of the water.

Finally, a vehicle built to demonstrate the application of the insights gained in testing is described, and its performance is discussed.

7.2 Conclusions

1. Multirotor HAW vehicles have configuration, transition characteristic, and weight constraints imposed by the strategy implemented to avoid a powered rotor in transition. These can be relaxed or removed by leveraging an understanding of a powered rotor in transition.

2. Cambered plate airfoils show high sensitivity to Reynolds number effect, with higher Reynolds numbers resulting in higher lift to drag ratio at low angles, and earlier onset of stall.

3. Structural properties of an aerial rotor in water are important in avoiding instability.

4. Aerial rotor performance is modified in the water due to elastic deformations, resulting in different C_T and C_P in the two mediums.

5. The transition between air and water of a powered rotor occurs gradually between $\bar{h} = -1/3$ and the water surface.

6. The mixed air-water medium that the rotor operates in during the transition is a function of rotor height relative tot he water surface as well as the RPM of the rotor.

7. Rotor performance in the transition during water entry and exit is not sensitive to the speed of the transition between 2.4 cm/s and 7.3 cm/s.

8. Maximum thrust occurs during water exit at a height just below the water free surface due to the underwater ceiling effect

9. The rotor introduces water to heights just above the free surface on exit that is not present during water entry, modifying the characteristics of transition at that height.

10. The Transition Index TI is a valuable metric that informs on the state of the medium the rotor operates in

11. Aeration of water during entrance modifies the medium the rotor operates in past the 1.3 rotor radius depth

12. TI can be used to accurately predict thrust through the rotor transition

13. Thrust prediction can be implemented in a feedback controller to achieve target thrust through the transition.

14. HAW vehicle challenges in construction include waterproofing and propulsion system design

15. A HAW vehicle in a standard quadrotor configuration can perform transitions into the water when equipped with a TI based controller.

7.3 Future Work

Due to the young state of the multirotor HAW field, and the novel nature of the powered rotor in transition research, the potential for future work is large. Some

areas in which future work will be productive are described below.

1. **Scalability**: This work focused on a rotors with a diameter of up to 15 inches. The transition performance of rotors at smaller and larger scales should be compared to these results. The ability of TI to generalize to larger scale variations should be confirmed.

2. **Angled Transitions**: Transitions performed for this thesis used a rotor oriented such that the tip path plane was parrallel with the water surface. Such transitions are the most common in multirotor HAW vehicles, but a potential improvements of powered rotors through the transition include the ability to make angled transitions. Data on the performance of a powered rotor in a transition that asymmetrically affects the rotor should be collected and analyzed.

3. **Controller Improvements**: The TI enabled controller used the maintenance of a constant thrust through the transition and implemented on the AQWUA is a demonstration level application of TI. Additional work to increase performance, intelligently manipulate the setpoint, and better account for ground and ceiling effects can greatly improve on the results shown in this thesis. Additionally, modification to the vehicle attitude controller should be made to better interface with the TI controller and improve vehicle performance in the water.

4. **Physics Based Modeling**: The TI and thrust prediction are useful practical formulations for flight controllers. However, estimating performance based on

rotor geometry only is a powerful tool for designing optimized rotors and simulating transitions. Such estimation has been performed with CFD, but no analytical formulation exists. This would serve as a powerful tool for design and evaluation.

Bibliography

[1] J. Gordon. Leishman. *Blade Element Analysis*, page 115–169. 2008.

[2] Offshore wind farm inspection. *Balmore Aerial Media*, Nov 2019. `https://balmoreuav.co.uk/offshore-wind-farm-inspection/`.

[3] Doug Thaler. Drone inspection for bridges – a technology for transformation? *Infrastructure Preservation Corporation*, Dec 2017. `https://www.infrastructurepc.com/drone-inspection-for-bridges/`.

[4] Mariano Castillo. U.s. successfully launches drone from submerged submarine. *CNN*, Dec 2013. `https://www.cnn.com/2013/12/06/us/submarine-drone-launch/index.html`.

[5] Adam Haydock. Cave divers trapped for 69 hours. *Dive Magazine*, 2018. `http://divemagazine.co.uk/skills/8284-cave-divers`.

[6] Yu Herng Tan, Rob Siddall, and Mirko Kovac. Efficient aerial–aquatic locomotion with a single propulsion system. *IEEE Robotics and Automation Letters*, 2(3):1304–1311, 2017.

[7] Alexis Lussier Desbiens, Morgan T Pope, David L Christensen, Elliot W Hawkes, and Mark R Cutkosky. Design principles for efficient, repeated jumpgliding. *Bioinspiration & Biomimetics*, 9(2):025009, 2014.

[8] Marco M Maia, Parth Soni, and Francisco J Diez. Demonstration of an aerial and submersible vehicle capable of flight and underwater navigation with seamless air-water transition. *arXiv preprint arXiv:1507.01932*, 2015.

[9] Marco M Maia, Diego A Mercado, and F Javier Diez. Design and implementation of multirotor aerial-underwater vehicles with experimental results. In *2017 IEEE/RSJ International Conference on Intelligent Robots and Systems (IROS)*, pages 961–966. IEEE, 2017.

[10] Alexandre C Horn, Pedro M Pinheiro, Cesar B Silva, Armando Alves Neto, and Paulo LJ Drews-Jr. A study on configuration of propellers for multirotor-like hybrid aerial-aquatic vehicles. In *2019 19th International Conference on Advanced Robotics (ICAR)*, pages 173–178. IEEE, 2019.

[11] Hamzeh Alzu'bi, Iyad Mansour, and Osamah Rawashdeh. Loon copter: Implementation of a hybrid unmanned aquatic–aerial quadcopter with active buoyancy control. *Journal of field Robotics*, 35(5):764–778, 2018.

[12] Keith Henderson. Planetsolar passes halfway point. *Maritime Propulsion*, May 2011. `http://articles.maritimepropulsion.com/article/PlanetSolar-passes-halfway-point-1445.aspx`.

[13] B Yim. An application of linearized theory to water entry and water exit problems. part i (with gravity effect). Technical report, Naval Ship Research and Development Center Washington D.C., 1969.

[14] Okitsugu Furuya. A performance-prediction theory for partially submerged ventilated propellers. *Journal of Fluid Mechanics*, 151:311–335, 1985.

[15] DP Wang et al. Water entry and exit of a fully ventilated foil. *Journal of Ship Research*, 21(01):44–68, 1977.

[16] YL Young and SA Kinnas. Analysis of supercavitating and surface-piercing propeller flows via bem. *Computational Mechanics*, 32(4-6):269–280, 2003.

[17] Ashish Karn, Siyao Shao, Roger EA Arndt, and Jiarong Hong. Bubble coalescence and breakup in turbulent bubbly wake of a ventilated hydrofoil. *Experimental Thermal and Fluid Science*, 70:397–407, 2016.

[18] Bimlesh Kumar. Energy dissipation and shear rate with geometry of baffled surface aerator. *Chemical Engineering Research Bulletin*, 14(2):92–96, 2010.

[19] Radim Petříček, Tomáš Moucha, František Jonáš Rejl, Lukáš Valenz, Jan Haidl, and Tereza Čmelíková. Volumetric mass transfer coefficient, power input and gas hold-up in viscous liquid in mechanically agitated fermenters. measurements and scale-up. *International Journal of Heat and Mass Transfer*, 124:1117–1135, 2018.

[20] J. Gordon. Leishman. *Blade Element Analysis*, page 115–169. Cambridge University Press, 2008.

[21] Justin Michael Winslow. *Understanding of Low Reybolds Number Aerodynamics and Design of Micro Rotary-Wing Air Vehicles*. M.S. thesis, University of Maryland, 2016.

[22] Masato Okamoto, Kunio Yasuda, and Akira Azuma. Aerodynamic characteristics of the wings and body of a dragonfly. *Journal of experimental biology*, 199(2):281–294, 1996.

[23] Jason Crane and Imraan Faruque. Testing and characterization of hybrid unmanned aerial/underwater vehicle at the air-water interface. In *American Helicopter Society International Annual Forum and Technology Display Annual forum proceedings*, pages 2986–2993. AHS, 2017.

[24] Yi Hsuan Hsiao and Pakpong Chirarattananon. Ceiling effects for hybrid aerial–surface locomotion of small rotorcraft. *IEEE/ASME Transactions on Mechatronics*, 24(5):2316–2327, 2019.

[25] Satoshi Ogasawara and Hirofumi Akagi. An approach to position sensorless drive for brushless dc motors. *IEEE Transactions on Industry Applications*, 27(5):928–933, 1991.

[26] Alexander Rowe, Gourab Sen Gupta, and Serge Demidenko. Instrumentation and control of a high power bldc motor for small vehicle applications. In *2012 IEEE International Instrumentation and Measurement Technology Conference Proceedings*, pages 559–564. IEEE, 2012.

[27] Umair Mujtaba Qureshi, Faisal Karim Shaikh, Zuneera Aziz, Syed M Zafi S Shah, Adil A Sheikh, Emad Felemban, and Saad Bin Qaisar. Rf path and absorption loss estimation for underwater wireless sensor networks in different water environments. *Sensors*, 16(6):890, 2016.